

# UC Irvine

## UC Irvine Electronic Theses and Dissertations

### Title

The Very Near Field of High-Speed Jets from Simple and Complex Nozzles

### Permalink

<https://escholarship.org/uc/item/7dt9v614>

### Author

Adam, Andres

### Publication Date

2022

### Copyright Information

This work is made available under the terms of a Creative Commons Attribution License, available at <https://creativecommons.org/licenses/by/4.0/>

Peer reviewed|Thesis/dissertation

UNIVERSITY OF CALIFORNIA,  
IRVINE

The Very Near Field of High-Speed Jets from Simple and Complex Nozzles

DISSERTATION

submitted in partial satisfaction of the requirements  
for the degree of

DOCTOR OF PHILOSOPHY

in Mechanical and Aerospace Engineering

by

Andres Manuel Adam Alberdi

Dissertation Committee:  
Professor Dimitri Papamoschou, Chair  
Professor Feng Liu  
Professor Haithem Taha

2022



# TABLE OF CONTENTS

	Page
<b>LIST OF FIGURES</b>	<b>v</b>
<b>LIST OF TABLES</b>	<b>x</b>
<b>NOMENCLATURE</b>	<b>xi</b>
<b>ACKNOWLEDGMENTS</b>	<b>xiii</b>
<b>VITA</b>	<b>xiv</b>
<b>ABSTRACT OF THE DISSERTATION</b>	<b>xv</b>
<b>1 Introduction</b>	<b>1</b>
1.1 Motivation . . . . .	1
1.2 Research Objectives . . . . .	3
1.3 Thesis Overview . . . . .	4
<b>2 Literature Review</b>	<b>5</b>
2.1 Sources of Jet Noise . . . . .	5
2.2 Turbulent Mixing Noise . . . . .	7
2.3 Physics of Multi-Stream Jets . . . . .	11
2.4 Modeling of Jet Noise . . . . .	13
2.4.1 Acoustic Analogies . . . . .	13
2.4.2 Surface-based models . . . . .	15
2.4.3 Present model . . . . .	16
<b>3 Study of a Single-Stream Jet</b>	<b>21</b>
3.1 Jet Flow . . . . .	21
3.1.1 Jet Parameters . . . . .	21
3.1.2 Numerical Methods . . . . .	22
3.1.3 Simulation Parameters . . . . .	23
3.2 Scales in LES Flow Field . . . . .	24
3.2.1 Space-Time Correlations . . . . .	24
3.2.2 Convective Velocity . . . . .	26
3.2.3 Fixed-Frame Length Scales . . . . .	26
3.2.4 Moving-Frame Length Scales . . . . .	27

3.2.5	Azimuthal Scale . . . . .	28
3.3	Overview of the Flow Field . . . . .	28
3.3.1	Mean Velocity . . . . .	28
3.3.2	Reynolds Stress . . . . .	30
3.3.3	Convective Velocity . . . . .	31
3.3.4	Instantaneous Vorticity . . . . .	36
3.4	Longitudinal Correlations . . . . .	38
3.4.1	Two-Dimensional Correlations . . . . .	38
3.4.2	Fixed-Frame Length Scales . . . . .	40
3.4.3	Moving-Frame Length Scales . . . . .	45
3.5	Azimuthal Correlations . . . . .	47
3.5.1	Modal Components . . . . .	47
3.5.2	Cross-Sectional Correlations . . . . .	49
3.5.3	Azimuthal Scales . . . . .	49
3.6	Modeling Based on the Time-Averaged Flow . . . . .	52
3.6.1	RANS-Based Statistics . . . . .	53
3.6.2	Radiator Surface . . . . .	55
3.6.3	Convective Velocity . . . . .	56
3.6.4	Length Scales . . . . .	58
3.6.5	Azimuthal Scale . . . . .	59
3.7	Summary . . . . .	59
<b>4</b>	<b>Study of Three-Stream Jets</b>	<b>63</b>
4.1	Jet Flows . . . . .	63
4.1.1	Jet Parameters . . . . .	64
4.1.2	Computational Details . . . . .	67
4.2	Mean Flow Fields . . . . .	69
4.2.1	Mean axial velocity . . . . .	69
4.2.2	Reynolds stress . . . . .	72
4.3	Outer surface of peak stress . . . . .	73
4.3.1	Comparisons of LES and RANS results . . . . .	77
4.4	Radiator surface . . . . .	81
4.4.1	Distribution of Convective Velocity . . . . .	81
4.4.2	Approximation Based on the Mean Flow . . . . .	85
4.4.3	Flow Features Near the Jet Edge . . . . .	88
4.5	Longitudinal Correlations . . . . .	99
4.5.1	2D Space-Time Correlations . . . . .	99
4.5.2	Longitudinal Length Scales . . . . .	101
4.6	Azimuthal Correlations . . . . .	110
4.6.1	Azimuthal Scales . . . . .	110
4.6.2	Modeling Based on RANS Flow Field . . . . .	111
4.7	Summary . . . . .	115

<b>5</b>	<b>Elements of a Linear Surface-Based Model</b>	<b>118</b>
5.1	Theoretical Framework . . . . .	120
5.1.1	Axial shape . . . . .	121
5.1.2	Modeling from RANS . . . . .	122
5.2	Methodology . . . . .	124
5.2.1	BEM input . . . . .	124
5.2.2	Model calibration . . . . .	125
5.3	Model Results . . . . .	127
5.3.1	Effects of Length Scales . . . . .	127
5.3.2	Effects of Frequency and Length Coefficients . . . . .	130
<b>6</b>	<b>Conclusions</b>	<b>135</b>
6.1	Summary of Work Completed . . . . .	135
6.2	Recommendations for Future Work . . . . .	139
	<b>Bibliography</b>	<b>141</b>
	<b>A Noise Propagation through the Boundary Element Method</b>	<b>151</b>
	<b>B Flow Features Near the Edge of the Single-Stream Jet</b>	<b>161</b>

# LIST OF FIGURES

	Page
2.1 Far field noise spectrum of an overexpanded jet at a Mach number of 1.5. The microphone is at $150^\circ$ to the downstream jet axis. Data from Seiner [97]. . . . .	6
2.2 Diagram showing the turbulent mixing noise generation mechanisms in a single-stream jet. . . . .	7
2.3 Mach wave emission in the case of a wavy wall moving with velocity $U_c$ supersonic with respect to the ambient speed of sound. . . . .	8
2.4 Wavepacket shape moving at $U_c$ with envelope defined by $\mathcal{A}(x)$ . . . . .	10
2.5 Basic elements of a two-stream jet, from Papamoschou [72]. . . . .	12
2.6 Basic elements of surface-based modeling of the jet noise source. . . . .	17
2.7 Representation of the wavepacket model for a multi-stream jet. . . . .	20
3.1 Visualization of the single-stream jet over the numerical grid, with its boundary conditions. The jet contour plots instantaneous axial velocity from 0 (white) to $U_j$ (red). . . . .	23
3.2 Examples of stencils used in the determination of length scales. Reference points are located (A) between centerline and lipline, (B) between lipline and $9^\circ$ edge, and (C) outside $9^\circ$ edge. . . . .	25
3.3 Space-time correlation $R_{pp}$ in the vortical field at $x/D_j = 2.5$ and $r/D_j = 0.5$ . Dotted lines: fits by seventh-order polynomials. Dashed lines: envelope and ordinate relevant to the calculation of $\widehat{L}_p$ . . . . .	26
3.4 Distribution of normalized mean axial velocity. (a) Isocontours on a symmetry plane; (b) axial distribution on jet centerline compared to experiments by Lau <i>et al.</i> [56]. . . . .	29
3.5 Axial distributions of momentum thickness $\delta_\theta/D_j$ (solid black line) and inner edge of shear layer $r_i/D_j$ (dashed blue line). Dotted line indicates linear fit. . . . .	30
3.6 Isocontours of normalized Reynolds stress magnitude $g/U_j^2$ . Black line: SPS. . . . .	31
3.7 Isocontours of normalized convective velocity $U_{c_p}/U_j$ on a meridional plane. Red line: SPS. White line: radiator surface. . . . .	32
3.8 Isocontours of normalized convective velocity $U_{c_u}/U_j$ on a meridional plane. Red line: SPS. White line: radiator surface. . . . .	32
3.9 Representation of wavepacket model for the single-stream jet. . . . .	34
3.10 Radial distributions of $\bar{u}$ , $U_{c_u}$ , and $U_{c_p}$ at (a) $x/D_j=3$ , (b) $x/D_j=5$ , and (c) $x/D_j=8$ . Legend is the same for all plots. . . . .	35
3.11 Axial distributions of $U_{c_p}$ , $U_{c_u}$ , and $\bar{u}$ on the SPS. . . . .	36

3.12	Contour of instantaneous vorticity norm along a longitudinal plane. Black double line: radiator surface. White line: SPS. . . . .	37
3.13	Representation of swirling strength at the value $\lambda_{ci} = U_j/D_j$ . White double line: radiator surface. Red line: SPS. . . . .	37
3.14	Contours of $R_{uu}$ (left column) and $R_{pp}$ (right column) with reference point on SPS at $(x, r) = (3, 0.5)D_j$ for three time separations. . . . .	39
3.15	Contours of $R_{uu}$ (left column) and $R_{pp}$ (right column) with reference point on SPS at $(x, r) = (7.5, 0.5)D_j$ for three time separations. Legend is the same as for Fig. 3.14. . . . .	41
3.16	Isocontours of normalized length scales (a) $L_u/D_j$ and (b) $L_p/D_j$ . Red line: SPS. White line: radiator surface. . . . .	42
3.17	Simplified sketch of an eddy representation through velocity and pressure fluctuations. . . . .	43
3.18	Axial distribution of the correlation scales $L$ on the relevant surfaces. Orange solid line: $L_u$ on SPS. Blue dashed line: $L_u$ on the radiator surface. Green dotted line: $L_p$ on SPS. Black line dash-dot: $L_p$ on the radiator surface. . . . .	44
3.19	Plots of normalized length scales $L/\delta_\theta$ versus normalized radius $(r - r_i)/\delta_\theta$ , (a) based on axial velocity, (b) based on pressure. Legend applies to both subfigures. . . . .	45
3.20	Isocontours of normalized length scales (a) $\hat{L}_u/D_j$ and (b) $\hat{L}_p/D_j$ . Red line: SPS. White line: radiator surface. . . . .	46
3.21	Axial distribution of length scales $\hat{L}$ on the relevant surfaces. Orange solid line: $\hat{L}_u$ on SPS. Blue dashed line: $L_u$ on the radiator surface. Green dotted line: $\hat{L}_p$ on the SPS. Black line dash-dot: $\hat{L}_p$ on the radiator surface. . . . .	47
3.22	Plots of normalized moving-frame length scales $\hat{L}/\delta_\theta$ versus similarity coordinate $(r - r_i)/\delta_\theta$ , (a) based on axial velocity; (b) based on pressure. Legend applies to both subfigures. . . . .	48
3.23	Radial distribution of modal powers on $x = 7.5D_j$ for the first five modes; (a) based on axial velocity, (b) based on pressure. The vertical lines mark the locations of the SPS (red) and the radiator surface (blue). . . . .	49
3.24	Contours of (a) $R_{uu}$ and (b) $R_{pp}$ on the cross-sectional plane $x = 7.5D_j$ with reference point on SPS at $\phi = \pi/2$ (white cross). Time shift is zero. . . . .	50
3.25	Isocontours of azimuthal scales (a) $\Phi_u$ and (b) $\Phi_p$ , units are radians. Red line: SPS. White line: radiator surface. . . . .	51
3.26	Axial distribution of azimuthal scales $\Phi$ on the relevant surfaces. Orange solid line: $\Phi_u$ on SPS. Blue dashed line: $\Phi_u$ on the radiator surface. Green dotted line: $\Phi_p$ on the SPS. Black line dash-dot: $\Phi_p$ on the radiator surface. . . . .	51
3.27	Azimuthal scales $\Phi$ versus similarity coordinate $(r - r_i)/\delta_\theta$ , (a) based on axial velocity; (b) based on pressure. Legend applies to both subfigures. . . . .	52
3.28	Isocontours of normalized magnitude of mean vorticity $\bar{\omega}D_j/U_j$ . Black line: radiator surface based on $U_c$ -match criterion. . . . .	56
3.29	Approximation of the radiator surface using $C_\omega = 0.03$ and $C_\omega = 0.125$ . The former value is the best approximation for the single-stream jet, the latter is the optimal value for the three-stream jets of Chapter 4. . . . .	57

3.30	Comparison of LES- and eRANS-derived convective velocities on the radiator surface. . . . .	58
3.31	Fitting of eRANS-based length scales on the radiator surface. (a) Fixed-frame scale with $C_L = 0.76$ ; (b) moving-frame scale with $C_L = 5.65$ and $C_L = 1.65$ for the initial region and for the region past the potential core, respectively. . . . .	59
3.32	Fitting of eRANS-based azimuthal scales on the radiator surface with $C_\Phi = 2.60$ . . . . .	60
4.1	Characteristics of three-stream nozzles. (a) Exit geometry of nozzles; (b) coordinate system; (c) azimuthal variation of the tertiary annulus width. . . . .	65
4.2	Far-field sound pressure level spectra of jets AXI04U (red) and ECC09U (blue) various polar angles $\theta$ with respect to the downstream axis. . . . .	66
4.3	Space-time correlation $R_{uu}$ on the OSPS at $x/\hat{D} = 4$ for jet AXI04U. Dashed lines indicate fits by seventh-order polynomials to accurately detect the peak of each correlation. . . . .	70
4.4	Isocontours of normalized normalized mean axial velocity $\bar{u}/\hat{U}$ on the symmetry plane of jet AXI04U. a) LES and b) RANS. . . . .	71
4.5	Isocontours of normalized normalized mean axial velocity $\bar{u}/\hat{U}$ on the symmetry plane of jet ECC09U. a) LES and b) RANS. . . . .	71
4.6	Isocontours of normalized Reynolds stress $g/\hat{U}^2$ on a symmetry plane of jet AXI04U. a) LES and b) RANS. . . . .	73
4.7	Isocontours of normalized Reynolds stress $g/\hat{U}^2$ on the symmetry plane of jet ECC09U. a) LES and b) RANS. . . . .	74
4.8	Detection of the outer surface of peak Reynolds stress (OSPS) at $x/\hat{D} = 1.467$ for jet ECC09U. Contours indicate the distribution of Reynolds stress on this cross-stream plane. Thin red lines: rays along the mean velocity gradient. Thick red line: OSPS . . . . .	75
4.9	RANS-based OSPS with contours of convective Mach number $M_c$ . . . . .	77
4.10	LES-based OSPS with contours of convective Mach number $M_c$ . . . . .	77
4.11	RANS and LES results regarding the OSPS of jet AXI04U. . . . .	78
4.12	RANS and LES results regarding the OSPS of jet ECC09U on $\phi = 0^\circ$ . . . . .	80
4.13	RANS and LES results regarding the OSPS of jet ECC09U on $\phi = 180^\circ$ . . . . .	81
4.14	Distribution of normalized convective velocity $U_{cp}/\hat{U}$ as determined by space-time correlations based on $p'$ on the meridional planes of jets AXI04U and ECC09U. White lines: radiator surface; red lines: OSPS based on LES. . . . .	83
4.15	Distribution of normalized convective velocity $U_{cu}/\hat{U}$ on the meridional planes of jets AXI04U and ECC09U. The legend is the same as Fig. 4.14 . . . . .	84
4.16	Radiator surfaces and LES-based OSPS with contours of convective Mach number $M_c$ . . . . .	85
4.17	Isocontours of normalized module of mean vorticity $ \bar{\omega} \hat{D}/\hat{U}$ on the meridional planes of jets AXI04U and ECC09U. Black line: radiator surface based on $U_c$ -match criterion. Red line: OSPS . . . . .	86
4.18	Comparison of radiator surface with surface based on the mean vorticity criterion of Eq. 4.4 using the LES flow fields on the three stream jets. . . . .	87

4.19	Comparison of radiator surface with surface based on the mean vorticity criterion of Eq. 4.4 using the LES flow fields on three cross-sectional planes of jet ECC09U. . . . .	88
4.20	Comparison of radiator surface with surface based on the mean vorticity criterion of Eq. 4.4 using the RANS flow fields on the three-stream jets. . . . .	89
4.21	Comparison of radiator surface with surface based on the mean vorticity criterion of Eq. 4.4 using the RANS flow fields on three cross-sectional planes of jet ECC09U. . . . .	90
4.22	Distribution of $p'_{\text{rms}}$ , normalized by the ambient pressure $p_\infty$ , on the radiator surfaces of jets AXI04U and ECC09U at $\phi = 0^\circ$ . . . . .	91
4.23	Distribution of the root mean square of pressure fluctuation on the symmetry plane of jet ECC09U. Black line: radiator surface. Red line: OSPS. . . . .	91
4.24	Distribution of the normalized skewness of the LES pressure field. White lines: radiator surface. . . . .	93
4.25	Pressure time history on the radiator surface of jet AXI04U at $x/\hat{D} = 6$ and $\phi = 0^\circ$ . . . . .	94
4.26	Contour of the instantaneous pressure fluctuation in jet AXI04U at $\phi = 0^\circ$ . Arrows: projection of velocity fluctuation vectors on $x - y$ plane; white line: radiator surface; red line: OSPS surface. . . . .	95
4.27	Distribution of the normalized skewness of the LES axial velocity field. White lines: radiator surface. . . . .	97
4.28	Distribution of normalized correlation between $\omega'_\phi$ and $p'$ , $R_{\omega_\phi p}$ . White lines: radiator surface. . . . .	98
4.29	Contours of $R_{up}$ with reference point $(x_0, r_0) = (2, 0.3)\hat{D}$ for jets AXI04U (left column) and ECC09U (right column) at azimuthal angle $\phi = 0^\circ$ . Time separations: $\tau = -1.92\hat{D}/\hat{U}$ (top row), $\tau = 0$ (middle row), and $\tau = 1.92\hat{D}/\hat{U}$ (bottom row). Red line: SPS. White line: radiator surface. Black dashed vertical line: positions for a downstream convection at velocity $0.6\hat{U}$ . . . . .	100
4.30	Isocontours of normalized fixed-frame length scales based on axial velocity fluctuation, $L_u/\hat{D}$ . Red line: OSPS. White line: radiator surface. . . . .	102
4.31	Isocontours of normalized fixed-frame length scales based on pressure fluctuation, $L_p/\hat{D}$ . Red line: OSPS. White line: radiator surface. . . . .	103
4.32	Isocontours of normalized moving-frame length scales based on axial velocity fluctuation, $\hat{L}_u/\hat{D}$ . Red line: OSPS. White line: radiator surface. . . . .	105
4.33	Isocontours of normalized moving-frame length scales based on pressure fluctuation, $\hat{L}_p/\hat{D}$ . Red line: OSPS. White line: radiator surface. . . . .	106
4.34	Fitting of $L_u$ on the OSPS and RANS-based length scales to the $L_p$ distribution on the radiator surface. . . . .	108
4.35	Fitting of $\hat{L}_u$ on the OSPS and RANS-based length scales to the $\hat{L}_p$ distribution on the radiator surface. . . . .	110
4.36	Isocontours of azimuthal scales based on axial velocity fluctuation, $\Phi_u$ . Red line: OSPS. White line: radiator surface. . . . .	112
4.37	Isocontours of azimuthal scales based on pressure fluctuation, $\Phi_p$ . Red line: OSPS. White line: radiator surface. . . . .	113

4.38	Fitting of $\Phi_u$ on the OSPS and RANS-based azimuthal scales to the $\Phi_p$ distribution on the radiator surface. . . . .	115
5.1	Far field SPL spectrum of jets AXI04U and ECC09U. . . . .	118
5.2	Sketch of noise radiation and point of study of the wavepacket model. . . . .	119
5.3	Peak frequencies of the pressure autospectra on the OSPS and radiator surface of jet AXI04U. RANS-based frequencies are adjusted by $C_f = 0.3$ . . . . .	123
5.4	Results of model calibration to experimental far-field autospectra of jet AXI04U at $\theta = 32.5^\circ$ . (a) Comparison of scaled experimental and modeled autospectra, and (b) real part of the axial distribution $p_0(x)$ . . . . .	128
5.5	Sound pressure levels generated by wavepackets of different length scales, all other parameters equal. . . . .	129
5.6	Comparison of scaled experimental and modeled autospectra using a length scale coefficient of $C_L = 4.0$ . . . . .	130
5.7	Changes in modeled autospectrum generated by changing $C_f$ (left column) or $C_L$ (right column) around point $C_f = 0.6$ and $C_L = 4.0$ . Wavepacket amplitude is $\mathcal{A} = 1$ for all cases. . . . .	132
5.8	Convective velocity distribution $U_c$ (solid line) and values assigned to the modeled wavepackets (circles) for $C_f = 0.6$ . . . . .	133
5.9	Pressure spectra along the radiator surface. The black line denotes the maximum frequency at each axial location. . . . .	134

# LIST OF TABLES

	Page
4.1 Flow conditions. . . . .	66
5.1 Parameters for BEM modeling of jet AXI04U. . . . .	126

# NOMENCLATURE

## Roman symbols

$a$	speed of sound
$A$	duct exit area
$\mathcal{A}$	wavepacket amplitude
$C$	proportionality factor
$D$	nozzle exit diameter
$\widehat{D}$	equivalent diameter (three-stream jets)
$f$	cyclic frequency; sample time-dependant signal (Ch. 3)
$g$	principal component of the Reynolds stress
$k$	turbulence kinetic energy
$L$	fixed-frame length scale
$\widehat{L}$	moving-frame length scale
$\dot{m}$	mass flow rate
$M$	jet exit Mach number
$M_c$	convective Mach number
$p$	pressure
$\mathcal{P}$	pressure function in the frequency domain
$R$	space-time correlation
$S$	autospectra of the pressure signal
$r_i$	radial location of inner edge of mixing layer (single-stream jet)
$Sk$	normalized skewness
$St_D$	Strouhal number based on nozzle diameter
$t$	time
$U$	jet exit velocity
$U_c$	convective velocity
$\widehat{U}$	mass-flow-averaged jet exit velocity (three-stream jets)
$\bar{u}_{CL}$	centerline time-averaged velocity
$u, v, w$	velocity components in Cartesian coordinate system
$W$	annulus width
$x, r, \phi$	cylindrical coordinates, with $x$ on jet axis
$x, y, z$	Cartesian coordinates, with $x$ on jet axis and $y$ on upward vertical.

## Greek symbols

$\delta_\theta$	momentum thickness of the mixing layer
$\epsilon$	turbulence dissipation
$\theta$	polar angle relative to downstream jet axis
$\kappa$	wavenumber
$\lambda$	wavelength
$\nu_T$	turbulent viscosity

$\xi, \eta, \alpha$	displacements in cylindrical coordinates
$\xi, \psi, \zeta$	displacements in Cartesian coordinates
$\rho$	density
$\tau$	time displacement
$\Phi$	azimuthal scale
$\omega$	angular frequency
$\boldsymbol{\omega}$	vorticity vector

## Acronyms

BEM	boundary element method
ICAO	International Civil Aviation Organization
LES	large eddy simulation
NPR	nozzle pressure ratio
NTR	nozzle temperature ratio
OSPS	outer surface of peak Reynolds stress
RANS	Reynolds-Averaged Navier Stokes
SPS	surface of peak Reynolds stress

## Subscripts

$cl$	centerline
$j$	single-stream jet
$p$	based on pressure fluctuation (turbulence scales); primary stream (Ch. 4)
$s$	secondary stream
$t$	tertiary stream
$u$	based on axial velocity fluctuation
$wp$	wavepacket
$\infty$	ambient

## Superscripts

'	temporal fluctuation
—	time-averaged signal (overline)

# ACKNOWLEDGMENTS

I wish to express my gratitude to my advisor, Professor Dimitri Papamoschou, for his dedication, guidance, and support throughout my years at the University of California, Irvine. He built the theoretical foundation for this work and introduced me to the field of aeroacoustics, which will continue to interest me for many years to come.

I would like to thank Pete Balsells, founder of the Balsells Fellowship program, and its director Professor Roger Rangel for funding my first years of graduate school. My experience at UCI, facilitated by the Balsells fellowship, greatly contributed to my personal and academic growth.

The support by NASA Cooperative Agreement NNX14AR98A, monitored by Dr. James Bridges, is gratefully acknowledged. I am indebted to Dr. Christophe Bogey for generously sharing their single-stream jet LES results and invaluable expertise. That single-stream simulation was performed using HPC resources from PMCS2I (Pôle de Modélisation et de Calcul en Sciences de l'Ingénieur et de l'Information) of École Centrale de Lyon and from IDRIS (Institut du Développement et des Ressources en Informatique Scientifique). I also thank Dr. Juntao Xiong and Professor Feng Liu for their collaboration in providing the flow simulations of the three-stream jets.

I would like to express my appreciation to the American Institute of Aeronautics and Astronautics for awarding me the Gordon C. Oates graduate award.

I thank my fellow students Núria Espuga, Claudia López, Kyle Miller, David Morata, Vincent Phong, Jordi Poblador, and Laura Pla for their friendship and helpful discussions.

I also give heartfelt thanks to my parents and my sister for their unconditional, relentless support.

Portions of the text of this dissertation are reprints of the material as it appears in the publications “Investigation of vortical and near-acoustic fields in three-stream jets”, *The Journal of the Acoustical Society of America*, 2021, co-authored by D. Papamoschou and J. Xiong, and “Imprint of Vortical Structures on the Near-Field Pressure of a Turbulent Jet”, *AIAA Journal*, 2022, co-authored by D. Papamoschou and C. Bogey. Permission to use material from the first publication was granted by the Acoustical Society of America. The copyright of the second publication is held by the authors.

# VITA

**Andres Manuel Adam Alberdi**

## EDUCATION

<b>Ph.D. in Mechanical and Aerospace Engineering</b> University of California, Irvine	<b>2022</b> <i>Irvine, California, USA</i>
<b>M.S. in Mechanical and Aerospace Engineering</b> University of California, Irvine	<b>2018</b> <i>Irvine, California, USA</i>
<b>M.S. in Aeronautical Engineering</b> Polytechnic University of Catalonia	<b>2018</b> <i>Terrassa, Catalonia, Spain</i>
<b>B.S. in Aeronautical Engineering</b> Polytechnic University of Catalonia	<b>2016</b> <i>Terrassa, Catalonia, Spain</i>

## RESEARCH EXPERIENCE

<b>Graduate Student Researcher</b> University of California, Irvine	<b>2018–2022</b> <i>Irvine, California</i>
--	---

## TEACHING EXPERIENCE

<b>University of California, Irvine</b> Teaching Assistant for MAE 135: Compressible Flow	<i>Irvine, California</i> 2018-2020, 2022
Teaching Assistant for MAE 130A: Introduction to Fluid Mechanics	2022

## WORK EXPERIENCE

<b>International Centre for Numerical Methods in Engineering (CIMNE)</b> Intern	<i>Terrassa, Catalonia, Spain</i> November 2015 - June 2016
--	--

# ABSTRACT OF THE DISSERTATION

The Very Near Field of High-Speed Jets from Simple and Complex Nozzles

By

Andres Manuel Adam Alberdi

Doctor of Philosophy in Mechanical and Aerospace Engineering

University of California, Irvine, 2022

Professor Dimitri Papamoschou, Chair

This work presents advances towards a linear surface-based model for the jet noise source in simple and complex jets of relevance to the propulsion of high-speed aircraft. The model would be informed by low-cost, Reynolds-Averaged Navier-Stokes (RANS) computations of the flow field. It would be a practical alternative to experiments or high-fidelity computations, such as large eddy simulations (LES), both of which are resource-intensive and entail long turnaround times.

This study encompasses one single-stream and two triple-stream jets. The connection between the vortical field and its pressure signature on the edge of the jet is investigated. These regions are represented by the surface of peak Reynolds stress (OSPS) and the “radiator surface” respectively. The radiator surface is the location where the jet noise source model would be prescribed for the computation of its noise propagation.

The single-stream jet is an isothermal round jet at Mach 0.9 calculated by large eddy simulation (LES), which enables the computation of two-point space–time correlations throughout the jet and its near-acoustic field. It is observed that the nature of the space–time correlations is different for axial velocity fluctuations and pressure fluctuations. Velocity-based correlations appear to capture localized turbulent events, whereas pressure-based correla-

tions appear dominated by the interaction of large eddies with the surrounding potential flow.

Of the triple-stream jets, one is coaxial and the other has an eccentric tertiary flow that yields nose suppression in preferred directions. They are computed by LES and RANS and used to verify key modeling assumptions. In particular, the analysis of velocity scales obtained by two-point correlations validates the RANS-based models for the convective velocity  $U_c$  of the noise-generating turbulence, which is a crucial factor in noise generation.

The radiator surface is located near the boundary between the rotational and irrotational fields and is defined as the surface on which the  $U_c$  distribution equals that on the OSPS. The edge of mean vorticity is nearly coincident with the radiator surface, which suggests a straightforward RANS-based criterion for locating this surface. Additionally, it is found that the edge of the jet is affected by sparse vortices that peel off from the main flow and travel along the radiator surface. Those vortices represent the last remnants of the vortical field and cause a layer of negative pressure skewness at the edge of the jet.

Axial and azimuthal turbulence scales are examined on the OSPS and the radiator surface of the three jets, and compared with scales extracted from RANS. Simple relationships are inferred that may aid the development of rapid predictive models.

# Chapter 1

## Introduction

### 1.1 Motivation

Aircraft noise is today one of the most common sources of noise pollution, particularly in cities and areas near airports. Noise pollution creates an important impact on the quality of life of individuals affected and can cause serious and long term harm to their health. Exposure to aircraft noise has been associated to annoyance, sleep disturbance, cardiovascular diseases, and a reduction in cognitive performance, among other harmful effects [6, 53, 69]. Further, these effects create an economic impact in the form of housing value loss and restrictions in airport operations that has been estimated to surpass 30 billion in housing value loss [45].

The Federal Aviation Administration started restricting noise generation in 1969 for new civil subsonic jet aircraft designs in 1969. New and harsher noise regulations have been implemented in the years afterwards, making aircraft noise generation one of the most pressing issues facing the aerospace industry today [50].

Recent efforts to bring back commercial supersonic aviation, currently nonexistent since the retirement of the Concorde in 2003, make noise reduction crucial. The engines that power supersonic aircraft need to be powerful to bring it to supersonic speeds and slim to reduce its sonic boom. As a result, they have small bypass ratios and lose the noise-reducing effects of thick secondary flows, prompting engineers to search for new alternative noise mitigating technologies. A typical design process is iterative and needs rapid turnaround times of all its steps, including that of noise assessment. However, first-hand methods such as experimental testing or high-fidelity simulations are resource-intensive and entail long turnaround times. A practical alternative for rapid jet noise predictions is to base them on Reynolds-averaged Navier-Stokes (RANS) simulations, which is the focus of this work.

Obtaining noise predictions out of RANS simulations implies the modeling of the turbulent jet noise sources, on which they are replaced by equivalent sources built from the information that can be extracted from time-averaged data. There are different methods of noise source modeling, its main examples being volumetric models and surface-based models. This work focuses on the development of latter type, as it constitutes a simple approach to multi-stream and asymmetric jets.

Efforts to increase the efficiency and to achieve a higher noise reduction of aircraft engines have led to complex nozzle geometries such as three-stream and asymmetric jets, which our research group at the University of California, Irvine has studied extensively [81, 84]. For such complex geometries, the surface-based models simplify the treatment of their azimuthal directivity with respect to volumetric models. In addition, linear-based models allow not only propagation but also scattering predictions (e.g. from airframe surfaces) using well-established techniques like the boundary element method [73, 78]; thus, they have the capacity to address the acoustics of propulsion-airframe integration.

The backbone of RANS-based modeling is the understanding of noise generation mechanisms, which allows to reconstruct the effects of the noise-generating turbulence from their

effects on the mean flow provided by RANS simulations. This connection between time-resolved flow and time-averaged data is often postulated by assumptions that need thorough verification. This work aims to investigate the correct modeling of jet noise sources and obtained a low-cost prediction tool applicable to complex, multi-stream jets.

## 1.2 Research Objectives

The research presented in this work is directed towards the development of a linear surface-based wavepacket model for the jet noise source of complex multi-stream jets. This model is informed from the RANS solution of the flow field. The project involves the study of a single-stream jet with highly resolved LES, as well as two three-stream jets with LES and RANS simulations. The following objectives are established:

- Process the LES data of the single-stream jet and visualize its flow field.
- Study the LES flow field of the single-stream jet with the goal of understanding and quantifying the effects of turbulent structures on the near pressure field.
- Process RANS and LES data of the three-stream jets and compare their flow fields with emphasis on the mean velocity and the Reynolds stress.
- Verify the RANS-based model for the convective velocity of the noise-generating turbulence structures.
- Investigate the physics of length- and time-scales of the LES flow field and assess the approximation of those scales using RANS.
- Assess the implementation of the aforementioned concepts into a simplified model for the jet noise source.

## 1.3 Thesis Overview

The following dissertation is presented in six chapters.

- **Chapter 1** presents the motivation and overall objective of this work.
- **Chapter 2** outlines the theoretical background of jet noise generation and modeling that constitutes the basis of this work.
- **Chapter 3** presents the study of a single-stream jet computed through LES. It includes the overview of its flow field, computations of flow velocity and spatial scales, and their modeling from time-averaged results.
- **Chapter 4** studies the LES and RANS simulations of two three-stream jets. Particular emphasis is placed on the flow features near the surfaces relevant to wavepacket modeling, the OSPS and the radiator surface.
- **Chapter 5** presents a simplified wavepacket model that aims to recreate the peak noise emission of a three-stream jet while being informed from its RANS flow field.
- **Chapter 6** summarizes the work completed and gives recommendations for future work.

# Chapter 2

## Literature Review

### 2.1 Sources of Jet Noise

The term “jet noise” comprises three different phenomena: turbulent mixing noise, broadband shock-associated noise, and screech tonal noise. The latter two are only found in jets with imperfectly expanded exit conditions, and the former is present in jets at all operating conditions [103]. Figure 2.1 shows an example of a noise spectrum of a non-perfectly expanded supersonic jet measured experimentally by Seiner [97], which contains all three noise phenomena. In this figure, the sound pressure level (SPL) is plotted versus the non-dimensional frequency, also known as Strouhal number  $St$ . The peak of noise level near  $St = 0.4$  can be identified as a screech tone, and often appears with more than one harmonic. To its right dominates broadband shock associated noise, and to its left is the turbulent mixing noise. The frequency and intensity of these three natures are determined by the jet operating conditions, nozzle geometry, and observer position. The following paragraphs will briefly explain their characteristics and justify our focus on the turbulent mixing noise.

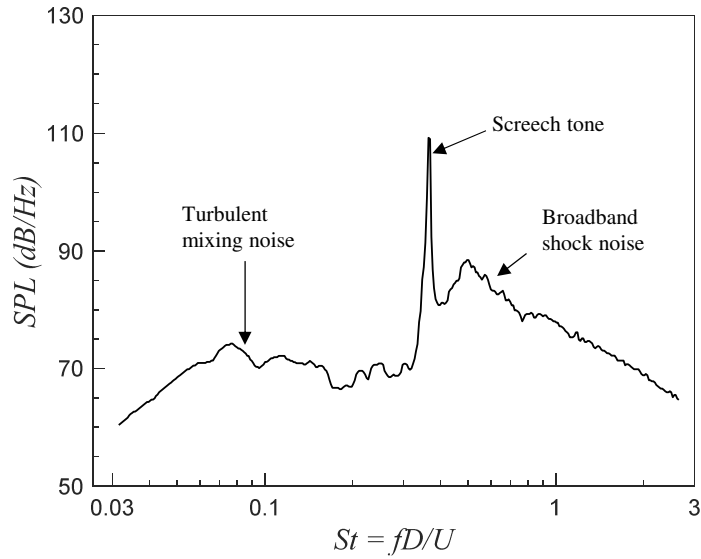


Figure 2.1: Far field noise spectrum of an overexpanded jet at a Mach number of 1.5. The microphone is at  $150^\circ$  to the downstream jet axis. Data from Seiner [97].

Broadband shock-associated noise and screech tones occur on certain operating conditions of supersonic jets. Under supersonic conditions, the static pressure at the nozzle exit can be different than the ambient pressure. This difference can generate wave phenomena at the nozzle lip, which reflects downstream forming a cell-like pattern named shock-cell structure. Broadband shock-associated noise is generated by the non-linear interaction between the downstream propagating coherent turbulence structures and the shock cells. Screech tones are believed to be product of a feedback mechanism that starts with acoustic disturbances exciting the thin jet mixing layer near the nozzle lip. The amplitude of this instability grows with downstream propagation and interacts with the shock cells in the jet plume. This interaction creates acoustic radiation that travels upstream and excites the shear layer near the nozzle, closing the feedback loop [103]. While these two noise mechanisms are common in military aviation, civil applications rarely present imperfectly expanded jets. As this work focuses on civil applications, we will only consider the remaining noise type: turbulent mixing noise.

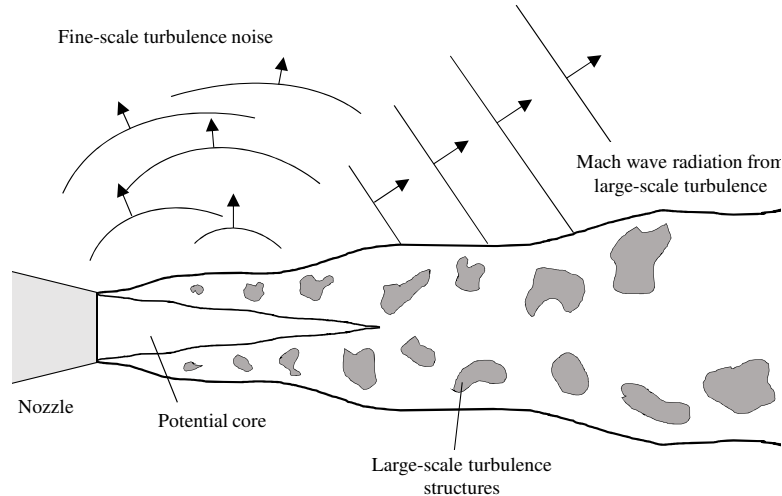


Figure 2.2: Diagram showing the turbulent mixing noise generation mechanisms in a single-stream jet.

## 2.2 Turbulent Mixing Noise

Turbulent mixing noise is generally understood as the noise generated by the turbulence within a jet. Turbulence is characterized by stochastic fluctuations in pressure and flow velocity [7]. Despite being chaotic, it is not completely random: Crow and Champagne [34] and Brown and Roshko [27] were among the first to prove the existence of coherent, large-scale turbulence structures in turbulent jets and two-dimensional shear layers. These structures convect downstream and coexist with small-scale, more isotropic eddies. An extensive analysis by Tam *et al.* [106] on the turbulent noise generated by many jets at different operating conditions divided it into two basic components: one generated by small-scale and another by large-scale structures. A schematic representation of these mechanisms is shown in Fig. 2.2. The small-scale turbulence is thought to be omnidirectional in its noise generation, while large-scale structures cause strongly directional noise which peaks at shallow angles with the jet downstream direction. While this attribution is the prevalent model, it is sometimes argued that the existence of two uncorrelated noise sources lacks conclusive proof [76].

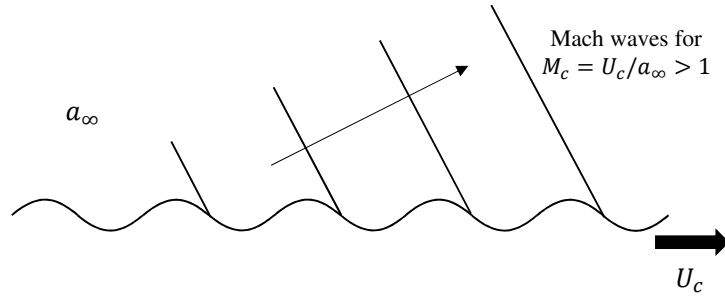


Figure 2.3: Mach wave emission in the case of a wavy wall moving with velocity  $U_c$  supersonic with respect to the ambient speed of sound.

Today, it is well accepted that the peak turbulent noise is caused by large-scale turbulence structures in both subsonic and supersonic jets [33, 52, 64, 104]. They cause highly directional noise as they travel downstream. A basic tool to understand their noise generation is to simplify the interface between the jet and the ambient to a wavy wall moving downstream next to a still fluid[105]. If the wall moves with supersonic velocity, it radiates Mach waves at low angles from the downstream direction as shown in Fig. 2.3. This would be the case for a instability wave moving with a speed that is supersonic relative to the ambient fluid.

Continuing with the wavy wall analogy, it is evident that an infinite periodic wavy wall moving at subsonic speeds would generate flow perturbations that quickly decay into the ambient. This is not the case for subsonic turbulent flows. The difference relies on the fact that turbulence structures have finite length, contrary to the infinite wall. Near the nozzle exit, the shear layer is thin and the mean-velocity gradient is large enough to cause linear instabilities to grow rapidly as they convect downstream. At later flow stages, the shear layer thickens and the mean-velocity gradient reduces, which slows the growth of the linear instabilities until they stop growing, experience damping, and disappear. This process can be translated to the wavy wall analogy by adding a growth and decay of the wall “waves” acquiring the form of a “wavepacket”. Let  $\eta(x, t)$  describe the vortex sheet between the jet

and a quiescent ambient or, in the wavy wall analogy, the shape of the wavepacket being

$$\eta(x, t) = \mathcal{A}(x) \exp\{i(\kappa_x x - \omega t)\} \quad (2.1)$$

where  $x$  is the axial position,  $t$  is the time,  $\kappa_x$  is the wavepacket wavenumber,  $\omega$  is the wavepacket frequency and  $\mathcal{A}$  is the envelope of the oscillations which determines the spatial length scale of the perturbation. A visualization of the wavepacket shape of Eq. 2.1 is depicted in Fig. 2.4.  $U_c$  is the speed at which the instability moves downstream, named convective velocity, and is related to Eq. 2.1 by

$$U_c = \frac{\omega}{\kappa_x} \quad (2.2)$$

The convective Mach number of the instability wave is

$$M_c = \frac{U_c}{a_\infty} \quad (2.3)$$

When the amplitude  $\mathcal{A}$  is constant, the instability radiate far-field sound only if  $M_c > 1$ . When  $\mathcal{A}$  is not constant, it is useful to consider the wavepacket shape  $\eta$  as a superposition of traveling waves in the axial Fourier space as

$$\eta(x, t) = \frac{1}{2\pi} \int_{-\infty}^{\infty} \hat{\mathcal{A}}(\kappa - \kappa_x) \exp\{i(\kappa x - \omega t)\} d\kappa \quad (2.4)$$

Thus, each individual wave has an amplitude in the Fourier space of  $\hat{\mathcal{A}}(\kappa - \kappa_x)$  and convective velocity of

$$U_{c,i} = \frac{\omega}{\kappa} \quad (2.5)$$

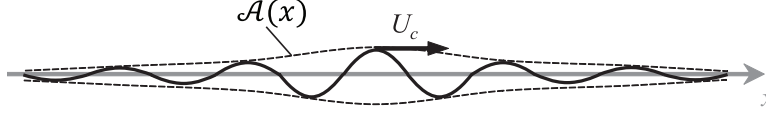


Figure 2.4: Wavepacket shape moving at  $U_c$  with envelope defined by  $\mathcal{A}(x)$

This means that the effect of growth and decay of instabilities transform a simple fluctuation of discrete wavenumber  $\kappa_x$  and convective velocity  $U_c$  into a wider wavenumber spectrum of waves traveling at different convective velocities. The convective Mach number for each wave is then

$$M_{c,i} = \frac{\omega}{\kappa a_\infty} \quad (2.6)$$

These results mean that even though  $M_c$  given by Eq. 2.3 is subsonic, the spectrum of the waves conforming the wavepacket may have components of supersonic convective speed  $|\kappa| \leq \omega_{wp}/a_\infty$  that generate Mach wave radiation into the far field. We can identify the region of  $|\kappa| \leq \omega_{wp}/a_\infty$  as the acoustic component, which can be heard by an observer in the far field. The remaining range of  $|\kappa| > \omega_{wp}/a_\infty$  is the hydrodynamic component, which decays rapidly outside the jet.

It can be concluded that the growth and decay of turbulence structures is a critical factor to their noise generation, and a basic mechanism by which subsonic flows radiate noise. In round jets, turbulence noise is mainly generated in the first few diameters from the nozzle exit and at the end of the potential core [9], where there are strong gradients that generate and dissipate turbulence eddies.

The growth and decay mechanism is associated with length and time scales of turbulence flows, which have received notable attention in the literature. We can highlight the measurements obtained by hot-wire anemometry of Harper-Bourne [44] and Morris and Zaman [71], which are frequently used to inform jet noise source models. More recently, Proença *et*

*al.* [92] performed a comprehensive hot-wire investigation in the shear layer of various unheated single-stream jets. Studies have also been performed using particle image velocimetry (PIV), such as those by Fleury *et. al.* [40] and Pokora and McGuirk [89], which have provided valuable, detailed information on the correlations of the velocity field. However, past works have focused primarily on the jet lip line and centerline and provide little information on turbulent scales near the edge of the jet. This motivates the present work, where we seek physical connections between flow scales in the vortical field and at the edge of the jet.

## 2.3 Physics of Multi-Stream Jets

Two-stream turbofan engines now account for the majority of commercial and military engines. These engines not only provide better fuel efficiency, but also a significant reduction in noise. The presence of a slower secondary flow surrounding the primary stream can diminish the Mach wave radiation of the jet by lowering the values of the convective Mach  $M_c$  of the turbulent structures responsible for their production [72].

The essential features of a two-stream jet flow are shown in Fig. 2.5 from Papamoschou [72]. A common feature at the exit of jets is the presence of a potential core, which is a region with relatively low vorticity. It is surrounded by a turbulent shear layer, which is the result of the velocity difference between the jet and the surrounding media. For this case of a dual-stream jet, both streams have an initial potential core that vanishes as the shear layers grow. A primary shear layer can be identified between the primary and secondary cores, and a secondary shear layer exists between the secondary core and the ambient air. The inflection points in mean velocity  $i_2$  and  $i_3$  determine the secondary core.

For velocity ratios of relevance to the exhaust of turbofan engines, sound emission is thought to be strongly influenced by the dynamics of the outer shear layer in the initial

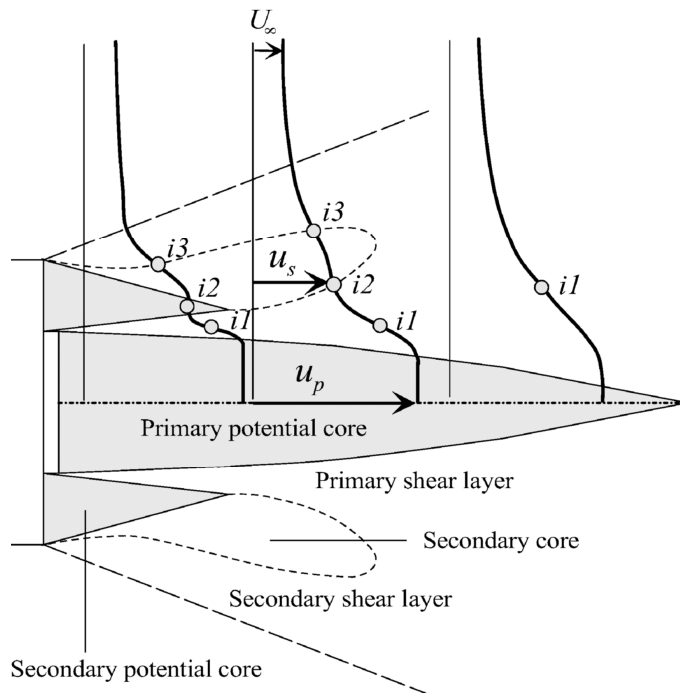


Figure 2.5: Basic elements of a two-stream jet, from Papamoschou [72].

region of a multi-stream jet. Support for this idea comes from the modeling of coaxial jet noise by Tanna and Morris [109] and Fisher *et al.* [39]. A number of additional works have validated and refined this concept, including experiments on mean velocity profiles and noise source location [82] and near-field pressure measurements [79, 110]. Considering the entire jet, we can generalize this observation by stating that the turbulent eddies in contact with the ambient air are the main generators of noise. In the case of multi-stream jets, this means that the inner shear layers are mostly silent.

Three-stream arrangements for turbofans, which improve the efficiency and stability of the engine cycle[99], have become available in advanced engine architectures in recent years. These arrangements appear to be key for low-noise supersonic transport. The acoustic and hydrodynamic dynamics of these jets have gained a lot of interest in recent experimental and numerical studies [46–48, 74, 81]. The presence of secondary and tertiary flows also widens the range of possible noise reduction mechanisms in the form of modifications of

the exhaust nozzle. Such modifications have included chevrons [26, 110], fluidic injections [36, 91], plasma excitation [95], and asymmetric nozzle geometry [77, 81].

## 2.4 Modeling of Jet Noise

### 2.4.1 Acoustic Analogies

The work of Lighthill [58] is widely accepted as the birth of modern aeroacoustics. His work rearranges the governing equations of fluid motion into a form similar to a wave equation, which directly connects a jet’s turbulent motions with the sound radiated into a quiescent medium.

$$\frac{\partial^2 \rho'}{\partial t^2} - a_\infty^2 \nabla^2 \rho' = \frac{\partial^2 T_{ij}}{\partial y_i \partial y_j} \quad (2.7)$$

The left hand side of Eq. 2.7 can be identified as a wave operator for  $\rho'$ . The term  $T_{ij}$  is the Lighthill stress tensor, defined as

$$T_{ij} = \rho u_i u_j + (p - a_\infty^2 \rho) \delta_{ij} - \tau_{ij} \quad (2.8)$$

where  $\delta_{ij}$  is the Kronecker delta and  $\tau_{ij}$  is the viscous stress tensor. The right hand side of Eq. 2.7 acts as a source term composed from turbulence interactions. Even though those terms appear as mathematical sources, there is no physical proof that they are the mechanisms by which jet noise is generated, hence the expression “acoustic analogy” to denote Lighthill’s approach. Owing to the double-divergence of the right hand side, Lighthill characterized the source term as a distribution of quadrupoles.

The first term of Eq. 2.8, named the turbulence self-interaction, dominates over the other terms on free jets at high Reynolds numbers. Through dimensional analysis, Lighthill found

that turbulence self-interaction causes a dependence of the far-field sound intensity with the eight power of the jet exit velocity [58]. This important relation has received a lot of attention and is the basic principle for noise reduction in engines with high bypass ratio. Viswanathan [112] showed that the overall sound power does not exactly follow the 8th power law and has a weak dependence on the jet temperature ratio, but it is close nonetheless. This is an indication that although the analogy models are often impractical to use for low-cost noise prediction, they can help identify the salient characteristics of noise generation.

There have been various theoretical developments and adaptations of the underlying theory since the creation of the acoustic analogy [113]. One can highlight the early contributions of Lilley [59], who developed an acoustic analogy that accounts for the effects of mean flow refraction and has been the base for many later models, as well as the model of Ffowcs Williams [41], which included the effects of moving sources and extended Lighthill's theory to sonic and supersonic Mach numbers. These considerations led to the well-known directivity of the Mach wave radiation towards the polar angle  $\theta = \arccos(1/M_c)$ .

Including the flow refraction is particularly critical for asymmetric jet configurations with azimuthal directivity of their acoustic emission, which are often sought to be silent on the downwards and sideline directions [81]. The complexity of those flows requires for complicated numerical procedures to construct the necessary Green's functions [57]. Application to three-stream jets with offset tertiary duct has shown initial promise [48], although the asymmetry in the modeled azimuthal directivity was weaker than the experimental one. More recently, Papamoschou [74] proposed an alternative methodology where the azimuthal influence is induced by special forms of the space-time correlations of the Lighthill stress tensor. Papamoschou's work also underscored the importance of properly modeling the convective velocity  $U_c$  of the turbulent eddies that dominate sound production, which is an important concept that greatly influenced this dissertation.

## 2.4.2 Surface-based models

Surface-based modeling is an alternative to the acoustic analogies where flow analysis and noise propagation are separated. The effects of the noise sources contained within the non-linear flow field are translated to an enclosing surface region. That surface is then treated as the source of noise radiation in a separate computation of propagation. This methodology is common for far-field noise predictions of large eddy simulations and other well-resolved computations [65] because they do not need to include a far-field observer within the computational domain. For simple surfaces (e.g., cylindrical or conical) analytical formulations of the surface Green's function can be used to propagate to the far field [108]. For complex surfaces, the problem can be tackled numerically by a variety of methods, including the boundary element method (BEM)[67]. These methods require time-resolved information of the non-linear flow enclosed by the surface, which makes them costly from a design perspective.

A low-cost approach to the surface-based methods is to use simple models for the surface source instead of raw time-resolved information. In several of these models for jet noise, the surface source takes the form of pressure partial fields, each partial field being an amplitude-modulated traveling wave (wavepacket), which aim to replicate the noise-generating effects of turbulence explained in Subsection 2.2. The acoustic field can then be constructed via stochastic superposition of the pressure field emitted by each wavepacket. Such constructions can be found in the works of Morris [70], Reba *et al.* [93], and Papamoschou [75, 76]. Reba *et al.* [93] used near-field data to formulate a wavepacket field and propagated its noise effects to the far-field. Papamoschou [75, 76] constructed a set of stochastic wavepackets that replicated the far-field noise from a single-stream jet.

An advantage of the surface approach is that one can predict not only far-field propagation from the jet but also scattering from airframe surfaces [73, 85], thus addressing the acoustics

of propulsion-airframe integration. Surface-based models may also simplify the treatment of the azimuthal directivity from asymmetric jets noted above.

Ultimately, it is desired that the set of wavepackets prescribed on the surface are informed by low-cost RANS simulations. The complexity of multi-stream jet flow fields makes this a challenging proposition. Before such model can be envisioned, we need to better understand and model the relation between the inner vortical field and the linear pressure field at the edge of a jet, which is the motivation for this work.

### **2.4.3 Present model**

The present work is greatly influenced by the model envisioned by Papamoschou in Refs. [74–76]. It is a surface-based model that prescribes a set of partial fields on a surface enclosing the non-linear region of the flow, as shown in Fig. 2.6. Those partial fields model the effects of large-scale turbulent structures in the jet region, convecting downstream and mixing with an inherent stochastic nature. The enclosing surface acts as a radiator in BEM computations, and is therefore named the “radiator surface”. For its role in the BEM computation, it can also be identified as a Kirchhoff surface. The partial fields are informed from RANS simulations through modeling assumptions based on physical principles. The sections below outline the main characteristics and modeling procedures of this method.

#### **Radiator surface**

For a computation of the noise propagation, any surface that does not contain the vortical field and correctly accounts for the pressure events in that location can be used as a source. However, there is only a thin region outside the jet that contains the full information emitted, that is, both acoustic and hydrodynamic components of pressure. The latter is considered the

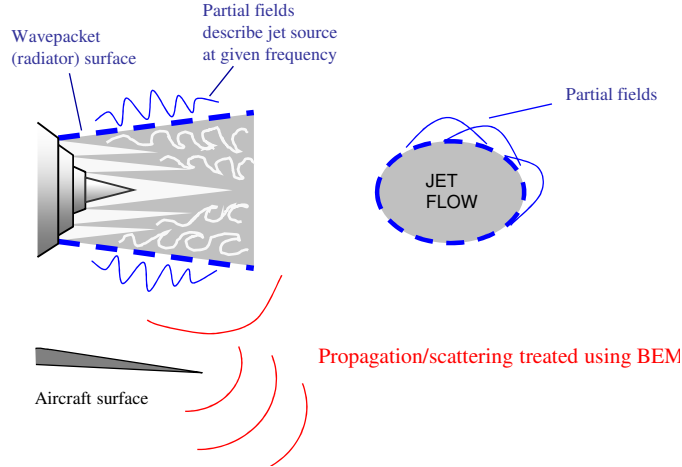


Figure 2.6: Basic elements of surface-based modeling of the jet noise source.

signature of the turbulence eddies of the jet and decays rapidly outside of it. Therefore, that region is the connection between the turbulence field and the linear pressure field, defined as the *edge* of the jet. Because in this model the radiator surface is built based on the effects of turbulent structures, it should be placed on that edge. Notable inaccuracies in its placement can be considered to have negligible effect on far-field noise in free space propagation, but they might have an important effect on near-field noise and scattering applications.

## Modeling of Convective Velocity

It was established above that the convective velocity of noise sources is crucial in their noise generation, and therefore should be well modeled. Direct calculation of the velocity of turbulent structures is impossible from the time averaged data given by RANS simulations, so it needs to be modeled from the information available. We can consider that turbulence eddies are important mechanisms of transport of quantities such as momentum, heat, species, and so on across the jet. Regarding the momentum transport, that is a variable that can be captured, in a time-averaged sense, by the velocity correlation  $\overline{\mathbf{u}'\mathbf{u}'}$ , or the associated Reynolds stress tensor  $-\overline{\rho\mathbf{u}'\mathbf{u}'}$ . It is postulated by Papamoschou [74] that the turbulent

structures induce the largest contributions in, and therefore are best represented by, the Reynolds stress. We model it with the constitutive relation that defines the backbone of turbulence modeling [62]

$$\overline{u'_i u'_j} = \frac{2}{3} k \delta_{ij} - \nu_T S_{ij} \quad (2.9)$$

where  $k$  is the turbulence kinetic energy,  $\nu_T$  is the turbulent viscosity, and  $S_{ij}$  is a tensor determined by the spatial derivatives of the time-averaged velocity field,

$$S_{ij} = \frac{\partial \bar{u}_i}{\partial x_j} + \frac{\partial \bar{u}_j}{\partial x_i} \quad (2.10)$$

The dominant component of the tensor  $S_{ij}$  is not necessarily along a coordinate axis, but rather along the gradient of mean velocity. The flow is mostly an axial movement and it diverges slowly, so the contribution of axial derivatives will be minor. The approximate magnitude of the dominant component of  $S_{ij}$  is

$$G = \sqrt{\left[\frac{\partial \bar{u}}{\partial y}\right]^2 + \left[\frac{\partial \bar{u}}{\partial z}\right]^2} \quad (2.11)$$

where  $y$  and  $z$  are part of a Cartesian coordinate system  $\mathbf{x} = (x, y, z)$ ,  $x$  is the axial centerline of the jet in the downstream direction and  $y, z$  are transverse components.

From Eqs. 2.9 and 2.11, it can be assumed that the principal turbulent transport is in the direction of the mean flow gradient. We can define a turbulent velocity fluctuation  $q'$  along the transverse gradient of mean velocity. The corresponding correlation of  $q'$  with axial velocity  $u'$  is

$$g = \overline{u'q'} = \nu_T G \quad (2.12)$$

The correlation  $g$  is considered the main contributor to the transport and hence to the Reynolds stress. In this work, we refer to  $g$  with the loose term “Reynolds stress” and treat it as non-negative.

As mentioned in section 2.3, the outermost turbulent eddies are the main contributors to Mach wave radiation and its associated peak noise. Accordingly, it is defined the outer surface of peak stress (OSPS) as the locus of the peak Reynolds stress as one approaches the jet from the ambient towards the jet axis. Denoting the radial location of the OSPS as  $r_{OSPS}(x, \phi)$ , the convective velocity of the turbulent eddies is modeled as the mean axial velocity at the OSPS, or

$$U_c(x, r, \phi) = \bar{u}(x, y_{OSPS}(x, \phi), \phi) \quad (2.13)$$

A schematic visualization of this modeling approach is shown in Fig. 2.7. The OSPS, in orange color, is the location of the maximum Reynolds stress, assumed to be linked to noise generating, large-scale eddies moving with velocity  $U_c$ . As the outer shear layers dissipate or mix with the inner layers, the OSPS deflects inwards. Later, it expands with the slow divergence of the jet. Equation 2.13 for the modeling of the convective velocity is one of the most critical assumptions in RANS-based modeling, and verifying it is one of the goals of this work.

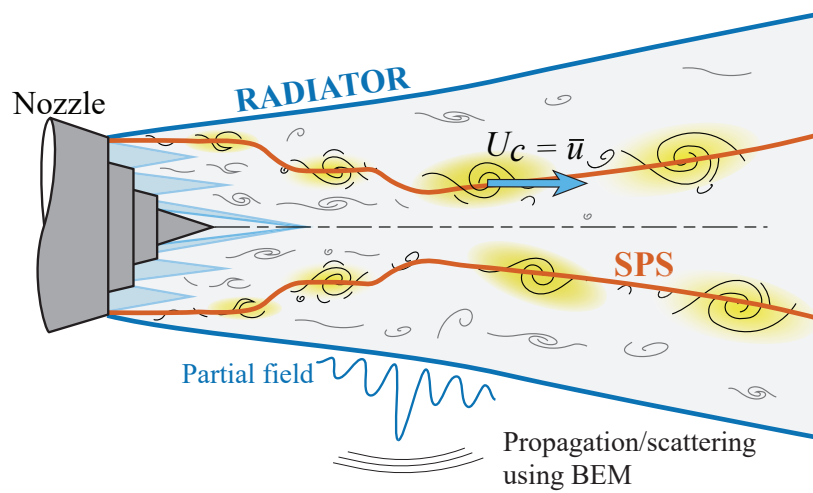


Figure 2.7: Representation of the wavepacket model for a multi-stream jet.

# Chapter 3

## Study of a Single-Stream Jet

This chapter presents the study on a single-stream jet. It includes the specification of the parameters of the flow and its numerical simulation, which is a well-resolved LES. Visualization of the flow field helps define the surfaces relevant for noise source modeling, namely the surface of peak stress (SPS) and the radiator surface. Then, length and velocity scales are studied across the flow field, with particular emphasis on their distributions along the two relevant surfaces. Lastly, the scales associated with an emulated RANS solution of the flow are compared to the LES-based scales and simple relationships are inferred to aid the development of rapid predictive models.

### 3.1 Jet Flow

#### 3.1.1 Jet Parameters

We consider an isothermal, single-stream round jet at velocity  $U_j = 309$  m/s, Mach number  $M_j = 0.9$  and diameter-based based Reynolds number  $Re_D = 10^5$ . The jet originates

from a pipe of constant diameter  $D_j$  and thickness  $0.053D_j$ . It discharges into air with temperature  $T_\infty = 293$  K and pressure  $p_\infty = 10^5$  Pa. This jet has been studied in previous works [1, 8, 10, 11, 20, 22]. We use a cylindrical  $(x, r, \phi)$  and a Cartesian coordinate system  $(x, y, z)$  where the axis  $x$  is the pipe axis and is positive towards the downstream direction. The pipe exit is at  $x = 0$ .

The pipe flow originates at  $x = -D_j$ , where a Blasius laminar boundary-layer profile of thickness  $\delta = 0.075D_j$  is imposed for the axial velocity. In addition, radial and azimuthal velocities are set to zero, pressure is equal to its ambient value, and the temperature is resolved by a Crocco-Busemann relation. The jet is initially disturbed by adding random low-level vortical structures uncorrelated in the azimuthal direction at  $x = -0.475D_j$  inside the pipe [20]. The forcing strength is empirically set to match the nozzle-exit conditions measured in a tripped jet by Zaman [116]. The resulting mean axial velocity profile is very similar to the laminar profile imposed at the nozzle inlet, while the rms velocity profile shows peak axial turbulence intensity  $u'/U_j = 0.0914$ . More details on the tripping process of this jet are given by Bogey *et al.* in Ref. [20].

### 3.1.2 Numerical Methods

The computational code solves the three-dimensional Navier-Stokes equations in cylindrical coordinates  $(x, r, \phi)$  using low-dissipation and low-dispersion explicit schemes. The singularity at the axis is solved by the method of Mohseni and Colonius [68]. The region near the axis also presents a restriction in time-step that is alleviated by calculating the azimuthal derivatives at coarser resolutions than those permitted by the grid [18], yielding an azimuthal resolution of  $2\pi/16$ . Spatial discretization is performed by fourth-order eleven-point centered finite differences, and time integration is carried out using a second-order six-stage Runge-Kutta algorithm [13]. The flow variables are filtered every time step by a sixth-order

eleven-point centered explicit filter [17]. The numerical framework for this LES has been used in many works by the research group of the École Centrale de Lyon [8, 10–12, 19–23].

The explicit filtering used in this simulation has the dual purpose of removing grid-to-grid oscillations and of performing as a subgrid-scale high-order dissipation model for the regions where the mesh grid is not fine enough to capture the smallest scales of turbulence. Filters and non-centered finite differences are also used near the pipe walls and grid boundaries. In order to avoid acoustic reflections, the boundaries are treated with the radiation conditions of Tam and Dong [107]. Additionally, the outflow boundary uses a sponge zone combining grid stretching and Laplacian filtering. The effectiveness of this numerical framework has been assessed in previous studies in diverse cases including subsonic jets, Taylor-Green vortices and turbulent channel flows [14, 15, 20, 38, 55], where it has been compared against direct numerical simulations and the properties of the filtering dissipation have been examined.

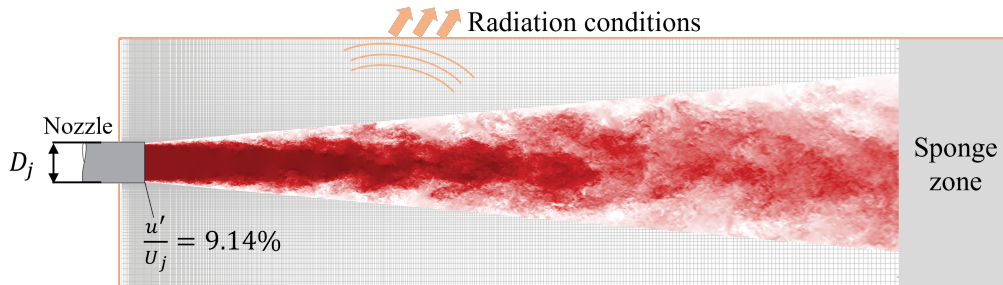


Figure 3.1: Visualization of the single-stream jet over the numerical grid, with its boundary conditions. The jet contour plots instantaneous axial velocity from 0 (white) to  $U_j$  (red).

### 3.1.3 Simulation Parameters

The simulation presented is a highly-resolved LES. The mesh grid contains  $n_x \times n_\phi \times n_r = 2085 \times 1024 \times 512$  points, and its physical extents are  $20D_j$  and  $7.5D_j$  in the axial and radial dimensions respectively. The minimum mesh spacings are equal to  $\Delta r = 0.0018D_j$  at  $r = D_j/2$  and  $\Delta x = 0.0036D_j$  at  $x = 0$ . The maximal mesh spacing in the jet near field is equal to  $\Delta r = 0.0375$ , leading to a Strouhal number of  $St_D = fD_j/U_j = 5.9$  for an acoustic

wave discretized by five points per wavelength, where  $f$  is the frequency. The characteristics of this jet are reported in detail by Bogey in Ref. [8], where a grid-sensitivity study of the jet flow and acoustic fields is carried out, as well as in Ref. [11], in which the acoustic tones emerging near the nozzle are analyzed.

The simulation was performed with an OpenMP-based solver using a time step  $\Delta t = 0.7 \times \Delta r_{min}/a_\infty$  to ensure numerical stability. The simulation had an initial transient period of  $87.5D_j/U_j$ . The simulation time after the transient period is equal to  $1250D_j/U_j$ . During the stationary time, density, velocity components and pressure are recorded at a sampling frequency of  $St_D = 12.8$  in eight equidistant azimuthal angles. Their Fourier coefficients in the azimuthal directions, estimated over the full section  $(x, r)$ , are also saved for the first nine azimuthal modes. The statistics are averaged in the azimuthal direction, when possible. The size of the database amounts to approximately 6.5 TB. Previous work on this simulation has reported good agreement with experimental results of similar jets [17].

## 3.2 Scales in LES Flow Field

### 3.2.1 Space-Time Correlations

Axial length and velocity scales are computed using two-point, space-time correlations. On a meridional plane, the normalized space-time correlation of zero-mean variable  $f$  with reference the point  $(x, r)$  is

$$R_{ff}(x, r; \xi, \eta, \tau) = \frac{\overline{f(x, r, t) f(x + \xi, r + \eta, t + \tau)}}{\left(\overline{f^2(x, r, t)} \overline{f^2(x + \xi, r + \eta, t)}\right)^{1/2}} \quad (3.1)$$

where overline denotes time averaging. The variable  $f$  represents the fluctuating axial velocity or pressure, yielding  $R_{uu}$  or  $R_{pp}$ , respectively.

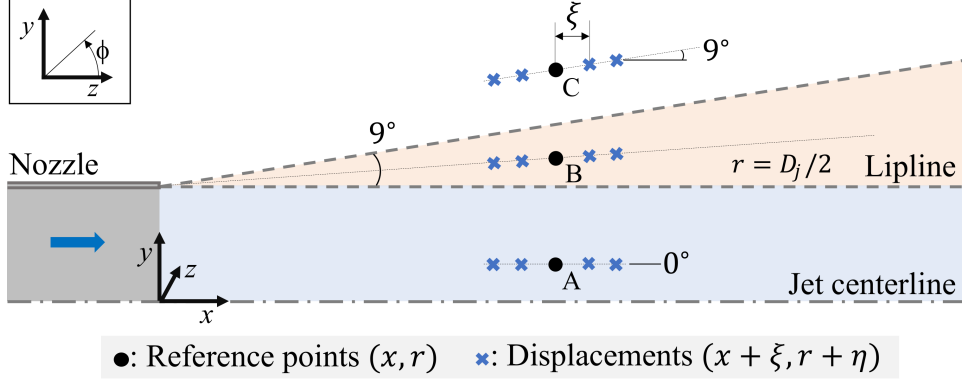


Figure 3.2: Examples of stencils used in the determination of length scales. Reference points are located (A) between centerline and lipline, (B) between lipline and  $9^\circ$  edge, and (C) outside  $9^\circ$  edge.

The space-time correlations are computed using a linear stencil centered around a reference point  $(x, r)$ . Even though axial correlations are sought, care must be taken that the stencil does not connect dissimilar regions of the jet. This is of particular relevance to the computation of length scales near the edge of the jet, where the transition from hydrodynamic to acoustic fields occurs within a thin layer that originates at the nozzle lip and is inclined at approximately  $9^\circ$  with respect to the jet centerline. A purely axial stencil near this transition layer poses the risk of extending from the acoustic to the hydrodynamic regions. Accordingly, the stencil angle, defined by  $\theta = \arctan(\eta/\xi)$ , follows the scheme depicted in Fig. 3.2. At points within the lip line  $r = 0.5D_j$ , the displacement is purely axial. Outside the lip line, the stencil aligns with the reference location  $(x, r)$  and the nozzle lip, up to a maximum angle of  $9^\circ$ . This transition at  $9^\circ$  is based on the angle of the radiator surface, which is located in Section 3.3.3. An example of space-time correlation given the reference point is plotted in Fig. 3.3. For a given axial separation  $\xi$ , the correlation peaks at a time shift  $\tau_{\max}$ . To minimize the error due to the discrete form of the correlation,  $\tau_{\max}$  is determined after fitting a seventh-order polynomial to the correlation curve for each displacement, as shown in the figure.

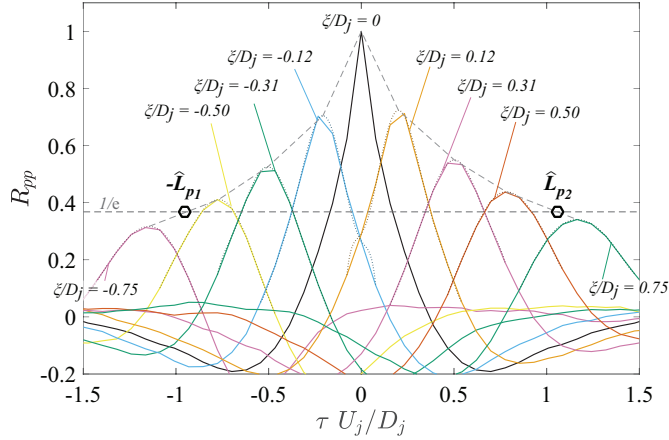


Figure 3.3: Space-time correlation  $R_{pp}$  in the vortical field at  $x/D_j = 2.5$  and  $r/D_j = 0.5$ . Dotted lines: fits by seventh-order polynomials. Dashed lines: envelope and ordinate relevant to the calculation of  $\hat{L}_p$ .

### 3.2.2 Convective Velocity

In the space-time correlations, each discrete axial separation  $\xi_i$  around a reference location  $(x, r)$  yields a correlation that peaks at time shift  $\tau_{\max, i}$ . The associated phase speed is  $U_{c_i} = \xi_i / \tau_{\max, i}$ . The axial convective velocity at that reference location is calculated as the average of  $U_{c_i}$  extracted from the correlations whose peak values exceed 0.4. The convective velocity can be based on velocity or pressure fluctuations, yielding  $U_{c_u}$  and  $U_{c_p}$ , respectively.

### 3.2.3 Fixed-Frame Length Scales

The fixed-frame length scale is the axial distance  $L$  over which events remain correlated at fixed time. Following Harper-Bourne [44], Morris and Zaman [71], and Dahl [35], the length scale is the displacement  $\xi$  at which the correlation  $R_{ff}$  decays to  $1/e$ . Noting that  $R_{ff}$  is not an even function of  $\xi$  [92], displacements  $\xi$  are taken in the negative and positive directions relative to the reference location. This procedure yields two displacements,  $\xi = -L_{f_1}$  and  $\xi = L_{f_2}$ , that satisfy  $R_{ff}(x, r; \xi, \eta(\xi), 0) = 1/e$ , with  $\eta$  and  $\xi$  linked according to procedure outlined in Section 3.2.1. The fixed-frame length scale is the average of of the two

displacements:

$$L_f = \frac{1}{2}(L_{f_1} + L_{f_2}) \quad (3.2)$$

In practice, the application of Eq. (3.2) requires interpolation between the discrete data of the simulation. The definition of length scale used here differs from the classical definition as the integral of the correlation curve [54]. However, the two approaches yield similar results as the integral approach often terminates at the first zero crossing of  $R_{ff}$ . Comparison of the two approaches shows that the quantitative values differ slightly but the qualitative trends are consistent.

### 3.2.4 Moving-Frame Length Scales

The moving-frame length scale  $\widehat{L}$  is a measure of the axial distance over which turbulence remains correlated as it convects downstream. It can also be interpreted as the “length of life” of a turbulent eddy, the distance traveled until its characteristics are lost through pairing or other mechanisms. Kerhervé *et al.* [54] note that this is not a “real” length scale, but rather a product of the convective velocity and a time scale of turbulence “life”. Nevertheless, it is an intrinsic characteristic of the stochastic events of the jet and can be useful for aeroacoustic models that use a Lagrangian frame of reference. The focus now is the envelope of the correlations represented by the dashed line of Fig. 3.3. Similarly to the fixed-frame length scales, displacements  $\xi = [-\widehat{L}_{f_1}, \widehat{L}_{f_2}]$  satisfy  $R_{ff}(x, r; \xi, \eta(\xi), \tau_{\max}(\xi)) = 1/e$ , as illustrated in the figure. The moving-frame length scale is then defined as

$$\widehat{L}_f = \frac{1}{2}(\widehat{L}_{f_1} + \widehat{L}_{f_2}) \quad (3.3)$$

The values of  $\xi$  corresponding to  $\widehat{L}_{f_1}$  and  $\widehat{L}_{f_2}$  are linearly interpolated from the correlation maxima.

### 3.2.5 Azimuthal Scale

The azimuthal scale is defined for zero axial, radial, and time separations. The related two-point correlation is

$$R_{ff}(x, r, \alpha) = \frac{\overline{f(x, r, \phi, t) f(x, r, \phi + \alpha, t)}}{\overline{f^2(x, r, \phi, t)}} \quad (3.4)$$

where  $\alpha$  is the the azimuthal separation. This formulation reflects the stationarity in azimuthal angle  $\phi$  expected for an axisymmetric jet. For a given reference point  $(x, r, \phi)$ , the azimuthal scale  $\Phi_f$  is defined by

$$R_{ff}(x, r; \alpha = \Phi_f) = 1/e \quad (3.5)$$

The range of the azimuthal scale is  $\Phi_f \in [0, \pi]$ , where  $\Phi_f = \pi$  indicates that  $R_{ff}$  is above the threshold of  $1/e$  for the entire azimuthal range. Note that in this work, the azimuthal variations of the flow field are reconstructed from the first nine Fourier modes of the complete three-dimensional LES solution.

## 3.3 Overview of the Flow Field

### 3.3.1 Mean Velocity

Isocontours of the normalized mean axial velocity,  $\bar{u}/U_j$ , averaged in the azimuthal direction, are plotted in Fig. 3.4(a). The axial distribution of the centerline mean velocity,  $\bar{u}_{\text{CL}}/U_j$  is plotted in Fig. 3.4(b) and shows good agreement with the experimental data of Lau *et al.*[56]. The end of the potential core, defined here as the point where the centerline mean axial velocity decays to  $\bar{u}_{\text{CL}} = 0.95U_j$ , is located near  $x = 7.4D_j$ .

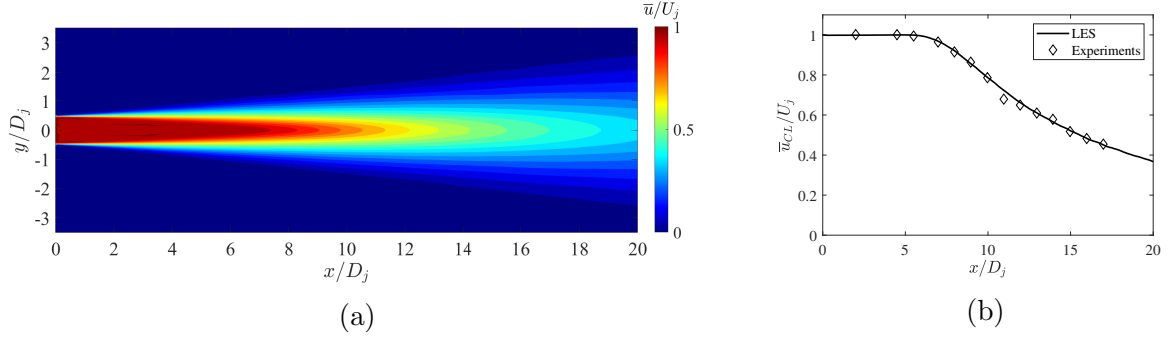


Figure 3.4: Distribution of normalized mean axial velocity. (a) Isocontours on a symmetry plane; (b) axial distribution on jet centerline compared to experiments by Lau *et al.* [56].

The momentum thickness of the jet is relevant to scaling relations that follow in Sections 3.4 and 3.5. To maintain the same definition within and downstream of the potential core, a generalization of the shear-layer momentum thickness is used:

$$\delta_\theta = \int_0^\infty \frac{\bar{\rho}(r)\bar{u}(r)}{\bar{\rho}_{CL}\bar{u}_{CL}} \left(1 - \frac{\bar{u}(r)}{\bar{u}_{CL}}\right) dr \quad (3.6)$$

where the centerline mean conditions are used for normalization. The growth of  $\delta_\theta(x)$ , plotted in Fig. 3.5, is well approximated by the linear fit  $\delta_\theta/D_j = 0.023 x/D_j + 0.007$ .

The radial location of the inner edge of the shear layer  $r_i(x)$  is also relevant to scaling relations that will be developed. Within the extent of the potential core, the inner edge is defined as the interior locus where the magnitude of the mean vorticity equals  $0.05U_j/D_j$ , that is,

$$|\bar{\omega}(x, r = r_i)| = 0.05 \frac{U_j}{D_j}, \quad r < D_j/2 \quad (3.7)$$

Past the potential core, where the annular shear layer has collapsed on itself, we set  $r_i = 0$ . The axial evolution of  $r_i$  is plotted in Fig. 3.5.

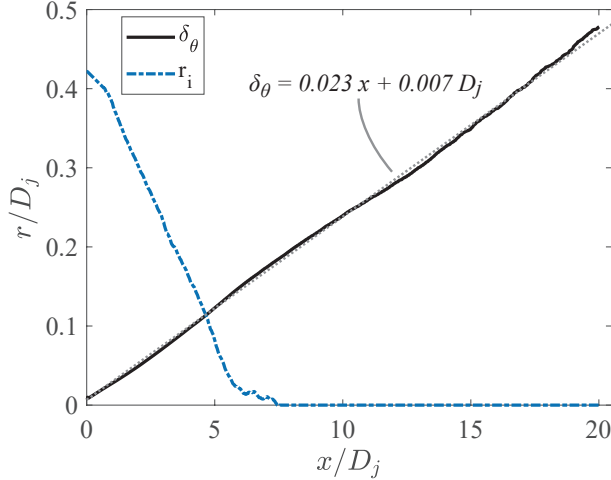


Figure 3.5: Axial distributions of momentum thickness  $\delta_\theta/D_j$  (solid black line) and inner edge of shear layer  $r_i/D_j$  (dashed blue line). Dotted line indicates linear fit.

### 3.3.2 Reynolds Stress

Section 2.4.3 introduced the idea of using the magnitude of the principal components of the Reynolds stress, normalized by the mean density, as time-averaged variable that is directly related to the turbulence dynamics of shear layers. Papamoschou [74] surmises that, in multi-stream jets, the outermost peak of  $g$  is a relevant surface for noise generation and modeling. For a single-stream round jet there is only one peak of  $g$  and the mean velocity gradient is in the radial direction. The surface is therefore named SPS (Surface of Peak Stress). It represents the locus of the most energetic eddies and can be readily detected in RANS simulations by modeling  $g$  as explained in Section 3.6.

Isocontours of the normalized Reynolds stress magnitude  $g/U_j^2$  are plotted in Fig. 3.6. The location of the SPS is included in the figure. The distribution of  $g/U_j^2$  creates two distinct lobes that reach a minimum separation around  $x/D_j = 9$ . Per its definition, the SPS is the locus of the radial maximum of the Reynolds stress. This places the surface very close to the nozzle lipline ( $r/D_j = 0.5$ ) until  $x/D_j = 11$ . Downstream of this station, the SPS expands at an angle of approximately  $4^\circ$  with respect to the jet axis. The maximum value of the Reynolds stress is  $g/U_j^2 = 0.0089$  and occurs near  $x/D_j = 5$ .

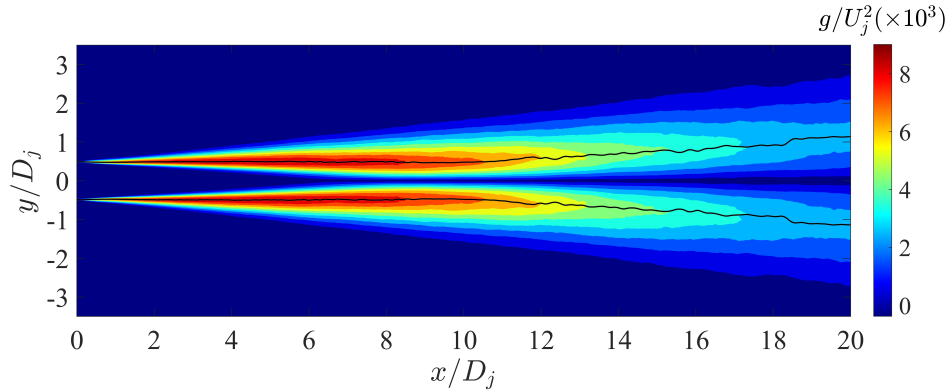


Figure 3.6: Isocontours of normalized Reynolds stress magnitude  $g/U_j^2$ . Black line: SPS.

### 3.3.3 Convective Velocity

The  $x - r$  distribution of the convective velocity  $U_{c_p}$  calculated from space-time correlations of the pressure fluctuation is plotted in Fig. 3.7. Two distinct regions are noted: an inner region, encompassing the jet flow, where  $U_{c_p}$  generally follows the trend of the mean axial velocity, and an outer region, near the edge of the jet and beyond, where  $U_{c_p}$  rapidly increases to supersonic values indicative of the acoustic field. Starting from the jet centerline,  $U_{c_p}$  initially follows the trend of the mean velocity, reaches a minimum, and then starts rising within the rotational region of the jet. This reversal has also been seen in earlier LES of single-stream jets [3, 83]. With further increase of the radius,  $U_{c_p}$  increases rapidly and attains large values in the acoustic field. The very large, supersonic values of  $U_{c_p}$  at large radius represent the trace along  $x$  of acoustic waves propagating at large angles with respect to the downstream direction.

The distribution of convective velocity based on axial velocity fluctuation is shown in Fig. 3.8. It shows a resemblance to the  $x - r$  distribution of  $U_{c_p}$  in terms of general trends: an inner region where  $U_{c_u}$  decreases radially and a reversal to rapid growth at the other regions of the vortical field and beyond. The main difference between velocity- and pressure-based convective velocities are that the radial minimum of  $U_{c_u}$  is located outwards from that of  $U_{c_p}$ , and the values of  $U_{c_u}$  are lower than those of  $U_{c_p}$  beyond that minimum. This

difference indicates that the transition from hydrodynamic to acoustic fields is experienced differently whether we are examining velocity or pressure fluctuations, an idea that will be explored more in detail in the later sections.

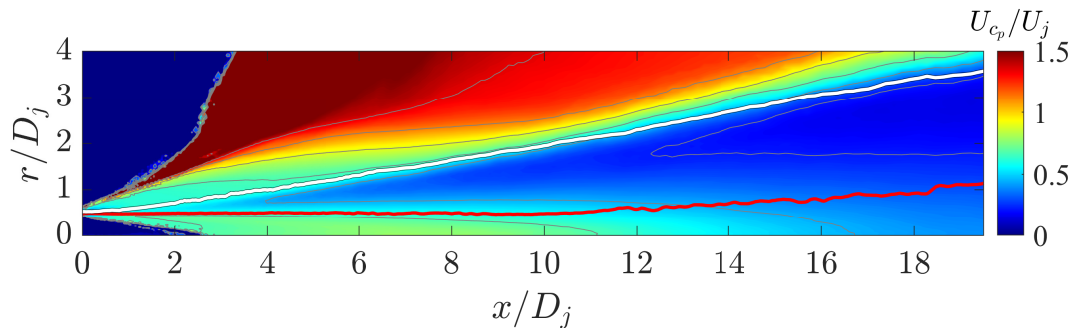


Figure 3.7: Isocontours of normalized convective velocity  $U_{c_p}/U_j$  on a meridional plane. Red line: SPS. White line: radiator surface.

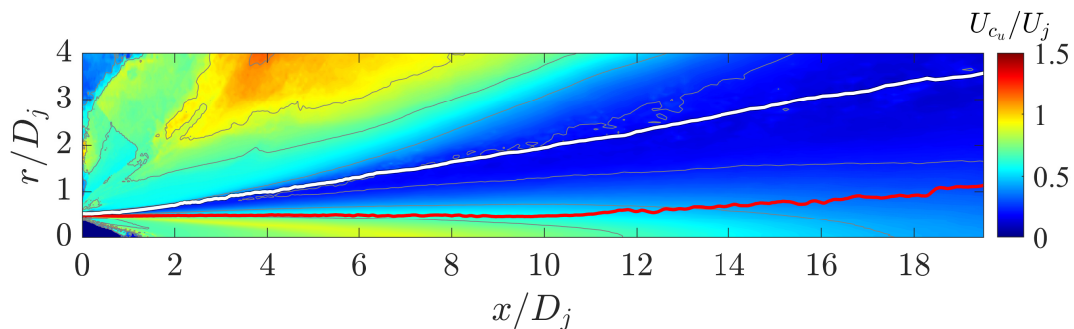


Figure 3.8: Isocontours of normalized convective velocity  $U_{c_u}/U_j$  on a meridional plane. Red line: SPS. White line: radiator surface.

### Location of the Radiator Surface

The convective velocity is an important variable for jet noise generation and modeling and may aid in the location of the radiator surface. As explained in Section 2.4.3, the radiator surface is the location where partial fields, informed by turbulence characteristics of the shear layer, will be prescribed. It is then sensible to look for a connection between the convective velocity distributions on the SPS and at the edge of the jet.

The first thing to determine is whether the LES-based convective velocity should be based on space-time correlations of the axial velocity fluctuation  $u'$  or the pressure fluctuation  $p'$ . Due to their physical associations,  $u'$ -based space-time correlations are designated for the inside of the vortical field, where the turbulent structures affect the velocity of the flow directly; and  $p'$ -based correlations for the region near and beyond the the edge of the jet, where they capture the pressure imprint of the vortical eddies.

In this work, we define the radiator surface as the region near the edge of the jet where the  $R_{pp}$ -based  $U_c$  distribution matches that  $R_{uu}$ -based  $U_c$  distribution on the SPS. We call this criterion “ $U_c$ -match”. The result is the white lines the white lines plotted in Figs. 3.7 and 3.8. The radiator surface is located at the transition region between hydrodynamic and acoustic fields as indicated by the  $R_{pp}$ -based map. Its growth is nearly linear at an angle of  $9^\circ$  relative to the jet centerline. The SPS is included in the plots for completeness.

With the new definition for the location surface and after visualizing the field of Renyolds stress in Subsection 3.3.2, we can collect the basic elements of the surface-based model envisioned in this work for the case of a single-stream jet in Fig. 3.9. The action of the turbulent eddies that dominate sound production is represented by the statistics on the SPS. The noise source is prescribed as a distribution of random partial fields on the surface at the edge of the jet. That surface is located at the boundary between the non-linear and linear flow fields, and is located by time-resolved data on the region near the edge where the convective velocity equals that of the SPS.

### Connection to the Mean Axial Velocity

The trends of Figs. 3.7 and 3.8 can be further quantified by plotting the radial distributions of  $U_{c_p}$ ,  $U_{c_u}$  and  $\bar{u}$  at  $x/D_j = 3, 5$  and  $8$  in Fig. 3.10. The potential core is manifested by the flat regions of the  $U_{c_p}$  and  $\bar{u}$  profiles near  $r = 0$ , which exist for  $x/D_j < 7.4$ . The

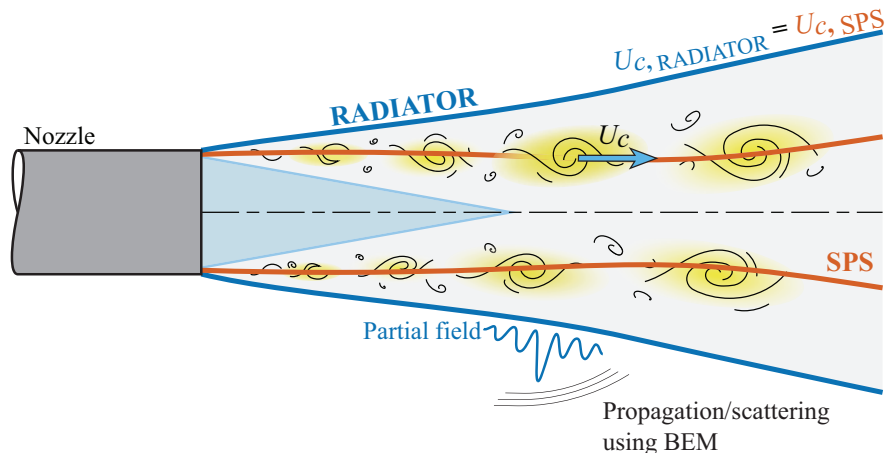


Figure 3.9: Representation of wavepacket model for the single-stream jet.

profiles of  $U_{c_u}$  show a local maximum near the edge of the potential core, which may be due to numerical artifacts or vortical features that make studying  $R_{uu}$  on this region difficult. The mean axial velocity is higher than the convective velocities in the inner regions of the jet. All profiles decrease radially within the shear layer and converge to similar values very near the SPS location. Beyond the SPS, the value of  $\bar{u}$  shows the strongest radial decrease, followed by  $U_{c_u}$ . As noted above, the profiles of convective velocity reach a radial minimum and rise beyond it, but  $U_{c_p}$  exhibits that minimum at a lower radius and attains larger values in the acoustic field. The very large, supersonic values of  $U_{c_p}$  at large radius represent the trace along  $x$  of acoustic waves propagating at large angles with respect to the downstream direction.

It is instructive to compare the axial distribution of  $U_{c_p}$  and the mean axial velocity  $\bar{u}$  on the SPS. As seen in Fig. 3.11, the two distributions are very close, with  $\bar{u}$  being about 8% lower for  $x/D_j < 10$ . This indicates that the convective velocity can be approximated well by the axial mean velocity on the SPS [74]. Within the potential core, the convective velocity is near  $U_{c_p} = 0.6U_j$ . For completeness, the figure includes the convective velocity  $U_{c_u}$ , which is based on space-time correlations of  $u'$ . The distributions of  $U_{c_u}$  and  $U_{c_p}$  are practically identical. The three curves of Fig. 3.11 show that, in the region of the most energetic eddies

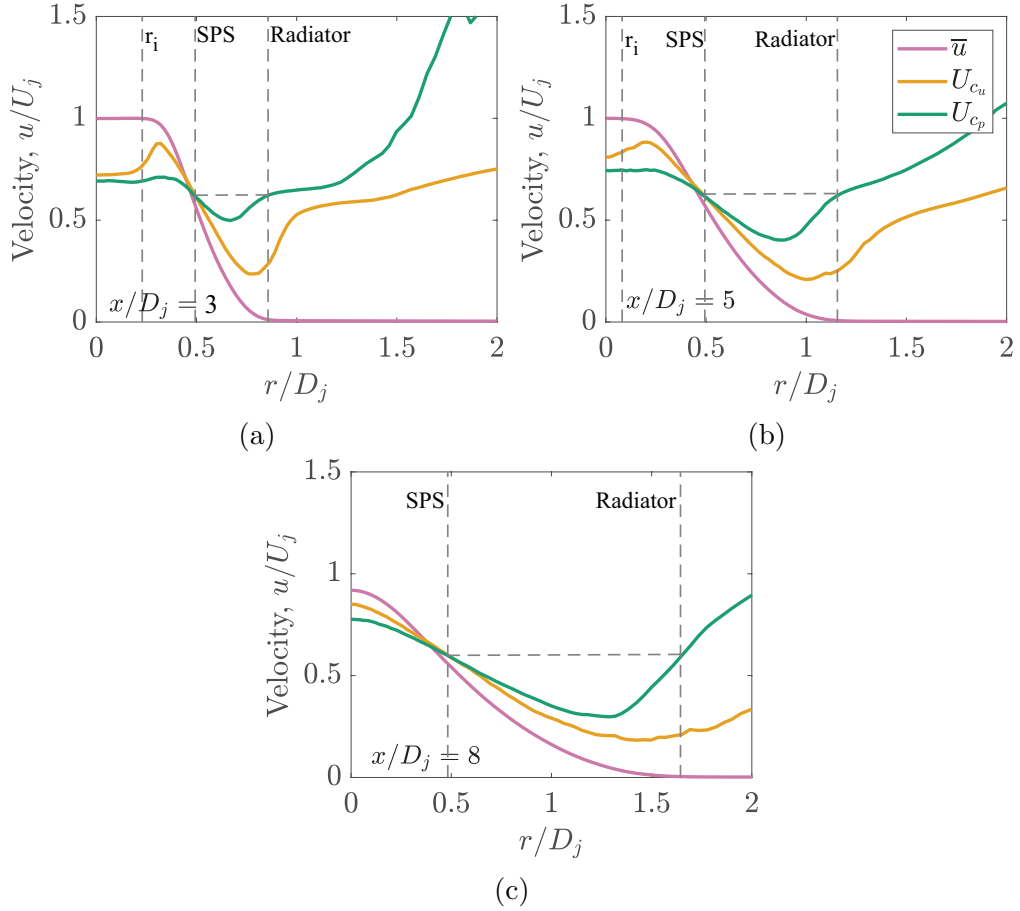


Figure 3.10: Radial distributions of  $\bar{u}$ ,  $U_{cu}$ , and  $U_{cp}$  at (a)  $x/D_j=3$ , (b)  $x/D_j=5$ , and (c)  $x/D_j=8$ . Legend is the same for all plots.

represented by the SPS, the axial transport of velocity and pressure fluctuations involves the same mechanism of convection by the local mean velocity. This is not true in other regions of the jet where significant differences can be found between  $U_{cu}$  and  $U_{cp}$ .

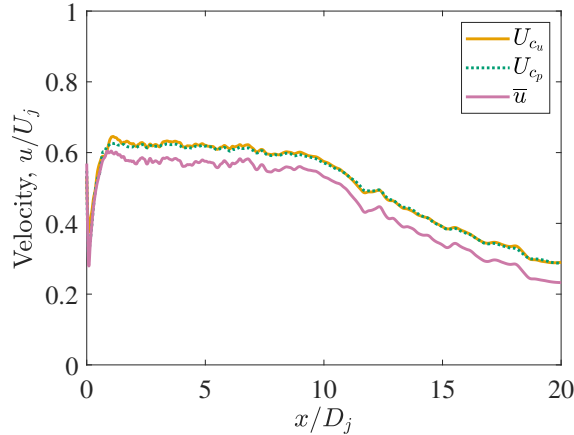


Figure 3.11: Axial distributions of  $U_{c_p}$ ,  $U_{c_u}$ , and  $\bar{u}$  on the SPS.

### 3.3.4 Instantaneous Vorticity

The main characteristic of the radiator surface is that it is placed at the boundary between the rotational and irrotational fields. It is therefore relevant to study the vorticity distribution as a means of delineating those fields and testing the validity of the  $U_c$ -match criterion for defining the radiator surface. Figure 3.12 plots a snapshot of the normalized vorticity norm  $|\omega|D_j/U_j$  on the  $x - y$  plane of the jet. The magnitude of  $|\omega|D_j/U_j$  has a wide dynamic range, approximately  $[0, 30]$  throughout the jet, and its exact range will depend on the local grid and sub-grid scale modeling. The contour is limited to  $|\omega|D_j/U_j = 7.5$  to accentuate the moderate fluctuations near the edge of the jet. Additionally, Fig. 3.13 plots the vortex identification method of swirling strength  $\lambda_{ci}$  [117] at the same snapshot for a better visualization of vortical events in the flow. Both figures include the radiator surface and the SPS.

Figures 3.12 and 3.13 indicate that the radiator surface, using the  $U_c$ -match criterion, encloses the vortical events inside the jet, with very scarce events crossing the surface. This feature is seen consistently for all time realizations of this jet. This observation gives credence to the notion that the  $U_c$ -match criterion results in a proper placement of the radiator surface.

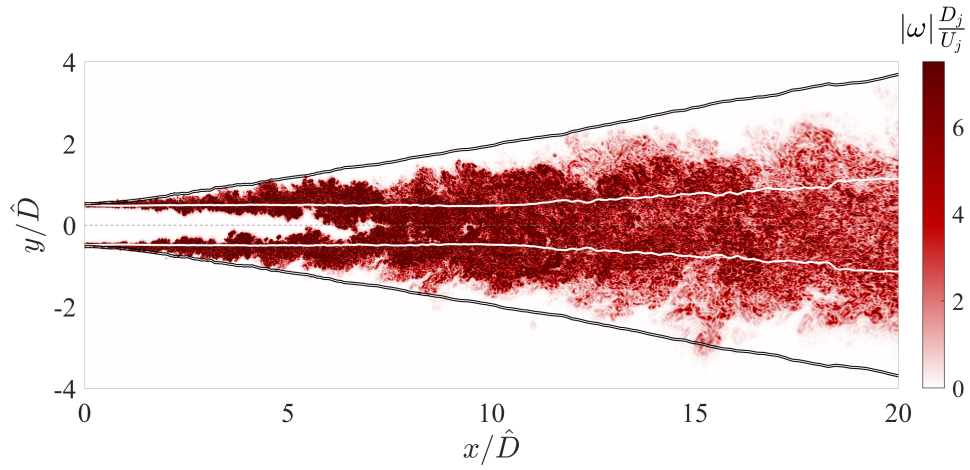


Figure 3.12: Contour of instantaneous vorticity norm along a longitudinal plane. Black double line: radiator surface. White line: SPS.

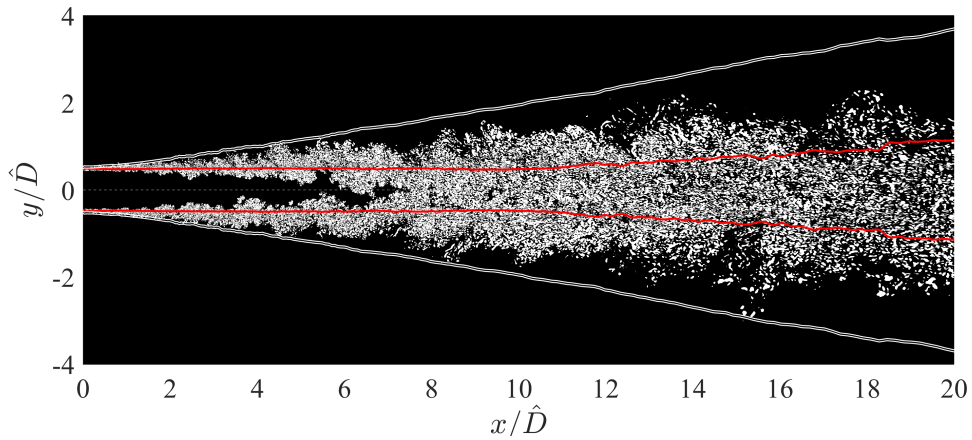


Figure 3.13: Representation of swirling strength at the value  $\lambda_{ci} = U_j/D_j$ . White double line: radiator surface. Red line: SPS.

## 3.4 Longitudinal Correlations

### 3.4.1 Two-Dimensional Correlations

Correlations on a meridional plane can give insight on the structure of turbulence and resulting acoustic field [10]. They also help in understanding the length scale distributions presented in the following Subsections 3.4.2 and 3.4.3. Space-time correlations  $R_{uu}$  and  $R_{pp}$  on a meridional plane are plotted in Fig. 3.14 for three time separations. The reference point is on the SPS at  $x/D_j = 3.0$ . The normalized time separations are  $\tau U_j/D_j = -1.94$  (top row), 0 (middle row) and 1.94 (bottom row). A vertical dashed line indicates the position that corresponds to a downstream convective velocity  $U_c = 0.6U_j$ .  $R_{uu}$  shows a compact area of correlation, mostly limited to a small positive (red) region that travels along the SPS and a negative (blue) oblong region along the radiator surface. On the other hand,  $R_{pp}$  has a wide structure of radially-oriented lobes extending from the centerline well into the acoustic field; the main structure comprises a positive lobe (red) flanked by strong negative lobes (blue), resembling a hydrodynamic pressure wave. The structures of  $R_{uu}$  and  $R_{pp}$  travel at similar convective velocities, but the former is slightly slower and the latter slightly faster than  $0.6U_j$ .

We now examine the evolution of  $R_{uu}$  and  $R_{pp}$  with the reference point on the SPS at  $x = 7.5D_j$ , near the end of the potential core. Figure 3.15 displays the resulting correlations at time separations  $\tau U_j/D_j = -3.49$  (top row), 0 (middle row) and 3.49 (bottom row). The time progression of  $R_{uu}$  shows a compact structure of positive correlation traveling along the SPS. The effects of that structure are felt above the radiator surface as a region of negative correlation. At  $\tau = 0$ , the peak of the negative correlation is -0.24. The limited size of the positive structure indicates that the  $u'$  correlations capture the local but not global effects of the convecting eddies. The axial velocity fluctuation thus becomes decorrelated as we

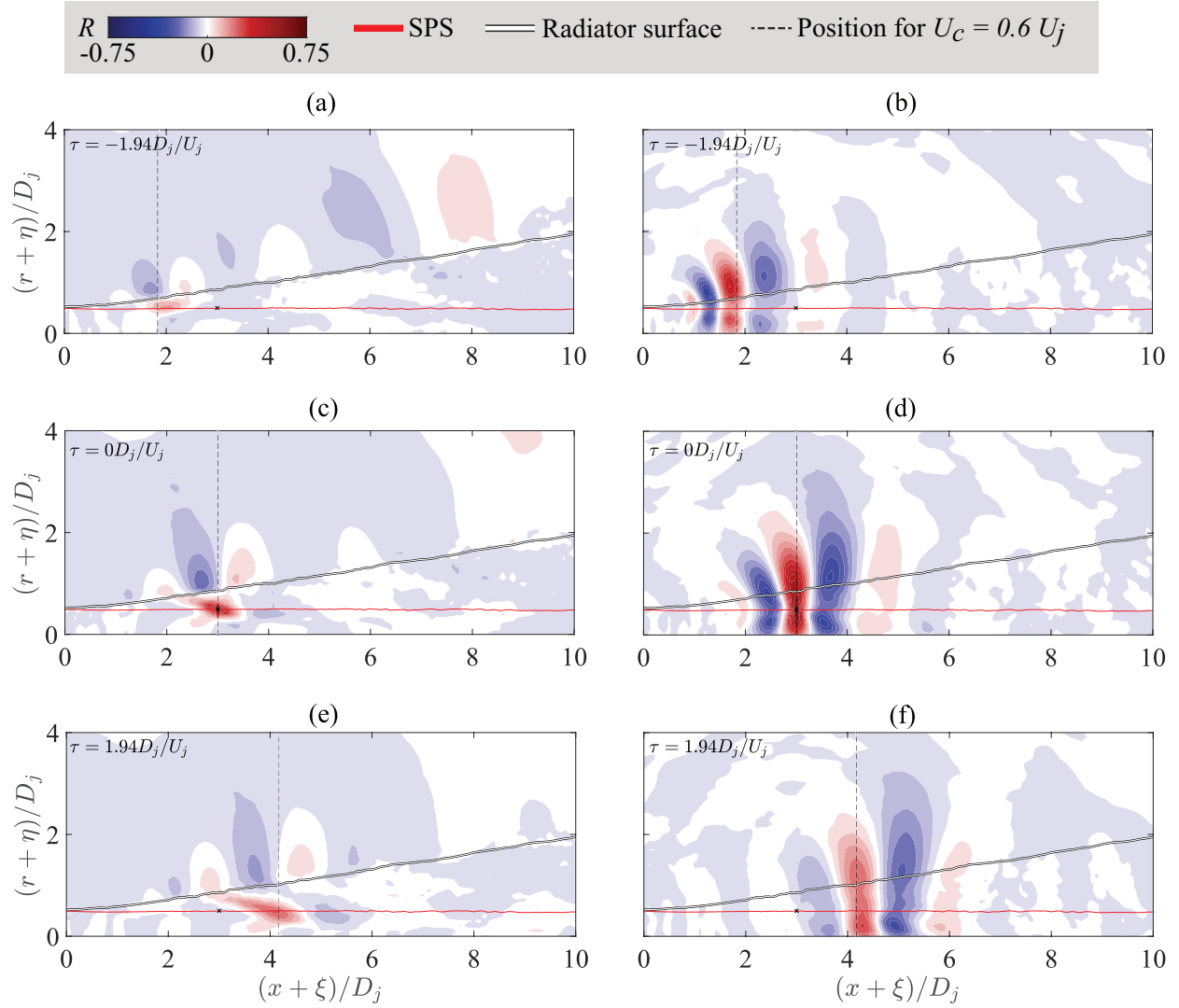


Figure 3.14: Contours of  $R_{uu}$  (left column) and  $R_{pp}$  (right column) with reference point on SPS at  $(x, r) = (3, 0.5)D_j$  for three time separations.

move from the SPS to the outer edge of the jet. This explains the region of low correlation between positive and negative structures in Fig. 3.15(a,c,d).

The time progression of  $R_{pp}$  is seen in Fig. 3.15(b,d,f). A wavepacket-like structure is evident for all the time separations. At zero time separation, in Fig. 3.15(d), a region of strong positive correlation emanates as a radial beam from the reference point to all across the jet, from the centerline to well outside the radiator surface. It is evident how the footprint of the large-scale structures is imprinted on the radiator surface. For negative and positive time separations, in Fig. 3.15(b,f), similar but weaker structures are seen, with a rapid decorrelation for  $\tau > 0$ . The latter may be explained by the breakdown of the shear-layer structures after the end of the potential core [111]. It is notable that the  $R_{pp}$  correlations structures convect fairly uniformly with a speed near  $0.6U_j$ , while the  $R_{uu}$  structures are stretched and their convective speed depends on radial location.

The differences in location, shape, and convective velocity of the features of  $R_{uu}$  and  $R_{pp}$  in Figs. 3.14 and 3.15 suggest that the two correlations portray events of different nature. The  $u'$ -based correlations reflect compact, localized turbulence events that travel along the SPS. The  $p'$ -based correlations appear to reflect interactions of eddies with the potential flow around them, namely the ambient air and the potential core, which result in large regions of influence. Consequently, pressure-based scales may not capture local events as accurately as velocity-based scales.

### 3.4.2 Fixed-Frame Length Scales

The distributions of fixed-frame length scales defined in Subsection 3.2 are now presented. Isocontours of normalized length scales based on axial velocity fluctuation,  $L_u/D_j$ , and on pressure fluctuation,  $L_p/D_j$ , are plotted in Fig. 3.16. The radiator surface marks the end of the vortical region, inside of which the scales  $L$  generally follow the axial growth of the

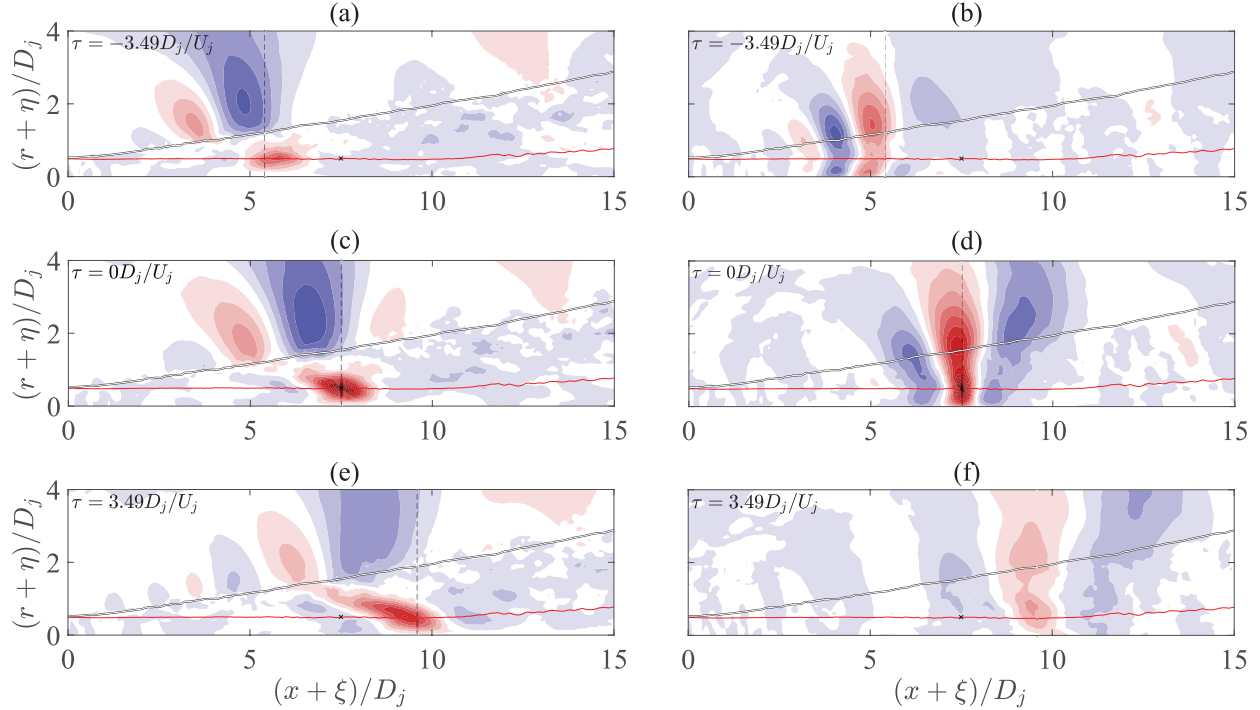


Figure 3.15: Contours of  $R_{uu}$  (left column) and  $R_{pp}$  (right column) with reference point on SPS at  $(x, r) = (7.5, 0.5)D_j$  for three time separations. Legend is the same as for Fig. 3.14.

momentum thickness. At a given axial location and going outwards from the inner edge of the shear layer  $r_i$ ,  $L_u$  increases, reaches a local maximum within the jet, then decreases to a local minimum at the edge of the jet. Outside the jet,  $L_u$  rises to high values. The local radial minimum of  $L_u$  follows closely the radiator surface. This suggests a loss of coherence of velocity-based events near the edge of the jet. Near the SPS,  $L_u$  experiences the strongest radial variation within the jet flow. In Fig. 3.16(b)  $L_p$  does not have a local maximum inside the jet in the radial direction. Instead, it is strictly increasing until reaching a maximum around one nozzle diameter outwards from the radiator surface. Its maximum radial gradient is found near the radiator surface.

The radial trends of Fig. 3.16 are interpreted as follows. The inner vortical region of the jet, marked by the SPS, contains the main events of mixing and momentum transport of the mixing layer, see Eq. 2.12. That region encompasses the largest scales of turbulence and, through energy cascade, it contains small scales as well[90]. The combination of large and

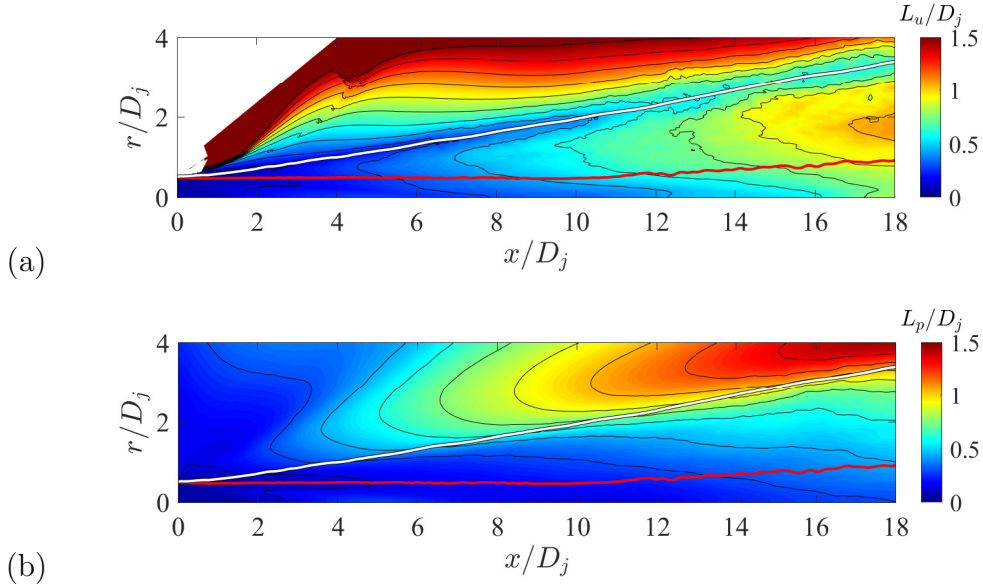


Figure 3.16: Isocontours of normalized length scales (a)  $L_u/D_j$  and (b)  $L_p/D_j$ . Red line: SPS. White line: radiator surface.

small scales drives the value of the length scale  $L$  below the actual length of the large scales [71]. As one leaves the SPS towards higher radial locations with lower vorticity, the effects of small eddies are lost faster than those of large eddies, resulting in the increase of scales versus radius seen in Fig. 3.16. It appears that the pressure-based scales grow radially due to this effect until peaking beyond the radiator surface, into the linear field. Thus, that region of radial maxima is due to the footprint of the large-scale vortical structures inside the jet [32, 86]. The velocity-based scales have a different behavior, whereby they capture the extent of the eddies themselves but not their footprint away from them. This behaviour is sketched in Fig. 3.17. As one approaches the outer edge of the jet, the velocity fluctuations disassociate from the core vortical region and become influenced by a combination of acoustic effects and small eddies of secondary acoustic relevance. This complex combination of influences causes the “valley” of low length scale  $L_u$  at the edge of the jet seen in Fig. 3.16(a). This observation is supported by the recent work of Camussi and Bogey [28] on this same jet, which found that the region of the vortical field near the edge of the jet shows high values of intermittency,

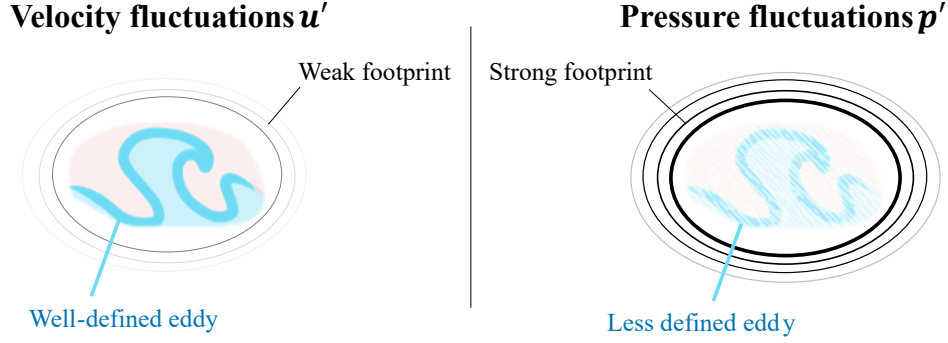


Figure 3.17: Simplified sketch of an eddy representation through velocity and pressure fluctuations.

and thus incoherent behavior. Further away from the jet edge, the acoustic perturbations start to dominate and cause the increase in length scale in the near-acoustic region.

To further quantify the connection between events on the SPS and radiator surface, the axial distributions of length scales  $L_u$  and  $L_p$  on these surfaces are plotted in Fig. 3.18. All the curves exhibit a substantially linear growth along the first 15 jet diameters. In addition, the length scales on the SPS acquire a higher value when calculated from velocity fluctuation than from pressure fluctuation. This result challenges the intuitive prediction that velocity scales would be lower due to a richer content of high frequencies, and therefore smaller scales [86]. However, this difference is likely to result from the specific definition of length scale used, based on Eq. (3.3), where only positive values of the correlation function are considered. Indeed, the correlations in Figs. 3.14 and 3.15 at  $\tau = 0$  show strong negative lobes of  $R_{pp}$  upstream and downstream from the reference point. Therefore, if the span of non-zero correlations were to be considered when defining the axial span of turbulence events, the pressure-based length scale would be longer than the velocity-based scale. Comparing scales based on the same variable, it is evident that those on the radiator surface are consistently larger than those on the SPS, with the pressure-based scale exhibiting the strongest increase in this regard. These results suggest that the signature of the eddies on the radiator surface is more coherent than the effect of the eddies in the vortical field. They are in line with the findings of Arndt *et al.* [4] that the pressure signal measured at the outer edge of a jet

mixing layer is dominated by the large-scale structure of the turbulent flow and is correlated over longer distances than the underlying velocity fluctuations.

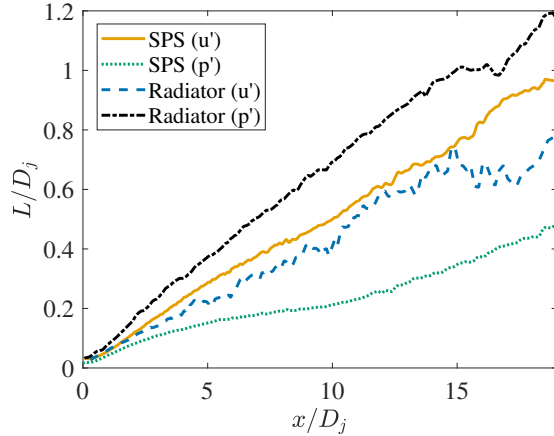


Figure 3.18: Axial distribution of the correlation scales  $L$  on the relevant surfaces. Orange solid line:  $L_u$  on SPS. Blue dashed line:  $L_u$  on the radiator surface. Green dotted line:  $L_p$  on SPS. Black line dash-dot:  $L_p$  on the radiator surface.

To examine the radial evolution of the correlation scales, we plot them in the “similarity” form  $L/\delta_\theta(x)$  versus  $(r - r_i(x))/\delta_\theta(x)$ . This form represents the expectation that the correlation scale grows with the momentum thickness  $\delta_\theta$ . The radial variations of the correlation scales at eight axial stations, from  $x/D_j = 1$  to 15, are shown in Fig. 3.19(a) for  $L_u$  and Fig. 3.19(b) for  $L_p$ . The locations of the centerline, SPS, and radiator surface are marked. The similarity form leads to a fair collapse of the curves, particularly for axial locations  $x/D_j \geq 3$  for  $L_u$  and  $x/D_j \geq 5$  for  $L_p$ . The length scales at  $x/D_j = 1$  and  $x/D_j = 3$  acquire high values near the centerline, possibly indicating the influence of coherent waves within the potential core. Overall, at all axial stations, common trends are found between the SPS (marked in black squares) and the radiator surface (blue circles) even though the trends differ between  $L_u$  and  $L_p$ . At high radii of  $(r - r_i)/\delta_\theta \geq 12$ , the curves diverge as a result of the acoustic propagation in a variety of directions depending on the axial position considered. The results in Fig. 3.19 are in agreement with the those by Fleury *et al.* [40] and Proença *et al.* [92], in which fixed-frame,  $u'$ -based correlation scales along the centerline and lipline grow according to the shear-layer width. This consistent scale growth is generalized here for

axial and radial locations within the jet (excluding the potential core region) and for both velocity- and pressure-based scales.

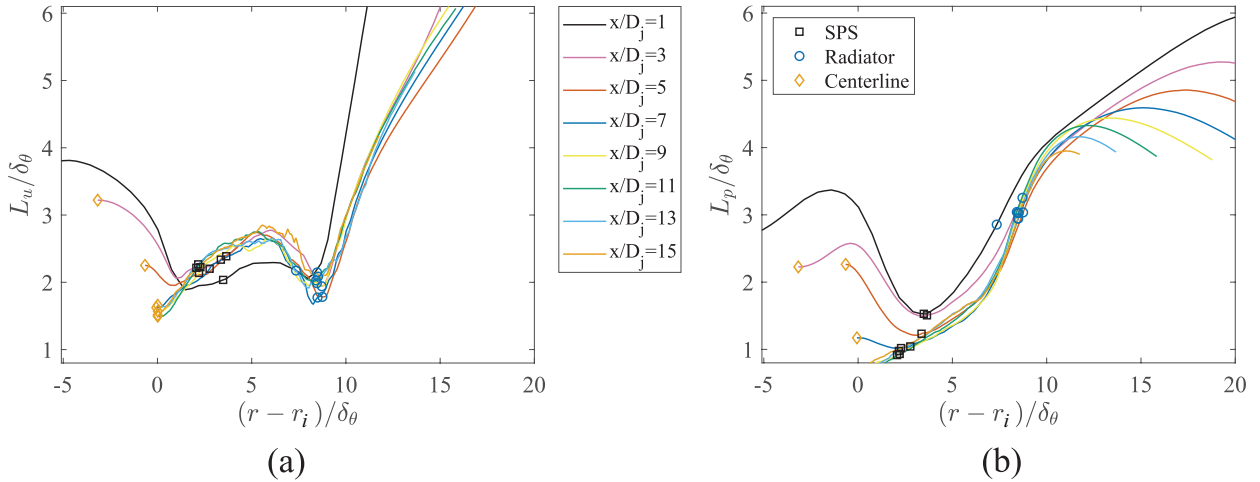


Figure 3.19: Plots of normalized length scales  $L/\delta_\theta$  versus normalized radius  $(r - r_i)/\delta_\theta$ , (a) based on axial velocity, (b) based on pressure. Legend applies to both subfigures.

### 3.4.3 Moving-Frame Length Scales

The distributions of the normalized moving-frame length scales based on axial velocity fluctuation  $\widehat{L}_u/D_j$  and pressure fluctuation  $\widehat{L}_p/D_j$  are presented in Fig. 3.20. The trends are somewhat similar to those seen for the fixed-frame scales in Fig. 3.16. With regards to the velocity-based scales, a notable difference is that the radial maxima of  $\widehat{L}_u$  inside the vortical field in Fig. 3.20(a) are more localized and occur inward, closer to the SPS, relative to those of  $L_u$  in Fig. 3.16 (a). This difference can be explained by examining the convection of the structures in Figs. 3.14 and 3.15, where the positive structure of  $R_{uu}$  rotates counter-clockwise as a result of the convective velocity decreasing with radius within the vortical region. High convective velocity near the jet axis elongates the lifespan of the turbulence, which is reflected by the radial maxima of  $\widehat{L}_u$  near the SPS. As with the fixed-frame scale distribution of Fig. 3.16 (a),  $\widehat{L}_u$  reaches minimum value near the location of the radiator surface. The pressure-based scale  $\widehat{L}_p$  follows the same general trends as  $\widehat{L}_u$  but with lower

values within the vortical region and a weak maximum slightly outside the SPS. Immediately outside the radiator surface,  $\widehat{L}_p$  rises rapidly to high values.

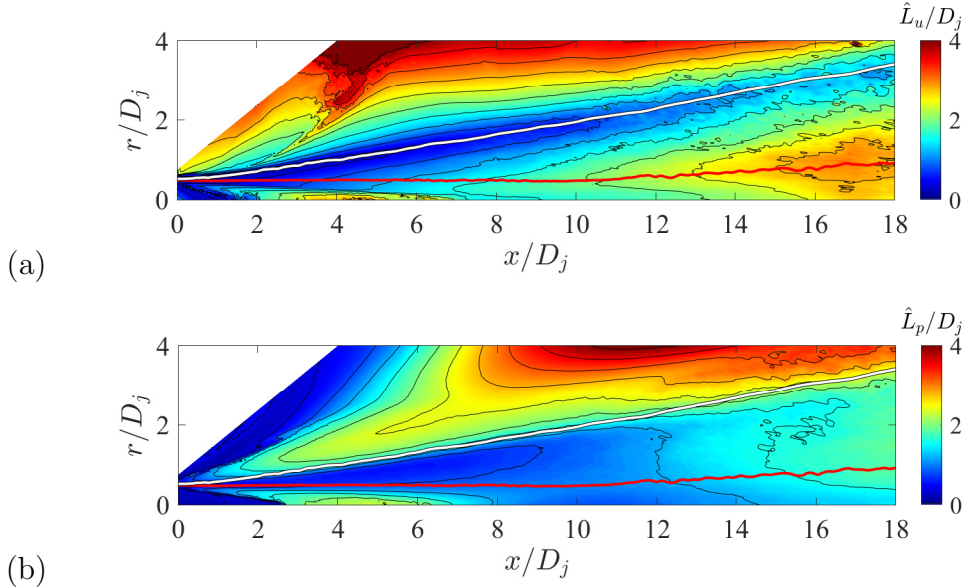


Figure 3.20: Isocontours of normalized length scales (a)  $\widehat{L}_u/D_j$  and (b)  $\widehat{L}_p/D_j$ . Red line: SPS. White line: radiator surface.

The axial distributions of the moving-frame length scales on the SPS and radiator surface are plotted in Fig. 3.21. Contrary to the fixed-frame length scales, where all curves exhibit a linear growth, here only those based on axial velocity fluctuation increase linearly on the SPS. The pressure-based length scale  $\widehat{L}_p$  rises rapidly within the first few jet diameters, reaches an apparent plateau, then resumes growth at a lower rate. On the radiator surface, it increases linearly at a fast rate up to  $x/D_j \approx 2.5$ , reaches a plateau for  $2.5 \leq x/D_j \leq 7.5$ , then grows at a rate similar to that of  $\widehat{L}_u$ . The difference in the trends of  $\widehat{L}_u$  and  $\widehat{L}_p$  is in line with the observations made in Section 3.4.1, where it is discussed that  $\widehat{L}_u$  follows the growth of the vortical region, while  $\widehat{L}_p$  appears affected by large-scale events that result from interactions of eddies with the potential flow surrounding them. Thus,  $\widehat{L}_p$  grows faster in the initial few diameters of the jet. This behavior might be explained by the dominance of different mechanisms of turbulence growth. Results by Schmidt *et al.* [96] and Pickering *et al.* [87] suggest that the shear layer over the potential core is dominated by Kelvin–Helmholtz type

instabilities, while the downstream regions have a stronger presence of Orr amplification mechanisms. However, the applicability of their results to this particular jet and two-point correlations has not been thoroughly studied and may be the target of future efforts.

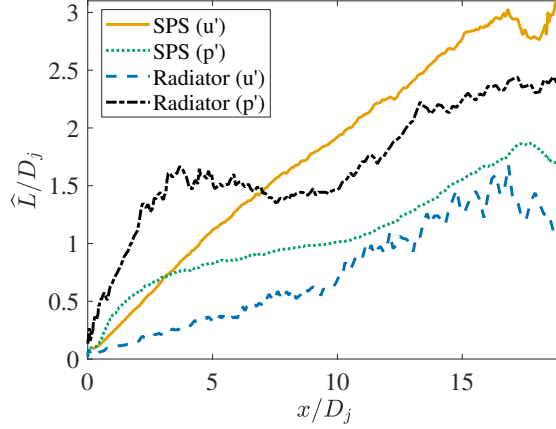


Figure 3.21: Axial distribution of length scales  $\widehat{L}$  on the relevant surfaces. Orange solid line:  $\widehat{L}_u$  on SPS. Blue dashed line:  $L_u$  on the radiator surface. Green dotted line:  $\widehat{L}_p$  on the SPS. Black line dash-dot:  $\widehat{L}_p$  on the radiator surface.

The radial variations of  $\widehat{L}_u$  and  $\widehat{L}_p$  are plotted in Fig. 3.22 using a normalization based on  $\delta_\theta$  as in Fig. 3.19. The curves at locations past the end of the potential core tend to collapse well. The curves at early axial locations also are very close to each other in the case of  $\widehat{L}_u$  in Fig. 3.22(a), which shows an approximately self-similar behaviour in agreement with the results by Proença *et al.* [92]. In contrast to  $\widehat{L}_u$ , the scales  $\widehat{L}_p$  in Fig. 3.22(b) grow rapidly near the nozzle exit and do not exhibit self-similar behavior.

## 3.5 Azimuthal Correlations

### 3.5.1 Modal Components

The azimuthal composition of the flow is studied by examining the radial variations of the energy of its Fourier modes  $m$ . The energy of the first five Fourier modes that compose

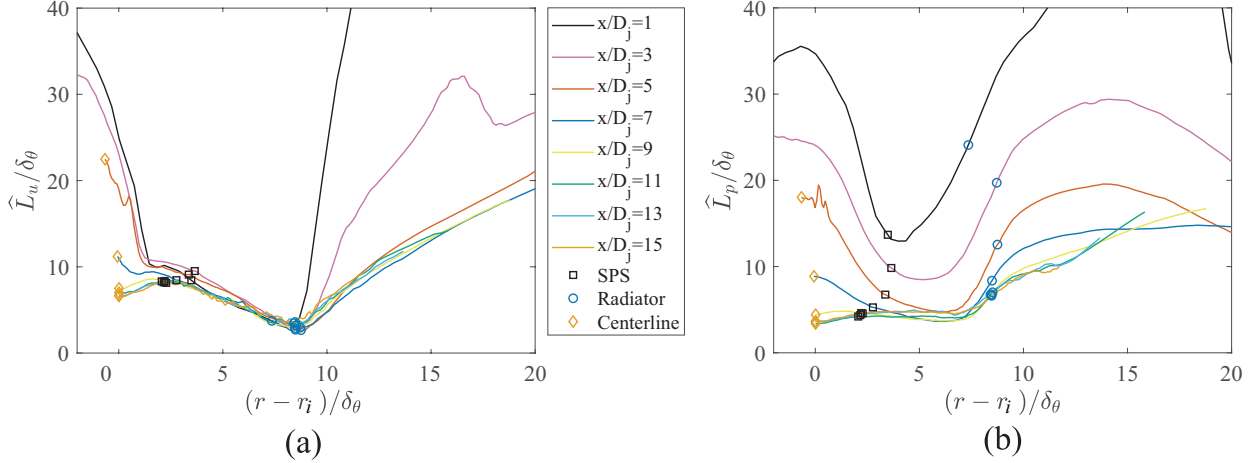


Figure 3.22: Plots of normalized moving-frame length scales  $\widehat{L}/\delta_\theta$  versus similarity coordinate  $(r - r_i)/\delta_\theta$ , (a) based on axial velocity; (b) based on pressure. Legend applies to both subfigures.

the  $u'$  and  $p'$  fluctuations is shown in Fig. 3.23. These distributions do not significantly depend on their axial location, so the results are only shown for  $x/D_j = 7.5$ . The modal energy distribution based on velocity fluctuation in Fig. 3.23a shows that the vortical region is dominated by modes  $m = 2, 3, 4$ , whose contributions peak near the location of the SPS. Lower modes such as  $m = 0, 1$  contain lower energy inside the vortical region but dominate the linear field past the radiator surface. On the other hand, the modal energies based on pressure fluctuation in Fig. 3.23b have fairly constant levels between the SPS and the radiator surface, with mode  $m = 1$  accounting for 33% of the total modal power. Going from the vortical to the linear field, the contributions of modes 0 and 1 rise and peak at distances  $1.0D_j$  and  $0.3D_j$  from the radiator surface, respectively. In that region, the two modes represent about 80% of the total power. Continuing outwards, the energy of those modes decreases and all modes reach levels between 8% and 28%. This radial variation is consistent with the radiation pattern observed in turbulent jets, where low modes dominate at shallow angles from the jet axis, and all modes have similar energy levels radiating perpendicularly to the jet axis [30].

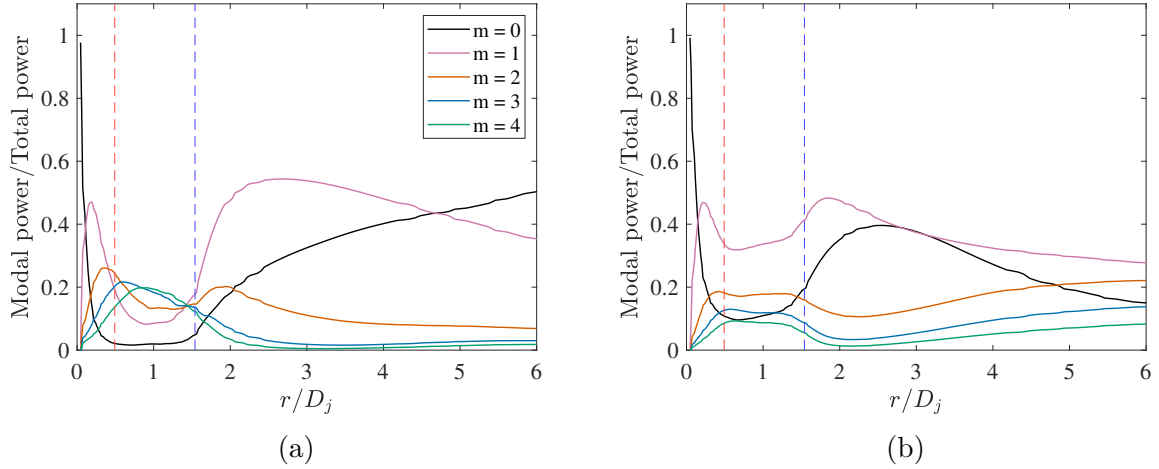


Figure 3.23: Radial distribution of modal powers on  $x = 7.5D_j$  for the first five modes; (a) based on axial velocity, (b) based on pressure. The vertical lines mark the locations of the SPS (red) and the radiator surface (blue).

### 3.5.2 Cross-Sectional Correlations

Two-dimensional correlations performed on a cross section of the jet at  $x/D_j = 7.5$  are represented in Fig. 3.24. The reference point is located on the SPS and marked by a white cross. The displacement in the  $z$  and  $y$  directions are denoted  $\zeta$  and  $\psi$ , respectively. Similarly to the longitudinal correlations presented in Subsection 3.4.1, there are notable differences between the distributions of  $R_{uu}$  and  $R_{pp}$ . The velocity correlations in Fig. 3.24(a) show a discrete, oblong shape of limited radial and azimuthal extent, flanked by negative sidelobes. The pressure correlations in Fig. 3.24(b) exhibit a wider azimuthal extent that remains roughly constant within the vortical field and increases rapidly in the linear field.

### 3.5.3 Azimuthal Scales

Isocontours of azimuthal scales based on axial velocity and pressure fluctuations are plotted in Fig. 3.25. By definition, there is full azimuthal coherence in the vicinity of the centerline as  $r \rightarrow 0$ . For both distributions, the azimuthal scale reaches a minimum of around  $15^\circ$  for

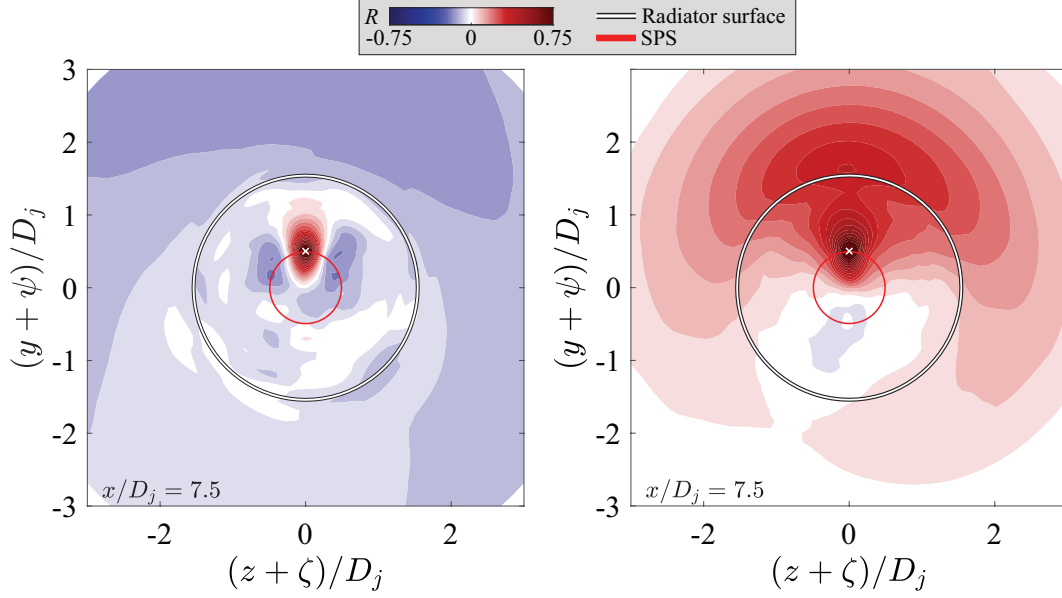


Figure 3.24: Contours of (a)  $R_{uu}$  and (b)  $R_{pp}$  on the cross-sectional plane  $x = 7.5D_j$  with reference point on SPS at  $\phi = \pi/2$  (white cross). Time shift is zero.

$\Phi_u$  and  $25^\circ$  for  $\Phi_p$  inside the vortical layer. With increasing radius, the azimuthal scale rises and becomes large in the acoustic near field. This rise starts earlier for  $\Phi_p$ . The distributions in Fig. 3.25 reflect a similar behavior to the fixed-frame length scales  $L_u$  and  $L_p$ , plotted in Fig. 3.16, divided by the radius  $r$ .

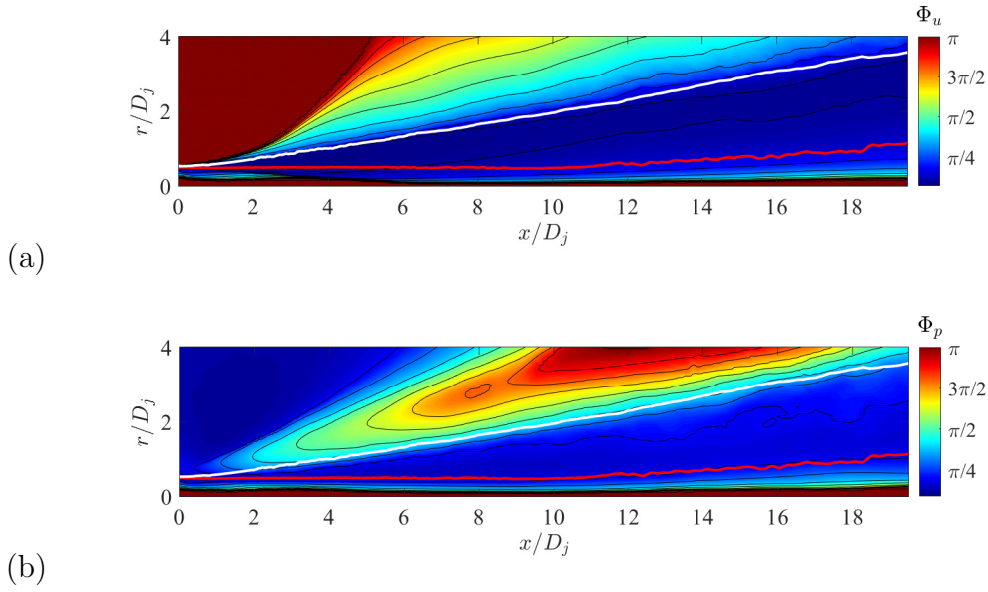


Figure 3.25: Isocontours of azimuthal scales (a)  $\Phi_u$  and (b)  $\Phi_p$ , units are radians. Red line: SPS. White line: radiator surface.

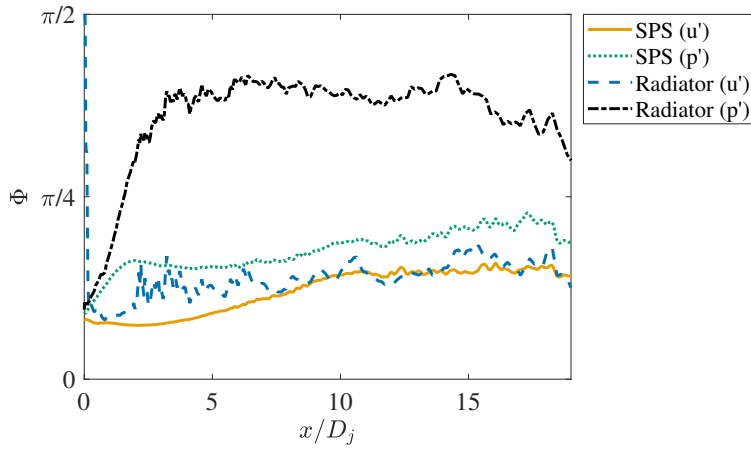


Figure 3.26: Axial distribution of azimuthal scales  $\Phi$  on the relevant surfaces. Orange solid line:  $\Phi_u$  on SPS. Blue dashed line:  $\Phi_u$  on the radiator surface. Green dotted line:  $\Phi_p$  on the SPS. Black line dash-dot:  $\Phi_p$  on the radiator surface.

The axial distributions of  $\Phi_u$  and  $\Phi_p$  on the SPS and radiator surface are plotted in Fig. 3.26. All curves display an initial growth followed by saturation. The saturation is consistent with the circumferential length scale and the radius of the surface both growing linearly. The pressure-based azimuthal scales  $\Phi_p$  display a faster initial growth than the

velocity-based scales  $\Phi_u$ . On the radiator surface,  $\Phi_p$  show the strongest correlation, which is consistent with the cross-sectional results in Fig. 3.24(b). They grow rapidly within the first three jet diameters, then saturate at approximately  $\pi/3$ . Radial profiles of  $\Phi_u$  and  $\Phi_p$  are plotted in Fig. 3.27 as a function of  $(r - r_i)/\delta_\theta$  and for several axial stations. Except for the region very near the nozzle exit ( $x/D_j \leq 1$ ) the profiles for each scale collapse fairly well within the radiator surface.

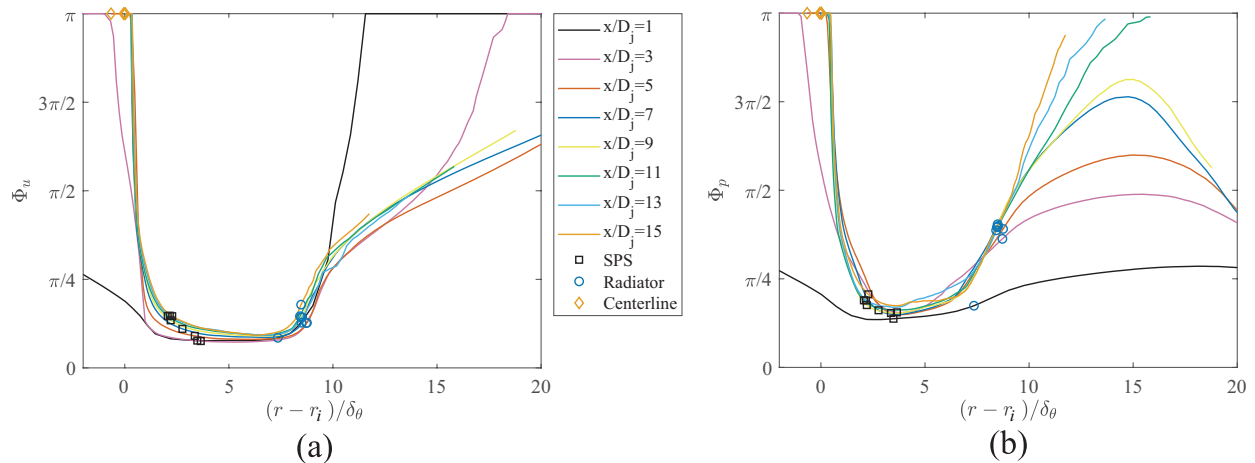


Figure 3.27: Azimuthal scales  $\Phi$  versus similarity coordinate  $(r - r_i)/\delta_\theta$ , (a) based on axial velocity; (b) based on pressure. Legend applies to both subfigures.

## 3.6 Modeling Based on the Time-Averaged Flow

The previous sections used the LES flow field to gain insight into the correlations between the vortical and the near-acoustic fields. The radiator surface is defined to contain the imprint of turbulent eddies that is crucial for modeling the jet noise source. However, the LES is costly and cannot yet be considered as a design tool. Can the properties on the radiator surface be informed by the time-averaged solution? This question is addressed here at a preliminary level.

### 3.6.1 RANS-Based Statistics

RANS-based statistics are relevant to the low-cost modeling of the noise source proposed in Ref. [74]. Here we do not use results derived directly from a RANS simulation of the jet, but instead use the statistics of the LES fields to emulate a RANS simulation. While this approach was taken because of a lack of a readily available, equivalent RANS simulation, an advantage of this emulation can be recognized: it allows us to avoid the discrepancies typically obtained by RANS and LES solutions due to the turbulence and subgrid models used. Here, the relations between turbulence structures and their impact on the time-averaged flow thus are evaluated without differences in the mean flow fields. To distinguish our approach from a direct RANS solution we will refer to it as “emulated RANS” and abbreviate it as eRANS.

The noise source model envisioned in this work uses flow variables available in RANS such as mean velocity, turbulent kinetic energy, and Reynolds stress. Comparison of those flow variables calculated from LES and direct RANS agree well in past works [83], as well as in this work in Chapter 4. Importantly, the peak values of turbulent kinetic energy and Reynolds stress are matched well. A consistent trend is that RANS overpredicts by about 10-20% the length of the potential core relative to the LES. The same observation applies when comparing RANS to experiments [24] and is a well-known shortcoming of RANS closure models for free shear flows [43]. Because the errors are systematic, they can be accounted for in jet noise prediction methodologies [24, 71]. With regards to the eRANS results to be presented here, it is expected that they will capture more faithfully the real mean flow than a direct RANS simulation would. However, a direct RANS solution could be scaled, if necessary, to filter out the effects of the over-predicted potential core length.

The eRANS flow field comprises the mean velocity vector, mean density, turbulent kinetic energy  $k$  and viscous dissipation  $\epsilon$ . The principal component of the Reynolds stress, given

by Eq. (2.12), is modeled as

$$g = \nu_T \left| \frac{\partial \bar{u}}{\partial r} \right| \quad (3.8)$$

where the turbulent viscosity  $\nu_T$  is given by the dimensional construct

$$\nu_T = C_\mu \frac{k^2}{\epsilon} \quad (3.9)$$

The coefficient  $C_\mu$  was set here at the value of 0.067, as will be discussed in Subsection 3.6.3.

Relying again on a dimensional construct, the eRANS-based length scale is

$$L = C_L \frac{k^{3/2}}{\epsilon} \quad (3.10)$$

A related azimuthal scale is based on the above length scale divided by the radial coordinate  $r$  of the relevant surface:

$$\Phi = C_\Phi \frac{k^{3/2}}{\epsilon r} \quad (3.11)$$

In the above relations,  $C_L$  and  $C_\Phi$  are coefficients determined empirically for the LES;  $k$  and  $\epsilon$  are evaluated on the SPS.

LES allows for the direct computation of the turbulent kinetic energy. It does not give directly the viscous dissipation because the energy dissipation combines viscous and filtering effects [15]. The actual viscous dissipation  $\epsilon$  must be computed from the budget of turbulent kinetic energy. Following Darisse *et al.* [37], the dissipation in a turbulent axisymmetric jet

is computed as

$$\begin{aligned} \epsilon = & - \left[ \bar{u} \frac{\partial k}{\partial x} + \bar{v} \frac{\partial k}{\partial r} \right] - \left[ \overline{u'^2} \frac{\partial \bar{u}}{\partial x} + \overline{v'^2} \frac{\partial \bar{v}}{\partial r} + \overline{w'^2} \frac{\bar{v}}{r} + \overline{u'v'} \left( \frac{\partial \bar{v}}{\partial x} + \frac{\partial \bar{u}}{\partial r} \right) \right] \\ & - \left[ \frac{\partial \overline{\kappa u'}}{\partial x} + \frac{1}{r} \frac{\partial (r \overline{\kappa v'})}{\partial r} \right] - \frac{1}{\rho} \left[ \frac{\partial \overline{p'u'}}{\partial x} + \frac{1}{r} \frac{\partial (r \overline{p'v'})}{\partial r} \right] \end{aligned} \quad (3.12)$$

where  $\kappa = (u'^2 + v'^2 + w'^2)/2$  is the instantaneous turbulent kinetic energy. We identify the first term (in brackets) as the advection, the second one as the production, the third one as the turbulent transport, and the fourth one as the transport by pressure fluctuations.

### 3.6.2 Radiator Surface

As the radiator surface marks the transition between the vortical and the linear fields, it is natural to seek a criterion for its location based on the mean vorticity  $\overline{\omega}$ . This reasoning is supported by the fact that the radiator surface encloses well the instantaneous vortical events of the jet, shown in Subsection 3.3.4. It is therefore relevant to study the mean vorticity distribution as a means of developing the desired criterion. Figure 3.28 plots isocontours of normalized mean vorticity magnitude  $|\overline{\omega}|D_j/U_j$  averaged azimuthally. The magnitude peaks at approximately  $|\overline{\omega}|D_j/U_j = 30$  in the shear layer near the nozzle exit, but a smaller dynamic range has been applied to show the vorticity levels at higher radial and axial positions. It is observed that, as with Fig. 3.12, the radiator surface follows the outer edge of the mean vorticity field.

While a fixed threshold of  $|\overline{\omega}|D_j/U_j$  may work well around the potential core of the jet, it will fail downstream as the magnitude of the mean vorticity decays together with the maximum mean velocity of the jet. To account for this, we consider a criterion based on the

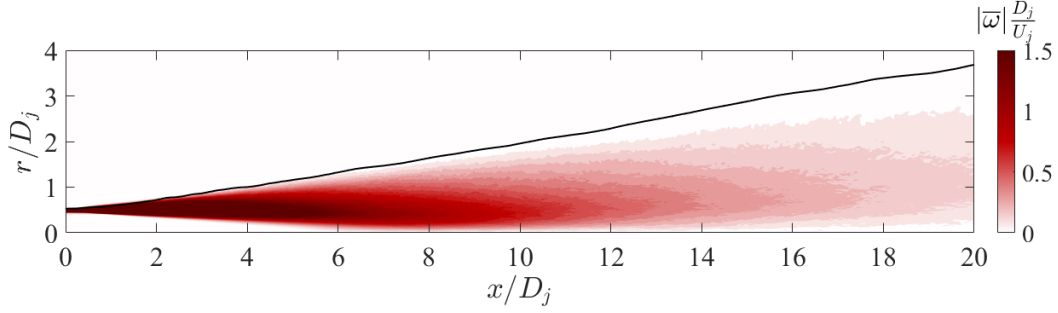


Figure 3.28: Isocontours of normalized magnitude of mean vorticity  $\bar{\omega}D_j/U_j$ . Black line: radiator surface based on  $U_c$ -match criterion.

local mean vorticity. Specifically, we seek the surface defined by

$$|\bar{\omega}|(x, r) = C_\omega |\bar{\omega}|_{\text{MAX}}(x), \quad r \geq r_M(x, \phi) \quad (3.13)$$

where  $|\bar{\omega}|_{\text{MAX}}$  is the outermost maximum of  $|\bar{\omega}|$  at a given axial location,  $r_M$  is the radial location of this maximum, and  $C_\omega$  is a threshold. An excellent agreement is found for  $C_\omega = 0.03$  in Fig. 3.29. Note that the location of the eRANS-based radiator surface is fairly insensitive to  $C_\omega$  as long as  $C_\omega$  is small. Varying  $C_\omega$  from 0.01 to 0.10, for instance, results in a change in the angle of radiator surface of  $\pm 1^\circ$  around the actual angle of  $9^\circ$ . When extended to the three-stream jets in Chapter 4, this criterion produces best results for a value of  $C_\omega = 0.125$ , also included in Fig. 3.29. Even though the two values are different, the resulting surface for  $C_\omega = 0.125$  expands at an angle of  $7.71^\circ$  and is still close to the LES-based radiator surface.

### 3.6.3 Convective Velocity

Recall that, by definition, the convective velocity on the radiator surface equals that on the SPS. The distribution of the eRANS-based Reynolds-stress field defined by Eq. (3.8) is practically identical to that given by LES using Eq. (2.12), displayed in Fig. 3.6, with

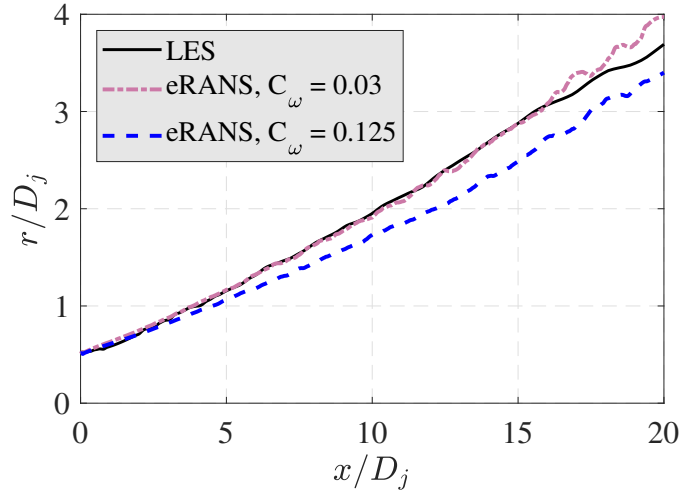


Figure 3.29: Approximation of the radiator surface using  $C_\omega = 0.03$  and  $C_\omega = 0.125$ . The former value is the best approximation for the single-stream jet, the latter is the optimal value for the three-stream jets of Chapter 4.

$C_\mu = 0.067$  in Eq. 3.9. This value is somewhat lower than the commonly used  $C_\mu = 0.09$ , but the value of  $C_\mu$  does not affect the conclusions that follow. Given the strong similarity of the eRANS- and LES-based Reynolds stress fields, the eRANS-based SPS is very close to the LES-based SPS. Following the concept introduced in Subsection 2.4.3, the eRANS-based convective velocity is modeled as the mean axial velocity on the SPS, that is,

$$U_{c,\text{eRANS}} = \bar{u}(x, r = r_{\text{SPS}}) \quad (3.14)$$

where  $r_{\text{SPS}}$  denotes the radial location of the eRANS-based SPS. As shown in Fig. 3.30, a good agreement is obtained between the axial distributions of  $U_{c_p}$  on the radiator surface, derived from the space-time correlations of  $p'$ , and of  $U_{c,\text{eRANS}}$ . Note that this agreement does not involve any tunable parameters.

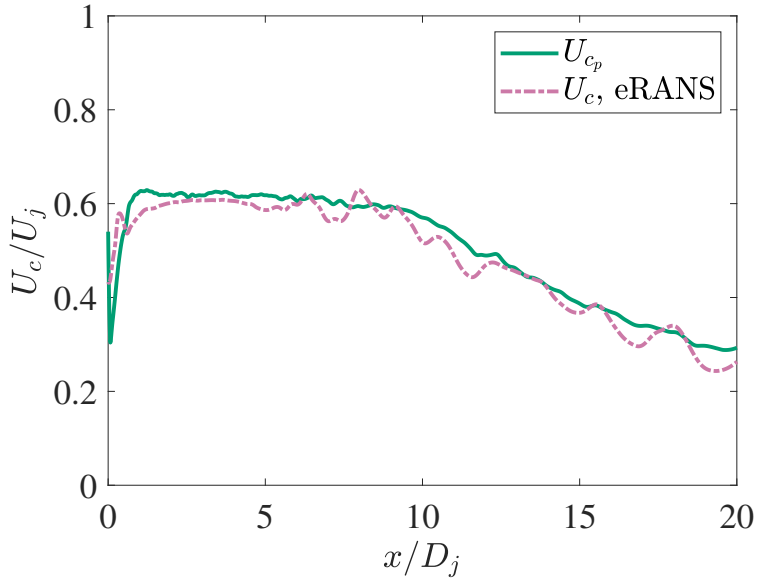


Figure 3.30: Comparison of LES- and eRANS-derived convective velocities on the radiator surface.

### 3.6.4 Length Scales

eRANS-based length scales are evaluated using Eq. (3.10) on the eRANS-derived SPS. They are compared with the LES-derived scales, based on  $p'$ , on the radiator surface in Fig. 3.31. The fixed-frame scale  $L_p$ , which displays a linear growth, is matched well by the eRANS scale with  $C_L = 0.76$ . The trend of the moving-scale scale  $\widehat{L}_p$  is more complex, as discussed in Subsection 3.4.3, and thus not amenable to simple scaling. The rapid initial rise can be modeled by the eRANS scale with  $C_L = 5.65$  up to about  $x/D_j = 2.5$ . A plateau of  $\widehat{L}_p/D_j \approx 1.5$  follows, and an apparently linear growth resumes past the end of the potential core,  $x/D_j \geq 7.5$ . The latter trend can be matched by the eRANS scale with  $C_L = 1.65$ . The complex growth for  $\widehat{L}_p$  suggests different mechanisms for  $p'$  generation in the initial region of the jet and in the region past the end of the potential core. A full understanding of the physics is lacking at this point and will be the topic of future research.

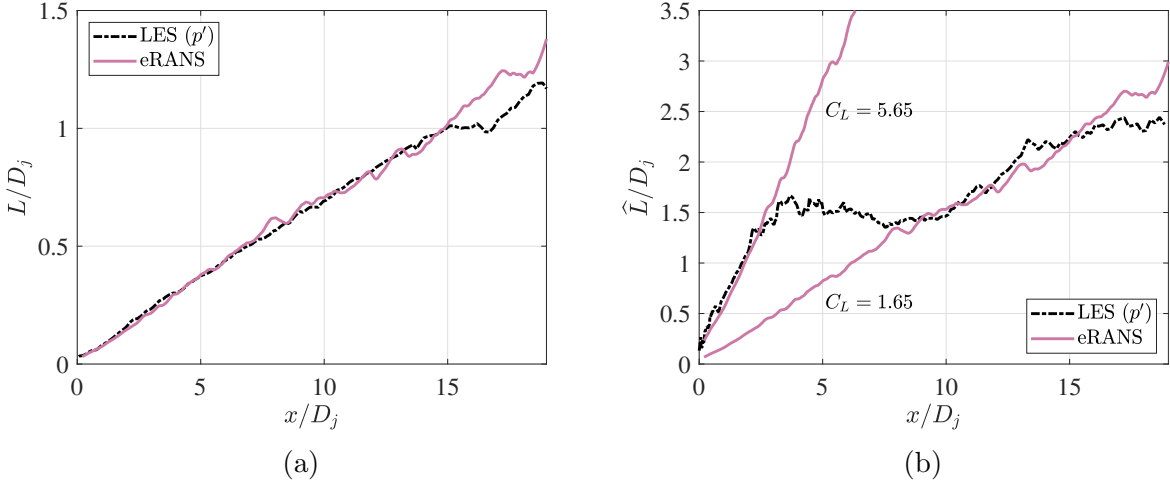


Figure 3.31: Fitting of eRANS-based length scales on the radiator surface. (a) Fixed-frame scale with  $C_L = 0.76$ ; (b) moving-frame scale with  $C_L = 5.65$  and  $C_L = 1.65$  for the initial region and for the region past the potential core, respectively.

### 3.6.5 Azimuthal Scale

The eRANS-based azimuthal scale is calculated from the eRANS length scale divided by the radius of the relevant surface. Here Eq. (3.11) is evaluated with  $k$  and  $\epsilon$  on the SPS and radius  $r$  set to that of the radiator surface. As shown in Fig. 3.32, the coefficient  $C_\Phi = 2.6$  results in a eRANS-based azimuthal scale that provides a fair approximation to the growth and saturation of the LES-derived azimuthal scale based on  $R_{pp}$ .

## 3.7 Summary

This chapter presents an investigation of a highly resolved LES of a Mach 0.9 isothermal turbulent jet to examine the connection between the statistics of the vortical field and the pressure signature of such vortical field on the edge of the jet. The representative locations for those regions are the surface of peak Reynolds stress and the radiator surface, respectively.

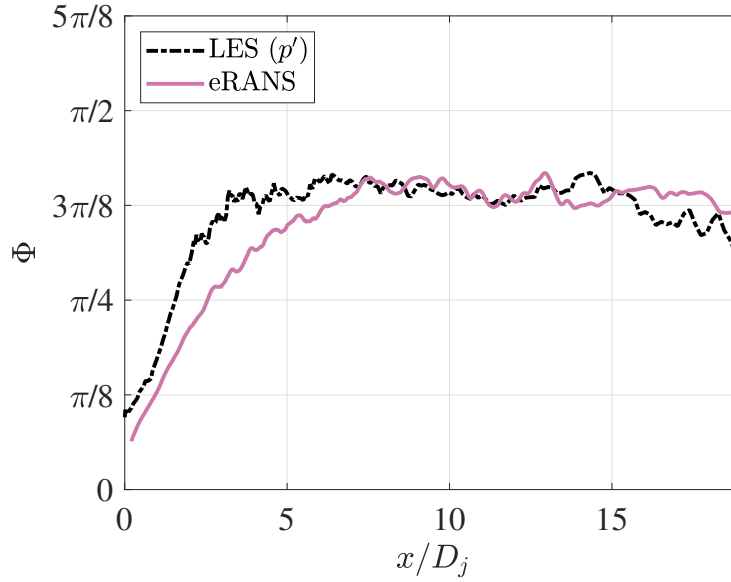


Figure 3.32: Fitting of eRANS-based azimuthal scales on the radiator surface with  $C_\Phi = 2.60$ .

The representative location of the vortical region is the surface of peak Reynolds stress, named the SPS. This surface is an idea proposed by Papamoschou [74] to study the noise-generating shear layer at the location of the outermost peak of the dominant component of Reynolds stress,  $g = |\overline{u'q'}|$ , which is implemented to facilitate the modeling of multi-stream jets. On a single-stream jet, there is only one peak.

Two-point space-time correlations throughout the LES flow allow the calculation of convective velocity,  $U_c$ . Analysis of the convective velocity fields helps identify a criterion for the location of radiator surface, which is a key component for the surface-based model defined in Section 2.4.3, at the edge of the jet. This criterion places the radiator surface at the location near the edge of the jet where the convective velocity equals that on the SPS. That location encloses very well the vortical events of the flow field, and can be accurately reproduced using a criterion based on the magnitude of the mean vorticity.

Two-dimensional space-time correlations are evaluated along a longitudinal and cross-sectional plane. These correlations are centered on points of the SPS. They help us understand the flow phenomena and the basic differences between velocity and pressure fluctua-

tions. Along the  $x - r$  plane, pressure-based correlations exhibit a wave-packet-like pattern that is coherent radially and moves downstream with a uniform convective velocity. The velocity-based correlations show a different behavior, which lacks strong radial coherence and instead acquire a compact shape within the vortical field. These results suggest that velocity-based correlations capture localized turbulent events, whereas the pressure-based correlations are dominated by the “footprint” of the large eddies and their interaction with the surrounding potential flow.

Turbulence axial and azimuthal scales are calculated based on axial velocity fluctuation  $u'$  and pressure fluctuation  $p'$  and plotted along the longitudinal plane. In the case of axial length scales, two definitions are considered: the fixed-frame scale  $L$  and the moving-frame scale  $\widehat{L}$ . The radial variations at several axial locations of fixed-frame length scales collapse well on a single curve when the radial coordinate is transformed to the “similarity” variable  $(r - r_i)/\delta_\theta$ , which considers the radial location of the inner edge of the shear layer ( $r_i$ ) and the momentum thickness ( $\delta_\theta$ ). This collapse of  $L$  works particularly well for axial locations of  $x \geq 3D_j$ . The same scaling is carried out with moving-frame length scales and azimuthal scales with equally good results, with the exception of moving-frame length scales based on pressure whose growth does not follow that of the momentum thickness. Instead, the value of  $\widehat{L}_p$  shows high values at the first few jet diameters, which could be attributed to a different mechanism of turbulence growth.

Lastly, we investigate the feasibility of modeling physically-meaningful turbulence scales from the time-averaged flow field. The LES results are used to emulate a RANS solution. The focus is on  $p'$ -based scales on the radiator surface. eRANS can satisfactorily predict the convective velocity on the radiator surface without any fitting parameters as the mean flow velocity on the SPS. The distributions of azimuthal scale and fixed-frame axial length scale are matched approximately by fitting constants to the eRANS-derived scales. The

distribution of the moving-frame axial length scale is complex and requires a higher level of empiricism.

# Chapter 4

## Study of Three-Stream Jets

This chapter presents the study on two triple-stream jets operating at identical conditions. We first specify the parameters of their flows and the details of their numerical simulations. Each jet is computed through LES and RANS simulations. We compare the two approaches using their time-averaged results, and study the modeling assumptions for turbulence scales of the surface-based model presented in Section 2.4.3. Particular emphasis is placed on studying the flow field near the edge of the jet, where the radiator surface would be located.

### 4.1 Jet Flows

This investigation considers three-stream jets at conditions relevant to variable-cycle engines for supersonic aircraft. The development of three-stream aircraft engines is motivated by their capability of achieving higher efficiency with moderate increase in complexity and weight [99]. Further, their secondary flows present good opportunities to reduce noise generation through enhanced mixing and nozzle asymmetry.

In 2012, Henderson [46] surveyed the acoustics of a three-stream configuration where the core and bypass streams are internally mixed upstream of the tertiary exit; the added tertiary flow reduced high-frequency noise at broadside and peak jet noise angles. Later, Henderson *et al.* [48] conducted acoustic experiments and flow field simulations of jets from three-stream nozzles with axisymmetric and offset configurations for the tertiary stream. The offset tertiary stream reduced noise along the thick side of the jet when the core flow was operating at supersonic conditions. Huff *et al.* [49] assessed the capability of three-stream, offset duct configurations to meet the latest noise standard by ICAO, Chapter 14. The research group at the University of California, Irvine has conducted extensive parametric studies of offset three-stream nozzle concepts and has identified promising quiet configurations that involve duct asymmetry in combination with a wedge-shaped fan flow deflector [81, 84].

### 4.1.1 Jet Parameters

We study the flow fields of two high-speed turbulent jets exiting from the triple-stream nozzles depicted in Fig. 4.1(a). The nozzles have external plugs and the mixing of the streams happens externally. The Cartesian and polar coordinate systems used,  $\mathbf{x} = (x, y, z)$  and  $\mathbf{x} = (x, r, \phi)$ , are illustrated in Fig. 4.1(b). The origin of the axial coordinate  $x$  is at the plug tip. Subscripts  $p$ ,  $s$  and  $t$  refer to the primary (inner), secondary (middle) and tertiary (outer) streams, respectively. The azimuthal angle  $\phi$  is defined relative to the downward vertical direction. Both nozzles have the same duct exit areas and plug dimensions. The effective (area-based) exit diameter of the primary duct is  $D_{p,eff} = 13.33$  mm, the secondary-to-primary area ratio is  $A_s/A_p = 1.44$  and the tertiary-to-primary area ratio is  $A_t/A_p = 1.06$ . The diameter of the tertiary duct is  $D_t = 0.0381$  m. The plug diameter is 23.80 mm and its length, as measured from the primary exit plane to the plug tip, is 38.40 mm.

Nozzle AXI04U is coaxial and thus features uniform distributions of secondary and tertiary duct exit widths at  $W_s/D_{p,eff} = 0.219$  and  $W_t/D_{p,eff} = 0.127$ , respectively. Nozzle ECC09U has the same primary and secondary ducts as AXI04U but features a tertiary duct of variable exit width  $W_t(\phi)$ , plotted in Fig. 4.1 (c). The distribution is symmetric around the plane  $z = 0$ . Compared to nozzle AXI04U, the tertiary duct of ECC09U is wider in the annular segment  $-110^\circ < \phi < 110^\circ$  and thinner elsewhere. On the top of the nozzle, the tertiary duct closes completely by means of a wedge-type deflector of axial length of  $2.1D_{p,eff}$  and half angle  $\delta = 25^\circ$ . This eccentric tertiary duct causes a thickened tertiary flow on the underside of the nozzle.

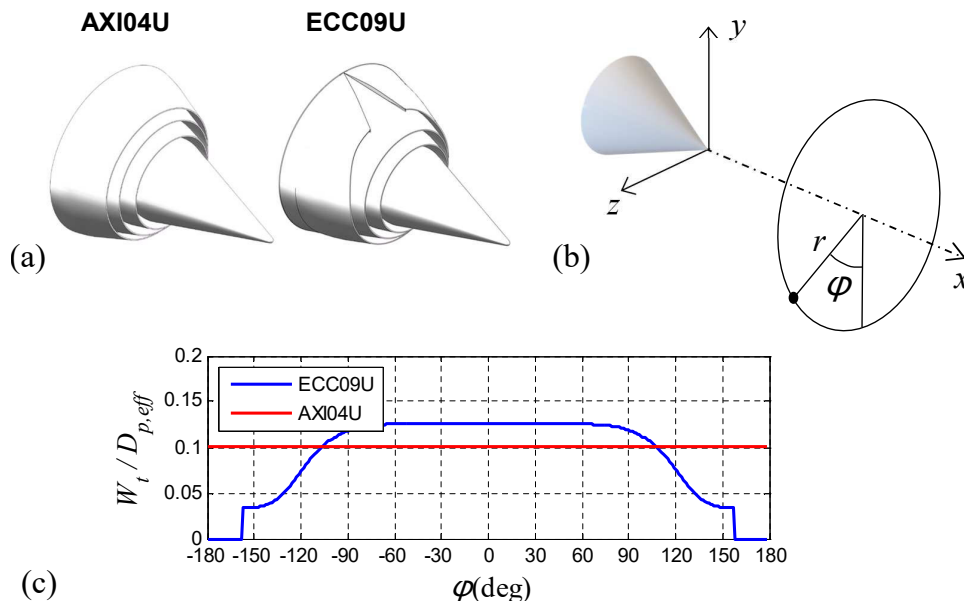


Figure 4.1: Characteristics of three-stream nozzles. (a) Exit geometry of nozzles; (b) coordinate system; (c) azimuthal variation of the tertiary annulus width.

The flow conditions are common for both nozzles and are listed in Table 4.1. They represent typical exhaust conditions for a supersonic turbofan engine [84]. The nozzle pressure ratio (NPR) is the ratio of the stagnation pressure to the ambient pressure, the nozzle temperature ratio (NTR) is the ratio of the jet stagnation temperature to ambient temperature,  $A$  is the exit cross-sectional area,  $\dot{m}$  is the mass flow rate,  $M$  is the fully-expanded Mach

Stream	NPR	NTR	$M$	$\dot{m}/\dot{m}_p$	$A/A_p$	$U$ (m/s)
Primary	2.06	3.38	1.07	1.00	1.00	590
Secondary	2.03	1.34	1.06	2.33	1.44	370
Tertiary	1.53	1.24	0.81	1.31	1.06	282

Table 4.1: Flow conditions.

number, and  $U$  is the fully-expanded velocity. The Reynolds number based on the primary exit conditions and  $D_{p,eff}$  is  $1.03 \times 10^5$ .

Jets AXI04U and ECC09U were part of a campaign to investigate the acoustics of coaxial and asymmetric three-stream jets [80, 84]. Small-scale experiments utilized helium-air mixtures to match the flow conditions shown in Table 1. To demonstrate the noise suppression ability of the eccentric tertiary flow, Fig. 4.2 plots the far-field narrowband spectra of jets AXI04U and ECC09U in the downward polar direction of peak emission (approximately  $35^\circ$  below the jet axis)[80]. The spectra are plotted versus the laboratory frequency, which is about 50 times larger than the full-scale frequency for a supersonic business jet. The eccentricity of the tertiary duct in ECC09U yields large reductions, as much as 12 dB, at full-scale frequency in the range of 200 - 500 Hz. Understanding and modeling the physical mechanisms of this reduction motivates the research effort discussed in this section.

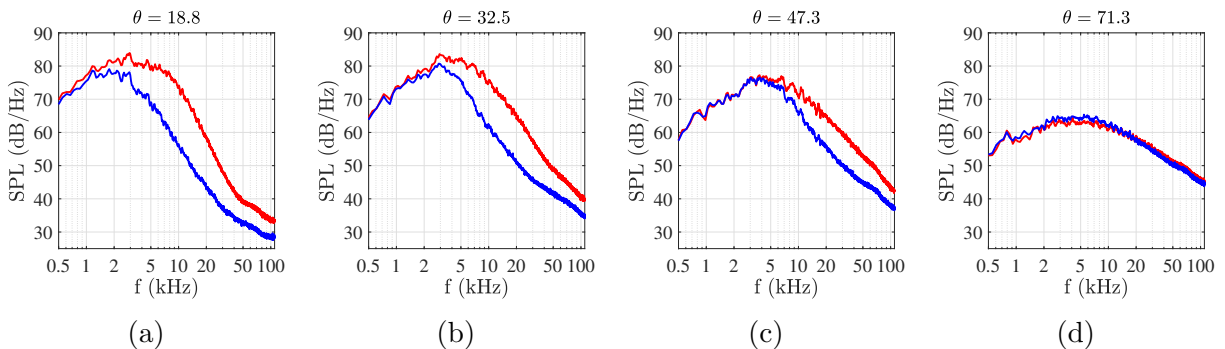


Figure 4.2: Far-field sound pressure level spectra of jets AXI04U (red) and ECC09U (blue) various polar angles  $\theta$  with respect to the downstream axis.

In the presentation of the results that follow, equivalent length and velocity scales will be used to properly normalize the coordinates and flow variables. The equivalent diameter  $\hat{D}$

is based on the total exit cross-sectional area and has the value of 24.9 mm. The equivalent velocity is the mass-flow-rate averaged velocity

$$\hat{U} = \frac{\dot{m}_p U_p + \dot{m}_s U_s + \dot{m}_t U_t}{\dot{m}_p + \dot{m}_s + \dot{m}_t} \quad (4.1)$$

and has the value of 435 m/s. The Reynolds number based on mass-flow-rate averaged values of velocity and kinematic viscosity and equivalent diameter is  $3.7 \times 10^5$ .

### 4.1.2 Computational Details

The computational effort encompassed Reynolds-Averaged Navier Stokes (RANS) solutions and Large Eddy Simulations (LES) performed at the conditions of Table 4.1 and the Reynolds numbers listed in the previous section. The computational fluid dynamics code is known as PARCAE [115] and solves the unsteady three-dimensional Navier-Stokes equations on structured multiblock grids using a cell-centered finite-volume method.

The RANS computations use the Jameson-Schmidt-Turkel dissipation scheme [51] and the Shear Stress Transport (SST) turbulence model of Menter [66]. The solver has been used in past research on dual-stream jets, and its predictions have been validated against mean velocity measurements for dual-stream jets [115].

The LES computations use implicit backward three-layer second-order time integration with explicit five stage Runge-Kutta dual time stepping, residual smoothing, and multigrid techniques for convergence acceleration. The spatial discretization of the inviscid flux is based on the weighted averaged flux-difference splitting algorithm of Roe [94, 98]. The viscous flux is discretized using a second-order central difference scheme. The time-evolving jet flow is simulated using a hybrid RANS/LES approach [101]. The Spalart-Allmaras turbulence model [100] is used to model the turbulent viscosity near the walls, while in the free shear flow

the computation relies on the subtle dissipation of the upwind scheme, using the method proposed by Shur *et al.* [98]. Experimental mean-velocity profiles of cold jets issuing from the nozzles of this study have been well replicated by the LES predictions; in addition, LES-based predictions of far-field sound pressure level spectra (in conjunction with a Ffowcs-Williams-Hawkings surface) have replicated satisfactorily experimental spectra for the nozzles and operating conditions of this study [114].

The computations encompassed both the internal nozzle flow as well as the external plume. At the inlet surface of each nozzle stream, the boundary conditions specified uniform total pressure and total temperature corresponding to their perfectly expanded exit Mach number. The ambient region surrounding the nozzle flow had a characteristic boundary condition, and the downstream static pressure was set to the ambient pressure. The nozzle walls had an adiabatic, no-slip boundary condition. To aid convergence, the RANS and LES simulations were conducted with a freestream Mach number of 0.05, equivalent to a velocity of 17 m/s.

For the RANS solutions, the mesh contained approximately 8 million grid points and extended to  $46\hat{D}$  axially and  $12\hat{D}$  radially. As the nozzles are symmetric around the  $x - y$  plane, only one half of the jet flows were modeled to save computational cost. The LES grids contained about 44 million grid points each and extended to  $46\hat{D}$  axially and  $23\hat{D}$  radially.

The results of nozzle AXI04U were calculated with 4100 time frames after the transient period at a time step of  $\Delta t = 10\mu s$ , yielding a simulation time of  $716\hat{D}/\hat{U}$ . The simulation of jet ECC09U had 4039 time frames with the same time step, resulting in a simulation time of  $705\hat{D}/\hat{U}$ . Given that nozzle AXI04U is axisymmetric, its results are averaged in the azimuthal direction whenever possible to improve smoothness. The same treatment is not applicable to jet ECC09U.

The LES flow field enables two-point space-time correlations throughout the domain, which are already defined in Section 3.2 and Eq. 3.1. Here we consider correlations between two flow variables  $a'(\mathbf{x}, t)$  and  $b'(\mathbf{x}, t)$  with zero means, so their normalized space-time correlation is defined by

$$R_{ab}(\mathbf{x}_0, \mathbf{x}, \tau) = \frac{\overline{a'(\mathbf{x}_0, t) b'(\mathbf{x}, t + \tau)}}{\left(\overline{a'(\mathbf{x}_0)^2} \overline{b'(\mathbf{x})^2}\right)^{1/2}} \quad (4.2)$$

where  $\mathbf{x}_0$  is the reference location,  $\mathbf{x}$  is the displaced location,  $\tau$  is the time separation, and the overline denotes time averaging. Equation 4.2 assumes stationarity in time  $t$ . In the analysis that follows we will consider space-time correlations of the pressure fluctuation  $p'$  with itself, ( $R_{pp}$ ), axial velocity fluctuation  $u'$  with itself ( $R_{uu}$ ), as well as  $u'$  with  $p'$  ( $R_{up}$ ). In section 4.4.3, we consider the correlation between azimuthal vorticity fluctuation  $\omega'_\theta$  and pressure fluctuation  $p'$  ( $R_{\omega_\theta p}$ ).

Similarly to the single-stream jet of Chapter 3, the space-time correlations enable calculation of the convective velocity  $U_c$  by locating the time separation where the correlation peaks. Due to a higher flow complexity, this calculation will be restricted to axial displacements only, with  $\mathbf{x}_0 = (x_0, r_0, \phi_0)$  and  $\mathbf{x} = (x_0 + \xi, r_0, \phi_0)$  in this chapter. The resulting axial convective velocity  $U_c$  will be based on  $R_{pp}$  and  $R_{uu}$ . Figure 3.3 shows examples of several space-time correlations for jet AXI04U centered around a point at  $x/\hat{D} = 4$ , on the OSPS.

## 4.2 Mean Flow Fields

### 4.2.1 Mean axial velocity

Figures 4.4 and 4.5 plot isocontours of the normalized mean axial velocity,  $\bar{u}/\hat{U}$ , on the plane of symmetry of jets AXI04U and ECC09U, respectively, and compare the RANS and

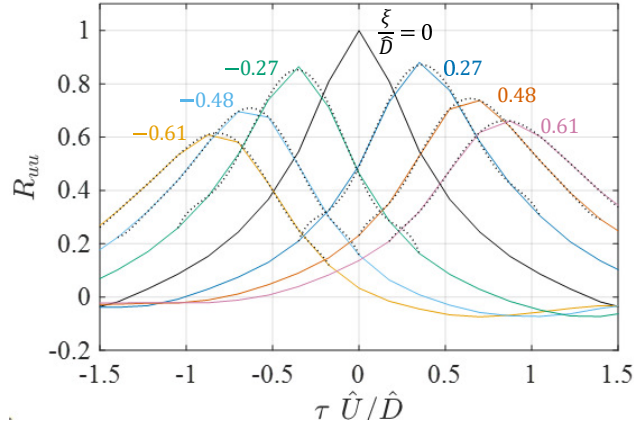


Figure 4.3: Space-time correlation  $R_{uu}$  on the OSPS at  $x/\hat{D} = 4$  for jet AXI04U. Dashed lines indicate fits by seventh-order polynomials to accurately detect the peak of each correlation.

LES solutions. The LES and RANS flow fields are very similar, with the LES predicting slightly faster spreading and thus moderately shorter primary potential cores. It is also noted that the wake from the plug is accentuated in the RANS solutions. For jet ECC09U, the asymmetry produced by the eccentricity of the nozzle is evident: there is a significant concentration of low-speed flow on the underside of the primary jet. The lack of tertiary flow on the upper side of ECC09U results in faster growth of the upper portion of the shear layer, thus the potential core for ECC09U is slightly shorter than for AXI04U. We define the length of the primary potential core  $L_p$  as the distance from the exit of the primary nozzle (located at  $x/\hat{D} = -1.7$ ) to the point where the maximum mean axial velocity equals  $0.9U_p$ . For jet AXI04U, LES gives  $L_p/\hat{D} = 4.7$  and RANS gives  $L_p/\hat{D} = 6.7$ . For jet ECC09U, the corresponding values are  $L_p/\hat{D} = 4.4$  and  $6.4$ . As has been noted in previous studies [24, 114], the RANS solution has the tendency to over-predict the length of the potential core. Despite this limitation, RANS-based noise predictions can provide useful guidance for the design of quiet propulsion systems [24].

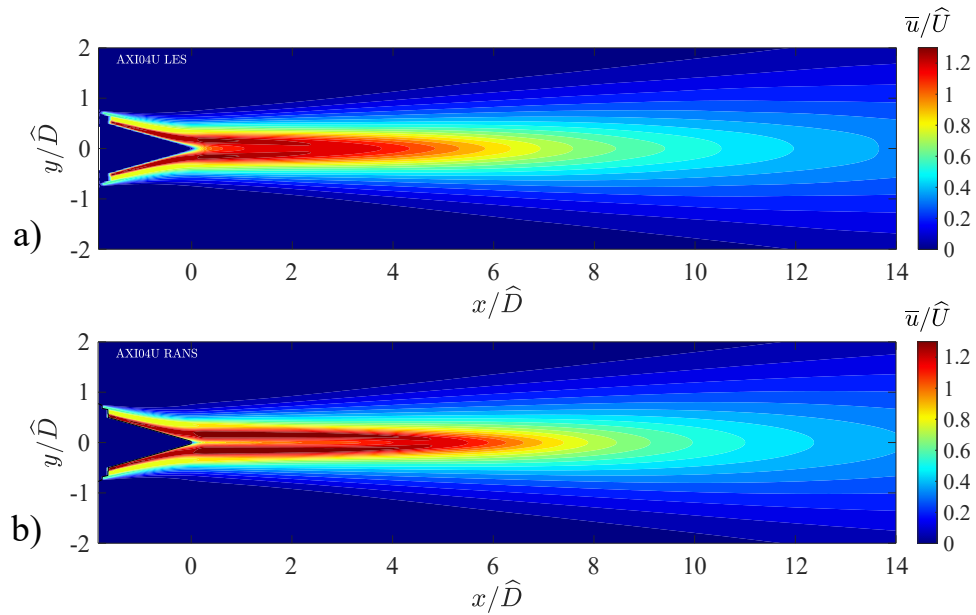


Figure 4.4: Isocontours of normalized normalized mean axial velocity  $\bar{u}/\hat{U}$  on the symmetry plane of jet AXI04U. a) LES and b) RANS.

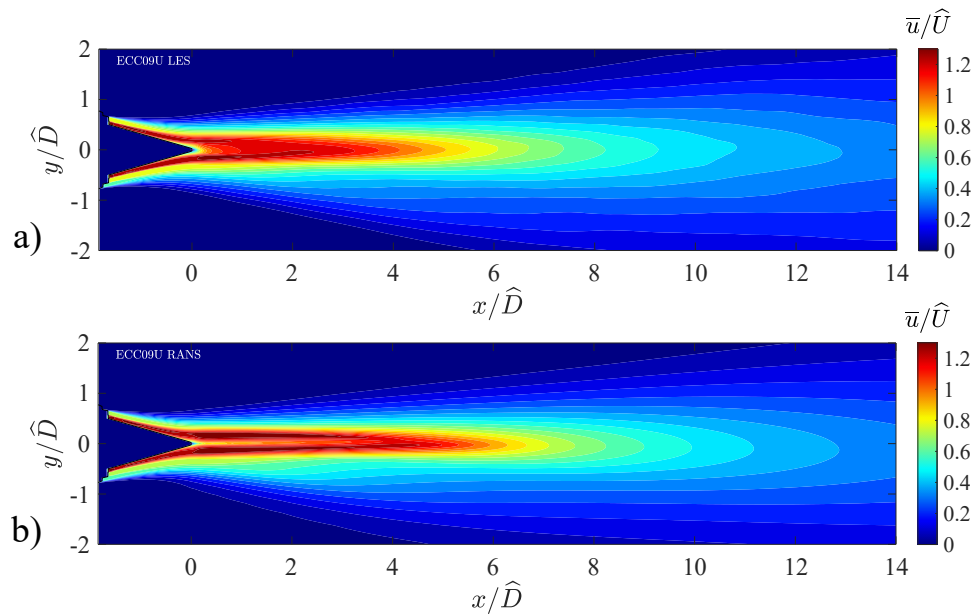


Figure 4.5: Isocontours of normalized normalized mean axial velocity  $\bar{u}/\hat{U}$  on the symmetry plane of jet ECC09U. a) LES and b) RANS.

## 4.2.2 Reynolds stress

We examine distributions of the magnitude of the principal component of the Reynolds stress tensor  $g = |\overline{u'q'}|$  already presented theoretically in Section 2.4.3 and in application to the single-stream jet in Section 3.3.2. The areas of high Reynolds stress may provide valuable information towards the modeling of the effects of the noise-generating turbulence eddies.

Figure 4.6 plots isocontours of normalized Reynolds stress  $g/\widehat{U}^2$  for nozzle AXI04U as predicted by LES and RANS. Two distinct shear layers are evident near the nozzle exit, plus the plug wake. The outer shear layer caused first by the tertiary stream, and then by the mixed flow of tertiary and secondary streams, interacting with the ambient air. The shear layer between the secondary and tertiary stream is weak and short-lived, so it is not visible in the contour plot. This is in part because those streams do not have a big difference in velocity, and in part because the tertiary stream is thin.

As noted in the discussion of the mean velocity profiles, the LES predicts faster mixing rates and consequently higher interaction between primary and secondary streams, visible as inner lobes of Reynolds stress near the tip of the plug in Fig 4.6. The outer shear layers gradually merge into the primary shear layer; this merging is complete by  $x/\widehat{D} = 2$  for LES and  $x/\widehat{D} = 3$  for RANS. The merged shear layers show a peak Reynolds stress of  $g/\widehat{U}^2 = 0.010$  occurring at  $x/\widehat{D} = 4.4$  for the LES solution, and of  $g/\widehat{U}^2 = 0.012$  at  $x/\widehat{D} = 5.0$  for the RANS solution. Overall, the comparison between RANS and LES is very good both in terms of levels and shapes of the distributions.

The analogous plot of Reynolds stress for ECC09U is shown in Fig. 4.7. The non-smoothness of the LES distribution is due to the limited number of time steps of the solution. On the underside of the jet, the thicker tertiary flow slows down the spreading of the primary shear layer and results in a large suppression of the Reynolds stress. Importantly, the peak Reynolds stress shifts to a lower-speed region, compared to AXI04U, meaning that the most

energetic eddies in contact with the ambient have slower convection speed. On the upper side, where there is no tertiary stream, the level of the Reynolds stress is slightly higher than in AXI04U. As for the axisymmetric case, the LES predicts moderately faster mixing rates than does RANS.

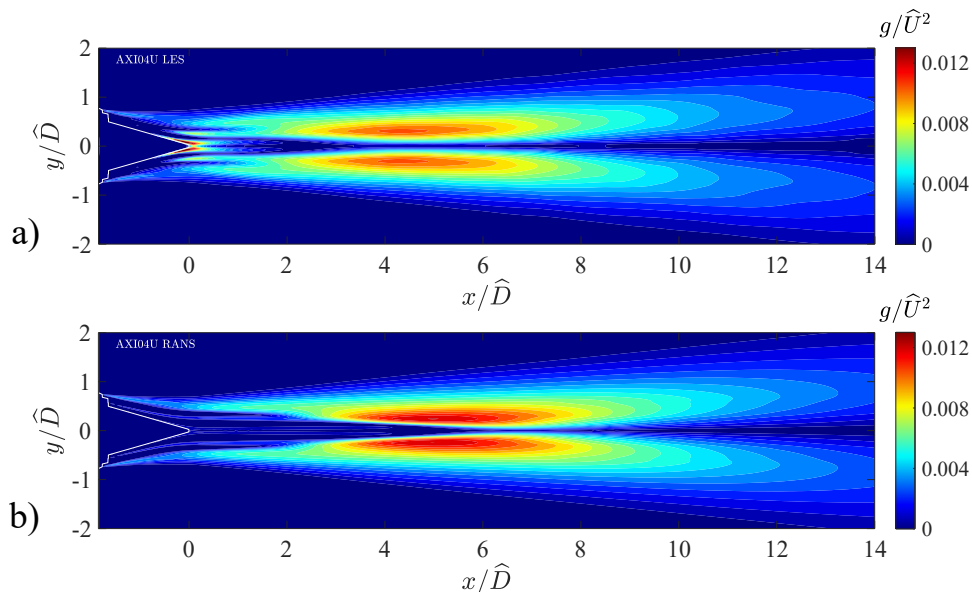


Figure 4.6: Isocontours of normalized Reynolds stress  $g/\widehat{U}^2$  on a symmetry plane of jet AXI04U. a) LES and b) RANS.

### 4.3 Outer surface of peak stress

In the acoustic analogy model of Ref. [74] it was surmised that, in multi-stream jets with velocity ratios of relevance to aeroengines, the turbulent eddies in direct contact with the ambient air are the principal noise generators. In a three-stream jet these eddies are initially in the tertiary (outer) shear layer, then progressively transition to the secondary and primary shear layers as the tertiary and secondary flows become mixed with the primary flow (Fig. 2.7). In the context of RANS, the action of those eddies is represented by the statistics on the outer-most peak of the Reynolds stress  $g$ , that is, the first peak of  $g$  as one approaches the jet radially from the outside towards the centerline. This results in the

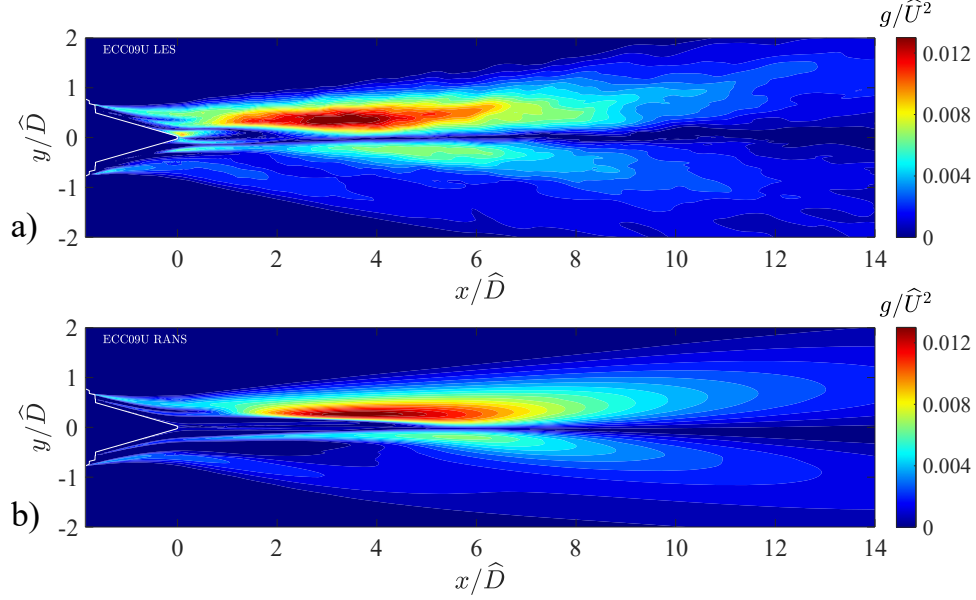


Figure 4.7: Isocontours of normalized Reynolds stress  $g/\widehat{U}^2$  on the symmetry plane of jet ECC09U. a) LES and b) RANS.

concept of the “outer surface of peak stress” (OSPS), which is thought to be important in the understanding and modeling of multi-stream jet noise. Among the most important properties of the eddies in contact with the ambient is their convective velocity  $U_c$  and convective Mach number  $M_c = U_c/a_\infty$ , where  $a_\infty$  is the ambient speed of sound. The convective Mach number governs the efficiency with which the eddies radiate sound to the far field; it is thus of paramount significance in the modeling.

The procedure for the detection of the OSPS is a modification of that described in Ref. [74]. At a given axial location, the OSPS is detected by constructing rays along the direction of the mean velocity gradient that propagate from the ambient towards the center of the jet; the first (outermost) maximum of the Reynolds stress  $g$  along each ray marks the location of the OSPS. This procedure is common for the RANS flow field and the time-averaged LES flow field. Figure 4.8 offers an example for jet ECC09U based on the RANS solution. The rays start from the low speed region of the jet and propagate inward. They terminate at the

first maximum of  $g$ , thus defining the OSPS at that particular cross plane. The inner peak of the Reynolds stress is also visible in the figure.

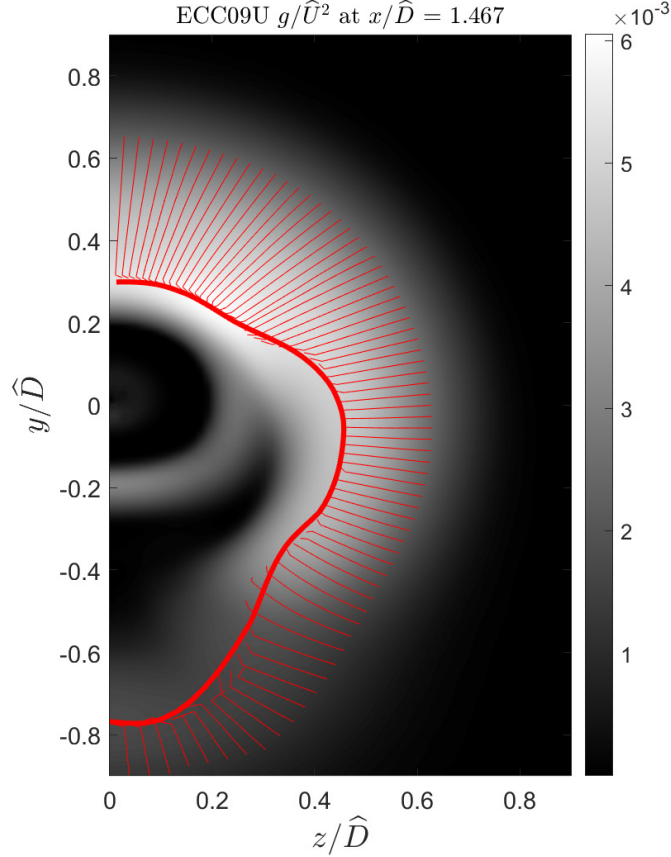


Figure 4.8: Detection of the outer surface of peak Reynolds stress (OSPS) at  $x/\hat{D} = 1.467$  for jet ECC09U. Contours indicate the distribution of Reynolds stress on this cross-stream plane. Thin red lines: rays along the mean velocity gradient. Thick red line: OSPS

For the RANS flow field, once the OSPS has been detected, the convective velocity is modeled as the mean axial velocity on the OSPS. Denoting the radius of the OSPS as  $r_{\text{OSPS}}(x, \phi)$ , the convective velocity is expressed as

$$U_c(x, \phi) = \bar{u}(x, r_{\text{OSPS}}(x, \phi), \phi) \quad (4.3)$$

For the LES flow field, the convective velocity on the OSPS is determined directly by the space-time correlation of Eq. 4.2 based on the axial velocity fluctuation,  $u'$ .

Three-dimensional views of the the RANS- and LES-derived OSPS for the jets of this study are shown in Figs. 4.9 and 4.10, respectively. Color contours indicate the distribution of the convective Mach number  $M_c$  on the surfaces. It is evident that LES and RANS produce similar surfaces, with moderate variations in geometry and levels of  $M_c$ . The LES surface for ECC09U is jagged due to the limited number of time steps (the corresponding surface for AXI04U appears smoother because it is averaged azimuthally). The OSPS of jet AXI04U shows a subtle convergence where the tertiary shear layer becomes mixed with the secondary shear layer, followed by a more pronounced convergence where the outer streams become totally mixed with the primary shear. This sudden collapse is followed by a gradual convergence near the end of the primary potential core, downstream of which the OSPS diverges slowly. The peak  $M_c$  occurs shortly downstream of the depletion of the outer streams. The asymmetry of nozzle ECC09U has a strong effect on the shape of its OSPS. The convergence from tertiary to secondary shear layer, as well as the stronger collapse on the primary layer, have a clear dependence on the azimuthal angle  $\phi$ . Those transition points move downstream as  $\phi$  tends to 0, the downward direction. In addition, in the proximity of  $\phi = 0^\circ$ , the tertiary shear layer interacts minimally with the secondary and primary layers: it diverges until it vanishes due to spreading. At that point, it stops representing the outer peak of Reynolds stress and the OSPS collapses on the primary shear layer. This creates the “bulge” visible in the downwards direction of Figs. 4.9(b) and 4.10(b). Overall, the outward deflection of the OSPS on the underside of the jet causes a large reduction in convective Mach  $M_c$ . This is key to the noise reduction induced by nozzle ECC09U in the downward direction, as seen in Fig. 4.2.

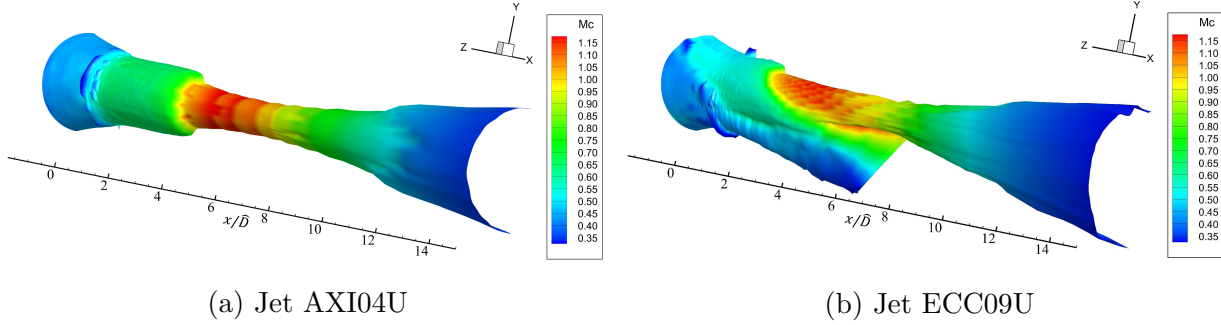


Figure 4.9: RANS-based OSPS with contours of convective Mach number  $M_c$ .

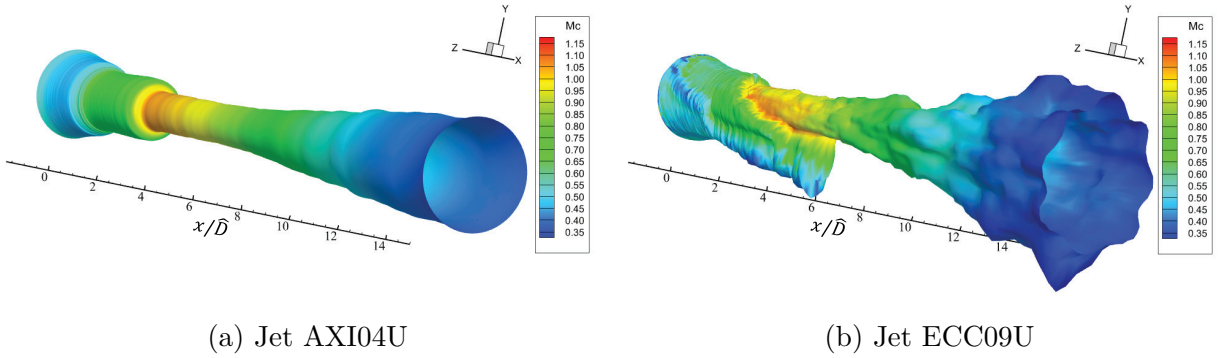


Figure 4.10: LES-based OSPS with contours of convective Mach number  $M_c$ .

### 4.3.1 Comparisons of LES and RANS results

Having discussed the detection and broad features of the OSPS, we proceed with detailed comparisons of the geometries and convective velocity distributions obtained by the RANS and LES solutions for the OSPS of jets AXI04U and ECC09U.

#### Jet AXI04U

Figure 4.11(a) plots the radial coordinates of the OSPS of jet AXI04U as computed by RANS and LES. The two predictions are practically identical up to  $x/\hat{D} = 1.7$ , with the plot showing clearly the inward transition of the OSPS from the tertiary to the secondary, and then to the primary shear layer. This transition occurs in LES about 0.8 diameters

upstream than in RANS. For  $x/\hat{D} > 1.7$ , the two surfaces are close but the LES result is shifted outward, reflecting the faster spreading of the LES jet.

The comparison of convective velocities on the OSPS is seen in Fig. 4.11(b). The RANS- and LES-based trends are similar and show an increase in  $U_c$  as the most energetic eddies move from the tertiary (low speed) to the secondary (medium speed), and then to the primary (high speed) shear layer. At this point the convective velocity peaks and starts to decline, following the decay of the mean velocity past the end of the potential core. Those three initial velocity levels are approximately  $0.36\hat{U}$ ,  $0.55\hat{U}$ , and  $0.82\hat{U}$  and correspond to  $0.56U_t$ ,  $0.64U_s$ , and  $0.60U_p$  respectively, which are close to the typical value of  $0.6U_j$  in the case of single-stream jets[25]. There are moderate quantitative differences between the RANS and LES results, with RANS predicting a peak value of  $U_c$  that is about 14% higher than that predicted by LES. These peaks of  $U_c$  also take place at slightly different locations,  $x/\hat{D} = 3.6$  for RANS and  $x/\hat{D} = 2.0$  for LES, which is explained by the difference in transition to the primary stream in each OSPS.

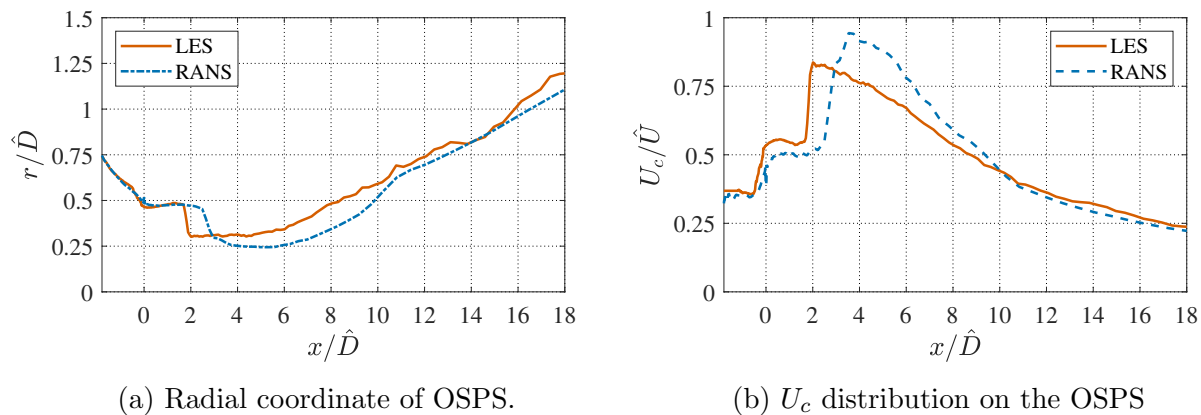


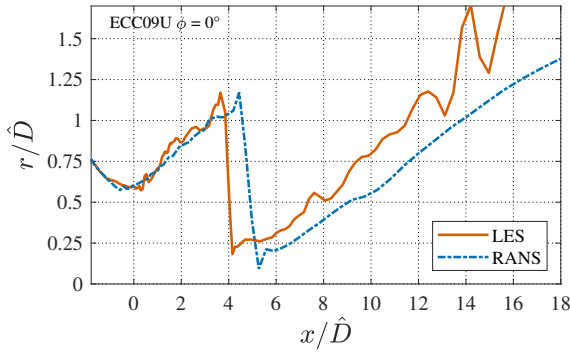
Figure 4.11: RANS and LES results regarding the OSPS of jet AXI04U.

## Jet ECC09U

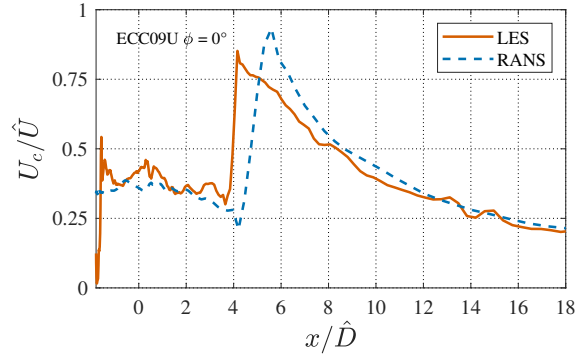
Because of the eccentricity of nozzle ECC09U, the resulting OSPS shape is dependent on the azimuthal angle  $\phi$ . For brevity we only show comparisons for  $\phi = 0^\circ$  and  $\phi = 180^\circ$ . The radial coordinate results for  $\phi = 0^\circ$  are plotted in Fig. 4.12(a). There is reasonable agreement between the RANS and LES predictions, both capturing the collapse of the OSPS near  $x/\hat{D} = 4.3$ , where the outer shear layer vanishes and the OSPS transitions to the primary shear layer. The axial location of this transition is earlier in the LES than in the RANS solution, consistent with the faster spreading of the LES flow, also seen for jet AXI04U. Downstream of this transition the curves have similar trends, with the LES-based OSPS showing a faster spreading and therefore an outward shift. Past  $x/\hat{D} = 13$  the LES-based OSPS loses accuracy due to the lack of convergence of the statistics.

Figure 4.12(b) compares convective velocities obtained by modeling on RANS and two-point correlations on LES. The noise on the LES-based  $U_c$  at  $x/\hat{D} < -1$  is not considered physical but a result of the numerical difficulty in locating the OSPS and performing two-point correlations very close to the tertiary nozzle lip. Overall, the LES and RANS curves are similar and show a slightly decaying  $U_c$  where the OSPS occurs on the outer shear layer. Near  $x/\hat{D} = 4.3$ , the collapse of the OSPS to the primary shear layer causes the convective velocity to rise suddenly. The LES predicts a peak  $U_c$  value about 9% lower than that obtained from the RANS solution.

Corresponding results for  $\phi = 180^\circ$  are shown in Fig. 4.13. The radial coordinates show similar trends, with an overall faster spreading of the LES jet. Because the tertiary stream is deflected away from the top of the nozzle, the OSPS follows the secondary shear layer, which is quickly merged with the primary shear layer. This transition occurs near  $x/\hat{D} = 0.7$  for LES and around  $x/\hat{D} = 1.2$  for RANS. Downstream of this transition, the LES result shows a more rapid spreading rate. Despite the location discrepancy seen in Fig. 4.13(a),



(a) Radial distribution of OSPS.



(b)  $U_c$  distribution on the OSPS

Figure 4.12: RANS and LES results regarding the OSPS of jet ECC09U on  $\phi = 0^\circ$ .

the RANS- and LES-based convective velocities plotted in Fig. 4.13(b) are still in overall agreement. Similarly to jet AXI04U, there is a stepped increment in the convective velocity as the shear layers mix. In this case, because the tertiary flow is deflected such that there are only primary and secondary flows at the top of the jet, only one sudden rise is seen. The fact that LES predicts the transition from secondary to primary shear layer upstream from RANS naturally leads to an earlier rise of the corresponding convective velocity. After that, the lower LES-based  $U_c$  is explained by the faster spreading of the OSPS.

Comparing the  $U_c$  distribution on the underside of jet ECC09U (Fig. 4.12(b)) with that of jet AXI04U (Fig. 4.11(b)) we note a substantial reduction in the region  $0 \leq x/\hat{D} \leq 4$ . This region influences the middle and high frequencies, which are of particular relevance to aircraft noise. The peak convective Mach number in that region is reduced from 1.06 to 0.57 in the LES solution; and 1.06 to 0.48 in the RANS solution. This reduction occurs because the outer-most eddies are shifted to a lower velocity regime. The resulting decrease in radiation efficiency is evident by the large reduction in sound pressure level seen in Fig. 4.2 at the mid and high frequencies. Even though there are discrepancies on the order of 10% between RANS and LES in the prediction of  $U_c$ , RANS captures well the changes in  $M_c$ , and their spatial extent, and is thus expected to provide useful guidance in a differential noise prediction model.

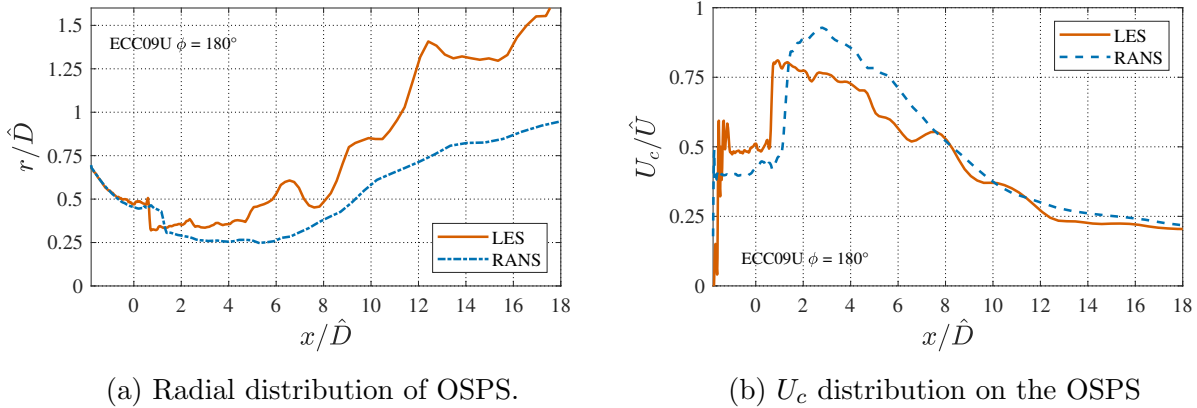


Figure 4.13: RANS and LES results regarding the OSPS of jet ECC09U on  $\phi = 180^\circ$ .

## 4.4 Radiator surface

The concept of a radiator surface as the location where the noise sources are prescribed was explained previously in Chapter 2. Here we extend the  $U_c$ -match criterion explained in Section 3.3.3 to the three-stream jets AXI04U and ECC09U, as the surface near the edge of the jet where the  $R_{pp}$ -based  $U_c$  matches the  $R_{uu}$ -based  $U_c$  on the OSPS at the same axial and azimuthal locations.

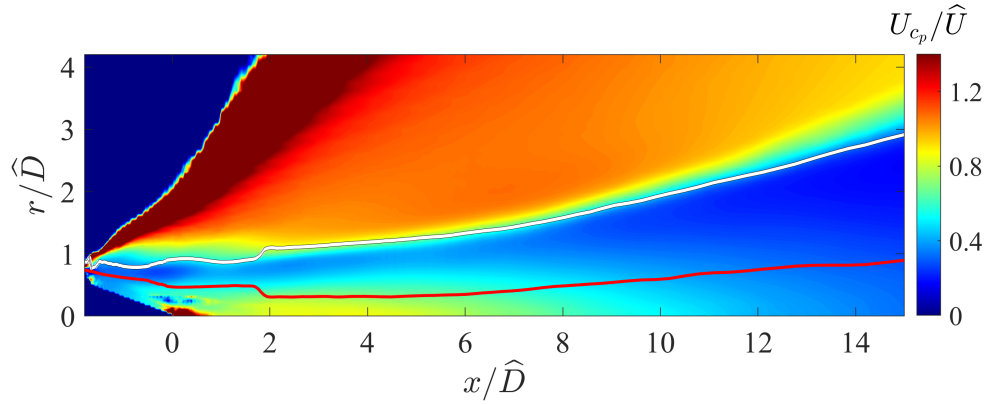
### 4.4.1 Distribution of Convective Velocity

Figure 4.14 displays isocontours of pressure-based convective velocity  $U_{c_p}$ , normalized by the equivalent velocity  $\hat{U}$ , on the meridional planes of jet AXI04U and jet ECC09U at  $\phi=0^\circ$  and  $\phi=180^\circ$ . The result for AXI04U has been averaged in the azimuthal direction. The distribution of  $U_{c_p}$  on the three-stream jets is similar to that of the single-stream jet of Chapter 3: at a given axial location,  $U_c$  has a radial trend whereby it decreases outside the OSPS, reaches a minimum, then rises sharply. The sharp rise is associated with the transition from the hydrodynamic to the acoustic fields. Previous studies have also shown similar trends in multi-stream jets [25, 102]. Comparing the two angles of jet ECC09U in

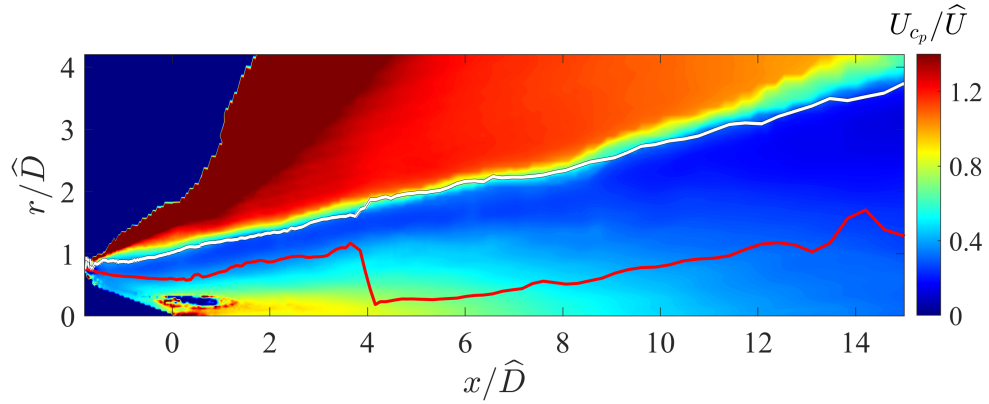
Figs. 4.14(b,c), it is evident how the presence of a tertiary flow at  $\phi = 0$  causes a wider jet expansion, as seen by the steeper angle of the radiator surface.

The analogous distributions of velocity-based convective velocity  $U_{cu}$  are plotted in Fig. 4.15. Again, the general trends are very similar to those shown for the single-stream jet in Chapter 3. Inside the vortical region,  $U_{cu}$  follows the same behavior as the mean velocity, but its radial decay is steeper than  $U_{cp}$  (see Fig. 3.10). The region of radial minima near the edge of the jet happens outwards from the similar feature of  $U_{cu}$ , and in fact, it is very close to the location of the radiator surface. Near the OSPS, the values of  $U_{cu}$  and  $U_{cp}$  are very similar. It should be noted that the  $R_{uu}$  correlations cause strong numerical artifacts in the linear region and at high polar angles in the form of a layer of high  $U_{cu}$ , which should be disregarded.

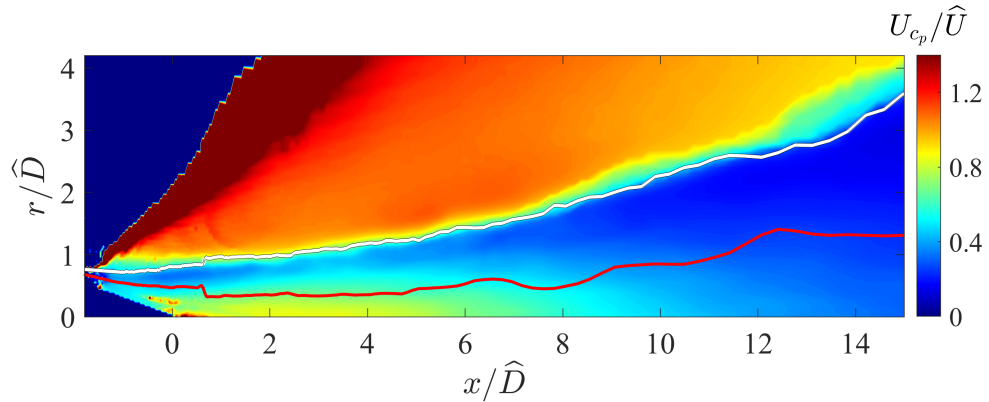
The radiator surfaces found by the  $U_c$ -match criterion, shown as white lines in Fig. 4.14, track very closely the hydrodynamic-acoustic transition of the  $U_{cp}$  maps. The smoothness of the  $U_c$ -match lines, and their proximity to the hydrodynamic/acoustic boundary in the field of  $U_{cp}$ , suggest that the  $U_c$  information on the OSPS is transmitted to the jet rotational/irrotational boundary. It is in fact quite remarkable that a highly distorted OSPS, such as that of jet ECC09U, yields a smooth radiator surface. This is even more apparent in the three-dimensional renderings of Fig. 4.16 which overlays the LES-derived OSPS with the radiator surface for jets AXI04U and ECC09U. The results provide encouragement that there is a surface, having the desired properties of the radiator surface, on which the RANS-derived convective velocity (on the OSPS) would inform the definition of the partial fields for noise source modeling.



(a) Jet AXI04U

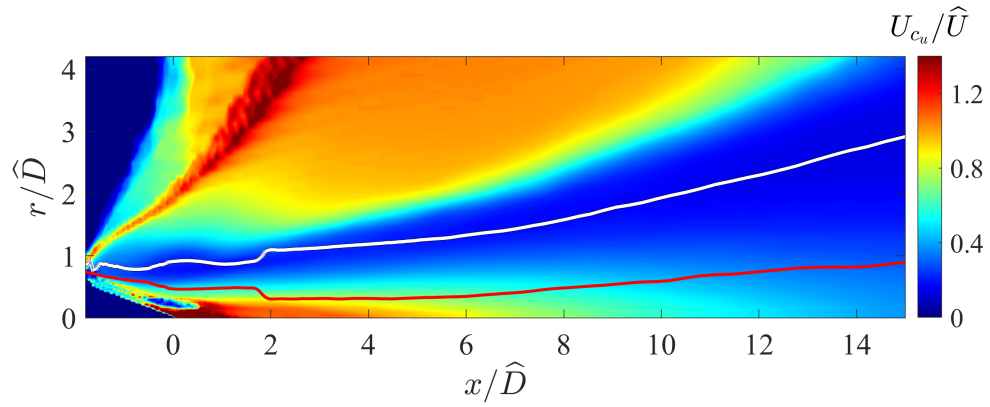


(b) Jet ECC09U at  $\phi = 0^\circ$ .

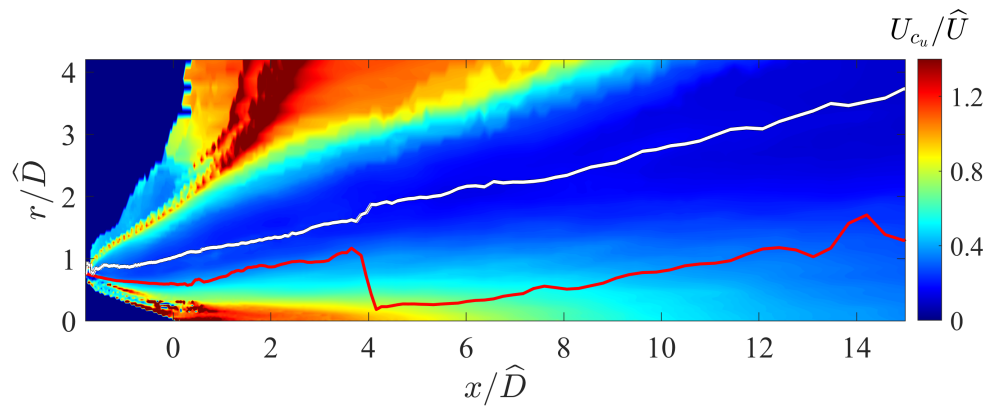


(c) Jet ECC09U at  $\phi = 180^\circ$ .

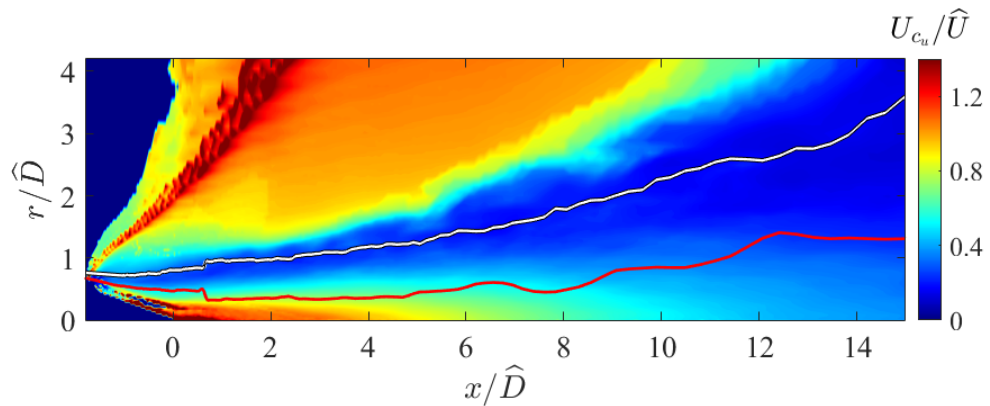
Figure 4.14: Distribution of normalized convective velocity  $U_{c_p}/\hat{U}$  as determined by space-time correlations based on  $p'$  on the meridional planes of jets AXI04U and ECC09U. White lines: radiator surface; red lines: OSPS based on LES.



(a) Jet AXI04U



(b) Jet ECC09U at  $\phi = 0^\circ$ .



(c) Jet ECC09U at  $\phi = 180^\circ$ .

Figure 4.15: Distribution of normalized convective velocity  $U_{cu}/\hat{U}$  on the meridional planes of jets AXI04U and ECC09U. The legend is the same as Fig. 4.14

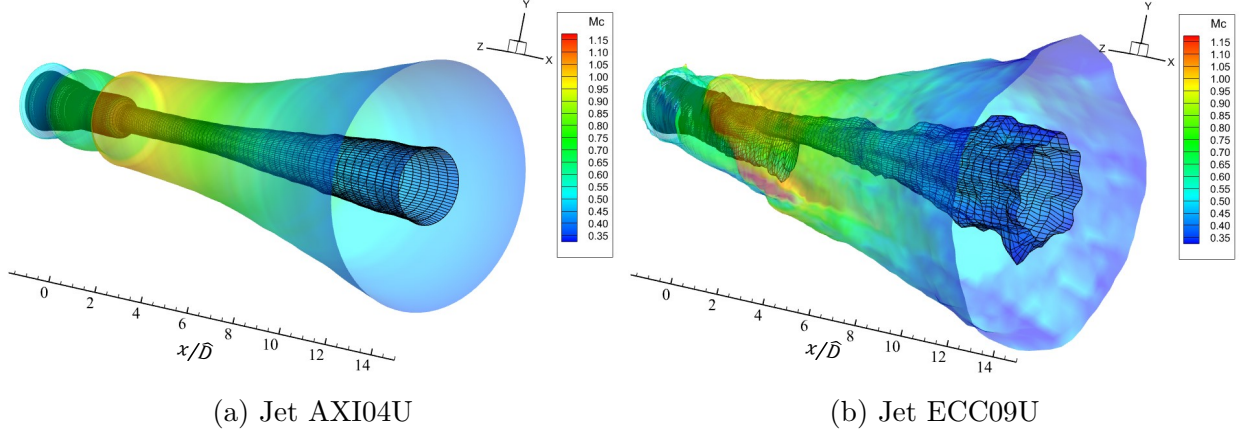


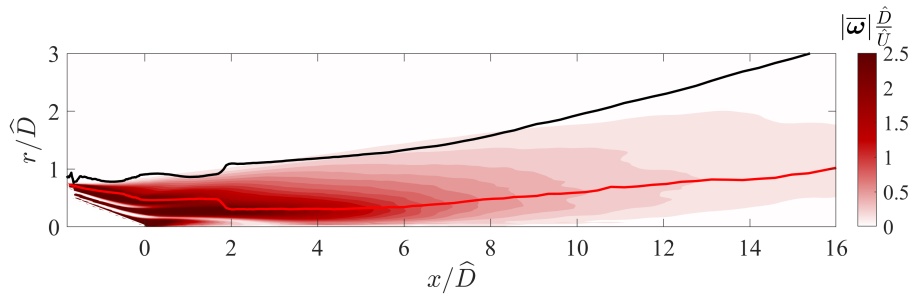
Figure 4.16: Radiator surfaces and LES-based OSPS with contours of convective Mach number  $M_c$ .

#### 4.4.2 Approximation Based on the Mean Flow

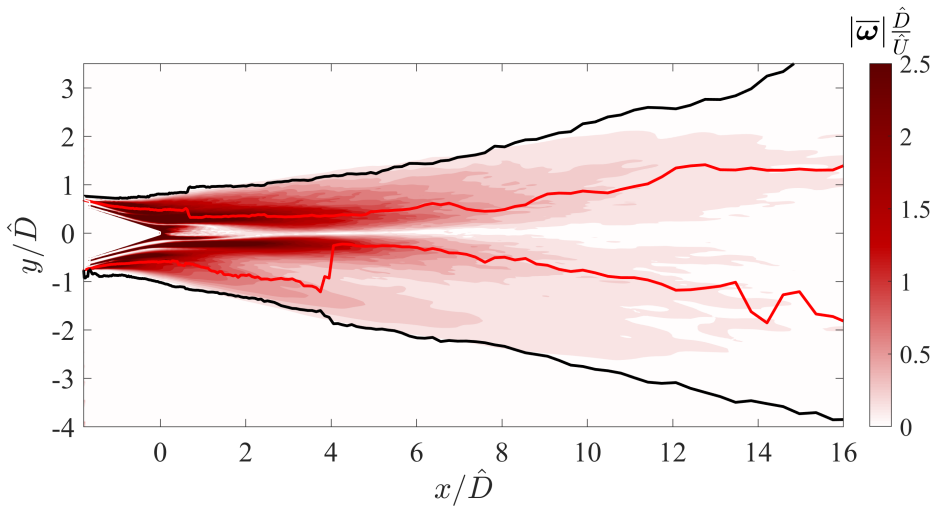
A predictive approach based on RANS alone would not have the benefit of the space-time correlations to locate the radiator surface. We thus search for a criterion based on the mean flow field that would yield an approximate representation of the radiator surface. The idea explained in Section 3.6.2 can be easily repeated in multi-stream jets, by which we search for a radiator surface based on the mean vorticity of the flow. Figure 4.17 plots isocontours of normalized mean vorticity magnitude  $|\overline{\omega}|\widehat{D}/\widehat{U}$  on the meridional planes of jets AXI04U and ECC09U. The magnitude has a wide dynamic range and reaches peak values of approximately  $|\overline{\omega}|\widehat{D}/\widehat{U} = 20$  in the shear layers near the nozzle exit. To accentuate the vorticity distribution near the jet edge, a smaller dynamic range has been applied so that the core vortical region appears saturated. The radiator surface is included in Fig. 4.17. Similarly to the single-stream jet, it is observed again that the radiator surface follows the outer edge of the mean vorticity field.

The criterion based on the local mean vorticity applied for single-stream jets of Eq. 3.13 is extended for asymmetric, multi-stream jets as

$$|\overline{\omega}|(x, r, \phi) = C_\omega |\overline{\omega}|_{\text{MAX}}(x, \phi), \quad r \geq r_{\text{OM}}(x, \phi) \quad (4.4)$$



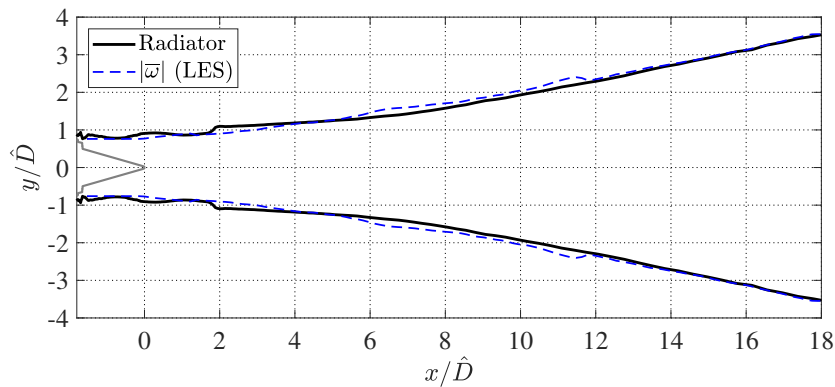
(a) Jet AXI04U.



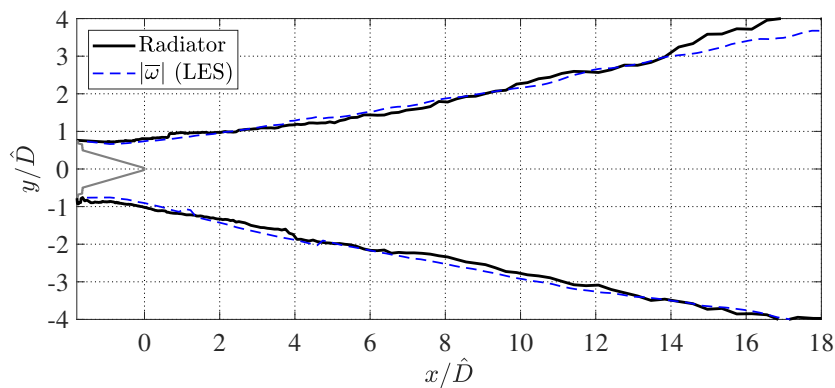
(b) Jet ECC09U.

Figure 4.17: Isocontours of normalized module of mean vorticity  $|\overline{\omega}| \hat{D} / \hat{U}$  on the meridional planes of jets AXI04U and ECC09U. Black line: radiator surface based on  $U_c$ -match criterion. Red line: OSPS

where  $|\bar{\omega}|_{\text{MAX}}$  is the outermost maximum of  $|\bar{\omega}|$  at a given axial and azimuthal location,  $r_{\text{OM}}$  is the radial location of this maximum. The search procedure for  $|\bar{\omega}|_{\text{MAX}}$  is similar to the detection of the OSPS exemplified in Fig. 4.8. Then, as Eq. 4.4 indicates, the threshold  $C_\omega$  is applied as one approaches the jet from the ambient towards the centerline. It was found that the threshold  $C_\omega = 0.125$  works satisfactorily for both jets of this study, as illustrated in Figs. 4.18 and 4.19. The figures demonstrate an excellent representation of the radiator surface using the criterion of Eq. 4.4 on the mean vorticity field as determined by LES correlations.



(a) Jet AXI04U



(b) Symmetry plane of jet ECC09U

Figure 4.18: Comparison of radiator surface with surface based on the mean vorticity criterion of Eq. 4.4 using the LES flow fields on the three stream jets.

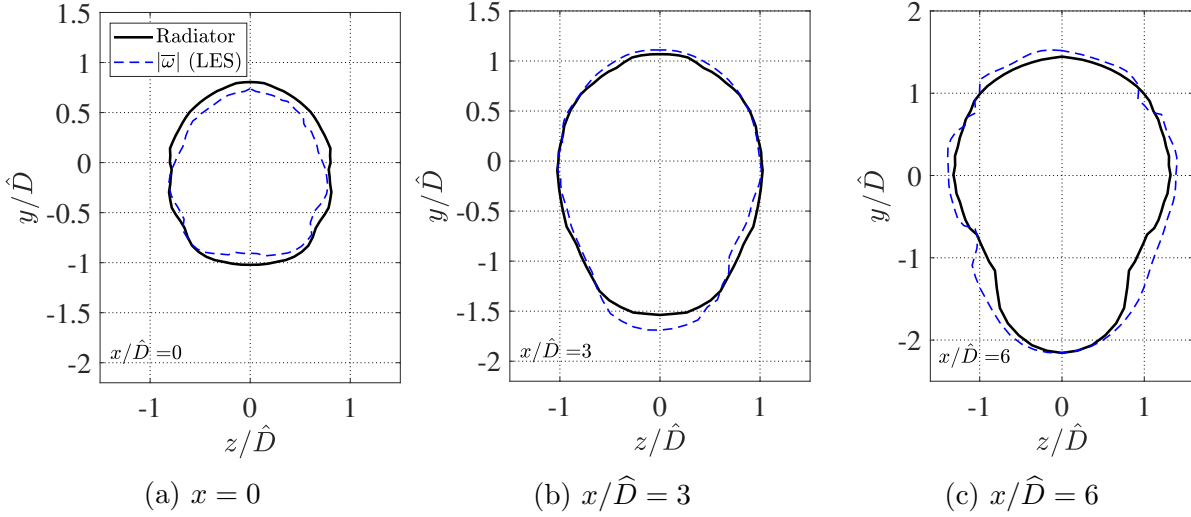
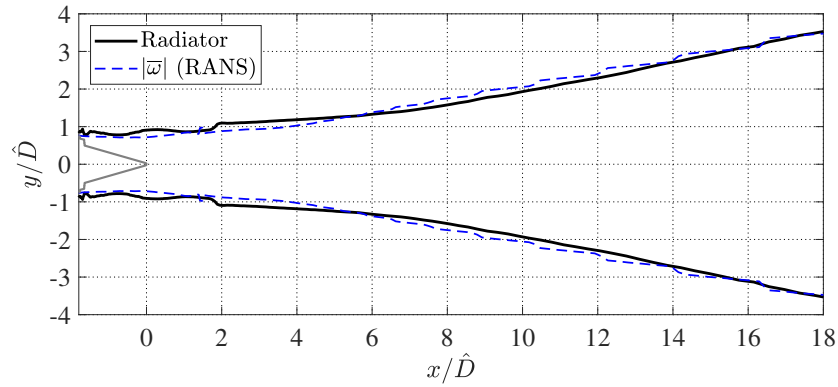


Figure 4.19: Comparison of radiator surface with surface based on the mean vorticity criterion of Eq. 4.4 using the LES flow fields on three cross-sectional planes of jet ECC09U.

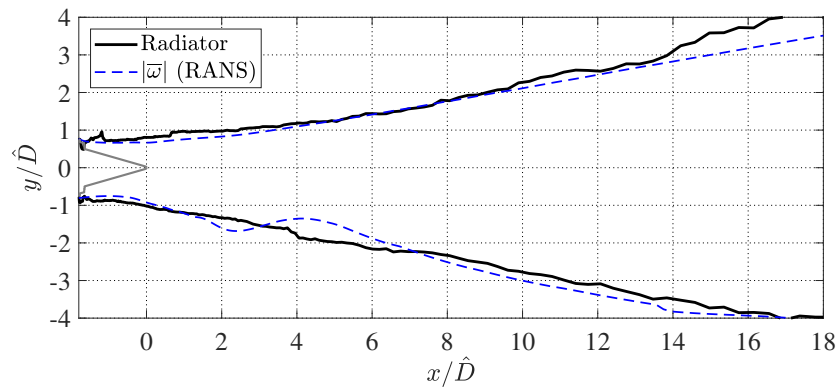
The above procedure can be repeated, for the same value of  $C_\omega = 0.125$ , using the RANS flow fields. The result is shown in Figs. 4.20 and 4.21. The RANS-based surfaces are very close to the radiator surfaces determined by the  $U_c$ -match criterion. Given the normal discrepancy between RANS and LES mean flow fields, these RANS-based surfaces are slightly less similar to the  $U_c$ -match surfaces than their LES-based counterparts in Figs. 4.18 and 4.19. Nevertheless, only jet ECC09U shows notable differences, with its RANS-based surface located moderately inwards from the radiator surface in Fig. 4.21. Overall, the surfaces obtained using Eq. 4.4 reproduce the geometry of the radiator surface with satisfactory accuracy. Even though this is based on only two multi-stream jets, it builds confidence that a RANS-based criterion for locating the radiator surface is achievable.

### 4.4.3 Flow Features Near the Jet Edge

To gain further insights as to the connection between events on the OSPS and their imprint on the radiator surface, it is convenient to examine statistics and instantaneous phenomena near the edge of the jet.



(a) Jet AXI04U



(b) Symmetry plane of jet ECC09U

Figure 4.20: Comparison of radiator surface with surface based on the mean vorticity criterion of Eq. 4.4 using the RANS flow fields on the three-stream jets.

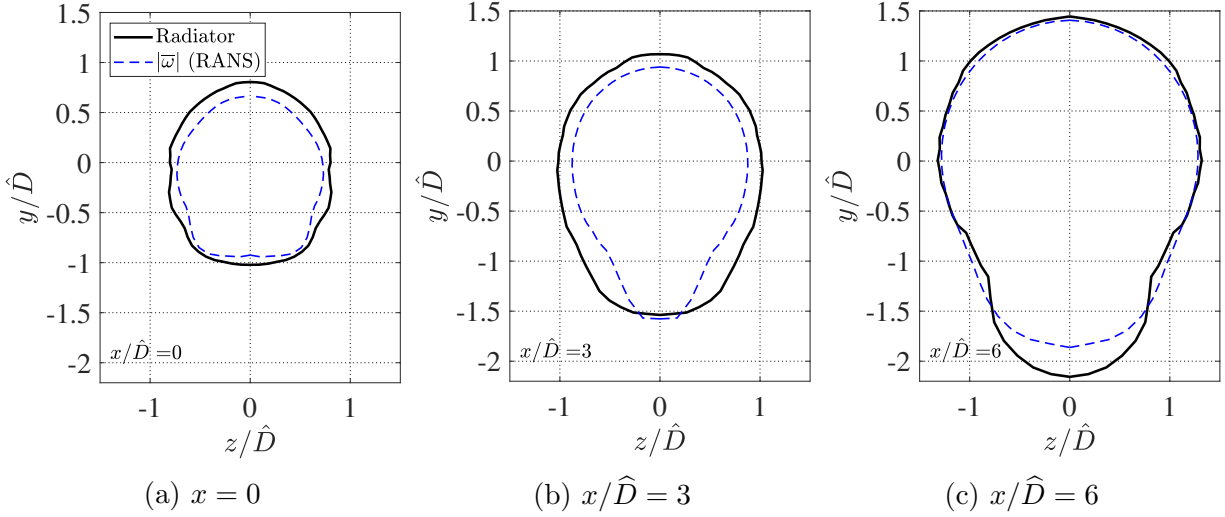


Figure 4.21: Comparison of radiator surface with surface based on the mean vorticity criterion of Eq. 4.4 using the RANS flow fields on three cross-sectional planes of jet ECC09U.

### Intensity of the Pressure Fluctuation

It is instructive to examine the effect of the eccentricity of the tertiary stream on the pressure distribution on the radiator surface. To this end, Fig. 4.22 plots the axial distribution of the root mean square of  $p'$ ,  $p'_{\text{rms}}$ , on the radiator surfaces of jets AXI04U and ECC09U at  $\phi = 0^\circ$  (downward direction). The eccentricity reduces the pressure level by factor of about two, which is consistent with the reduction in Reynolds stress seen when comparing Figs. 4.6(a) and 4.7(a).

The eccentricity of jet ECC09U also causes a notable difference between the  $p'_{\text{rms}}$  values at  $\phi = 0^\circ$  and  $\phi = 180^\circ$ , as shown in Fig. 4.23. At  $\phi = 180^\circ$ ,  $p'_{\text{rms}}$  forms a clear, continuous lobe, and the SPS follows closely its locus. In contrast,  $p'_{\text{rms}}$  acquires much lower values at  $\phi = 0^\circ$ . The reduction in  $p'_{\text{rms}}$  observed at  $\phi = 0^\circ$  in Figs. 4.22 and Fig. 4.23, and the decline in radiation efficiency due to the lower convective Mach number, are factors that contribute to the reduction in far-field sound pressure level seen in Fig. 4.2.

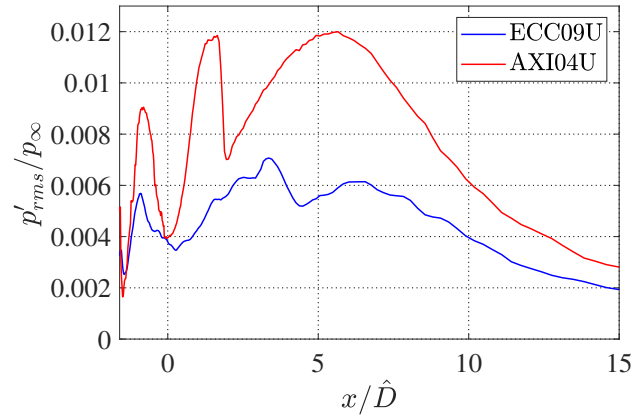


Figure 4.22: Distribution of  $p'_{rms}$ , normalized by the ambient pressure  $p_\infty$ , on the radiator surfaces of jets AXI04U and ECC09U at  $\phi = 0^\circ$ .

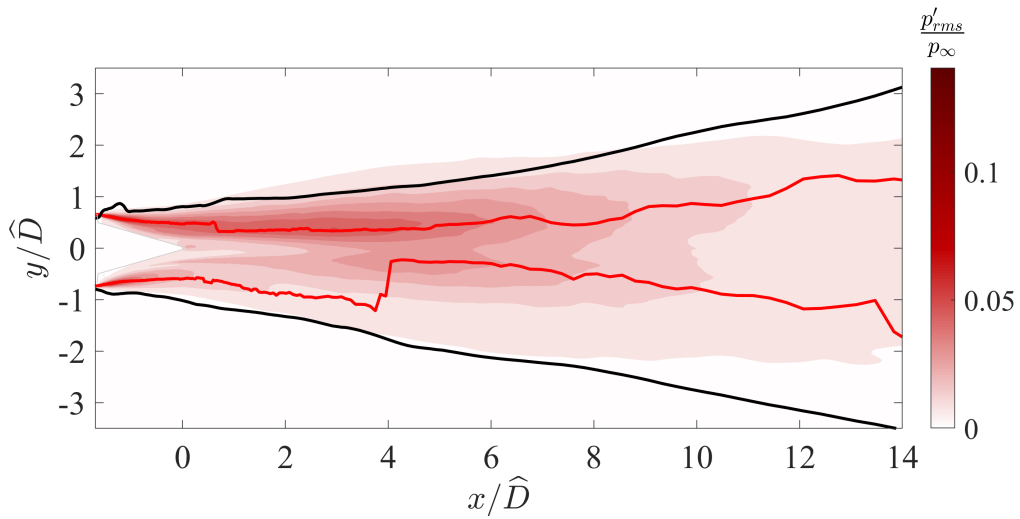


Figure 4.23: Distribution of the root mean square of pressure fluctuation on the symmetry plane of jet ECC09U. Black line: radiator surface. Red line: OSPS.

## Skewness of the Pressure Fluctuation

Skewness is a statistical measure of the asymmetry of the distribution of a variable. The skewness of pressure fluctuation  $p'$  is defined as

$$Sk_p = \frac{\overline{p'^3}}{\overline{p'^2}^{3/2}} \quad (4.5)$$

The same formula can be applied to any zero-mean signal, such as  $u'$ , to get  $Sk_u$ . The skewness of the pressure fluctuation,  $Sk_p$ , is often used to analyze the near field of jets in the study of shock formation [42], which deal with positive values of pressure skewness well into the acoustic region. However, an intriguing finding of experimental studies on the near pressure field of single- and dual-stream jets by Papamoschou and Phong [79] is the existence of a layer of negative skewness near the edge of the jet. This layer has also been observed in LES of supersonic single-stream jets [28, 88], as well as LES of jet AXI04U [2]. Therefore, this seems to be an inherent feature of turbulent jets, at least in the high-speed regime. In addition, in Ref. [79] it was noted that the RANS-based radiator surface, defined according to a criterion based on the gradient of mean axial velocity, was close to the locus of  $Sk_p \approx -0.3$ . All this motivates the decision to study the pressure skewness distribution of the jets of this work, and how the radiator surface and the negative skewness layer might be related.

Figure 4.24 plots isocontours of  $Sk_p$  for the three-stream jets of this study and includes the locations of the radiator surface. The plot for AXI04U of Fig. 4.24a is averaged in the azimuthal direction and therefore is smoother than the plot for ECC09U of Fig. 4.24b. Several regions of low skewness appear at the early stages of the jets, which are likely due to the interactions between shear layers and their surrounding ambient. Outer layers of strongly negative skewness are visible near the edge of the jets. The radiator surfaces, drawn as white lines, are very close or inside those layers.

It is difficult to draw conclusions based on the exact values of skewness of the jets of this study. The skewness, being a third power of a fluctuating signal, requires extensive simulation time to converge on reliable values. We briefly look at jet AXI04U in Fig. 4.24a, which is determined from more time steps and is averaged in the azimuthal direction. Its outer layer of negative  $Sk_p$  fluctuates between radial minima of  $Sk_p = -0.4$  and  $-0.7$  until  $x/\hat{D} = 6$ . After this point, the layer acquires increasingly low values. Given that the downstream regions of the flow take longer times to converge, it is likely that those very low values of  $Sk_p$  are transitory and lack simulation time.

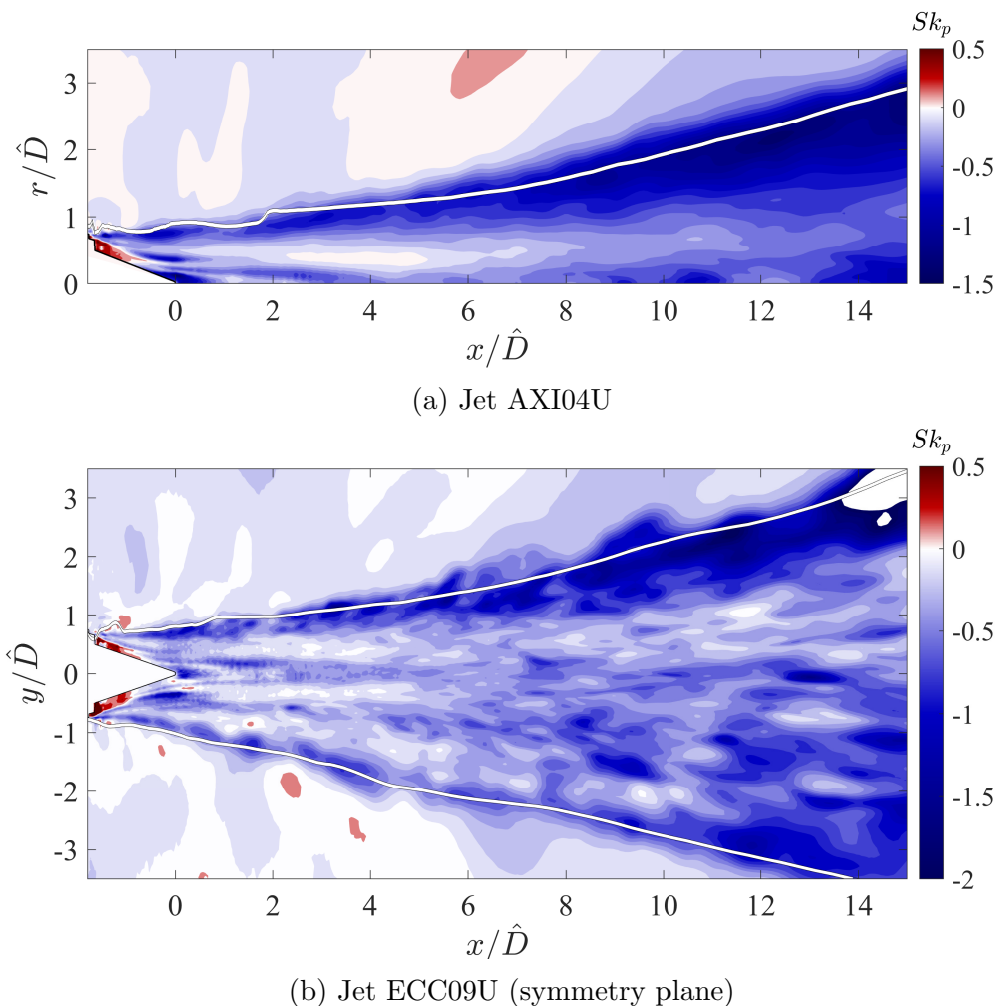


Figure 4.24: Distribution of the normalized skewness of the LES pressure field. White lines: radiator surface.

## Instantaneous Pressure Fluctuation

The natural procedure to investigate the origin of the layer of negative skewness of pressure is to study the time evolution of pressure in the vicinity of the radiator surface. Using jet AXI04U as a reference, a sample point for the study is selected to be  $x/\hat{D} = 6.0$  and  $\phi = 0^\circ$ , a location where where  $Sk_p = -0.75$  (Fig. 4.24(a)). A short segment of this evolution is plotted in Fig. 4.25, where  $p'$  is normalized by  $p'_{\text{rms,max}}$ , the maximum rms pressure fluctuation on the plane  $\phi = 0^\circ$ . Two strong negative peaks at  $t\hat{U}/\hat{D} = 25$  and  $t\hat{U}/\hat{D} = 30$  stand out over the rest of the signal, which is mostly contained within  $-0.3 < p'/p_{\text{rms,max}} < 0.3$ . The rms pressure fluctuation at this point of the radiator surface is  $p'_{\text{rms}}/p_{\text{rms,max}} = 0.13$ , so those pressure drops are more than three times the standard deviation of the pressure fluctuation. It is surmised that events like this sudden expansion contribute to the negative skewness.

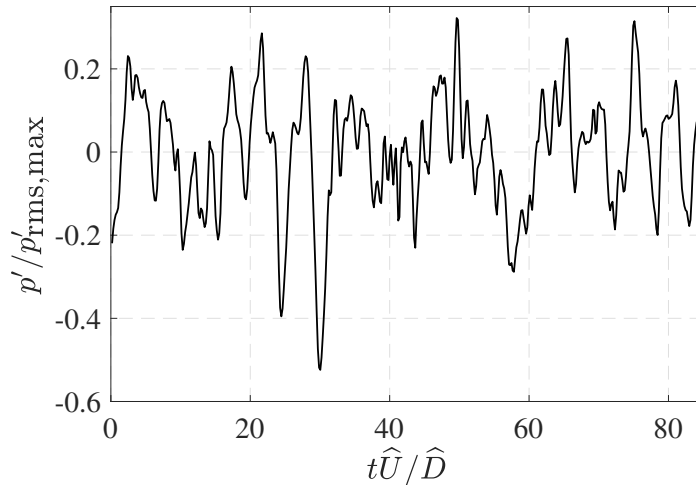


Figure 4.25: Pressure time history on the radiator surface of jet AXI04U at  $x/\hat{D} = 6$  and  $\phi = 0^\circ$ .

Figure 4.26 shows the contour of instantaneous pressure fluctuation at the times of the sudden drops noted in Fig. 4.25. We can see that the cause of the intense negative peaks are localized pressure drops near the radiator surface at  $x/D_j = 6$ . The arrows in Fig. 4.26

denote the projection of the instantaneous velocity fluctuation vector on the plane  $\phi = 0^\circ$  and help identify these events as vortices rotating counter-clockwise. These vortices travel at slow speeds compared to the inner turbulence. The vortex affecting  $x/D_j = 6$  at  $t\hat{U}/\hat{D} = 25$  (Fig. 4.26a) can be seen in Fig. 4.26b near the radiator surface at  $x/D_j = 6.8$ , yielding a convective velocity of that particular vortex of  $0.14\hat{U}$ , which is lower than the convective velocity based on correlations of the pressure fluctuation of that point (see Fig. 4.14).

It is evident from Fig. 4.26 that the pressure drops of Fig. 4.25 are connected to vortex cores. Analogous analysis other points near the radiator surface show similar events associated with negative pressure spikes. These observations suggest that the edge of the jet is affected by sparse vortices peeling off from the flow eddies and drifting towards the radiator surface. Their effects are imprinted as layers of negative pressure skewness. These events constitute the last remnants of the vortical field and vanish outside the radiator surface.

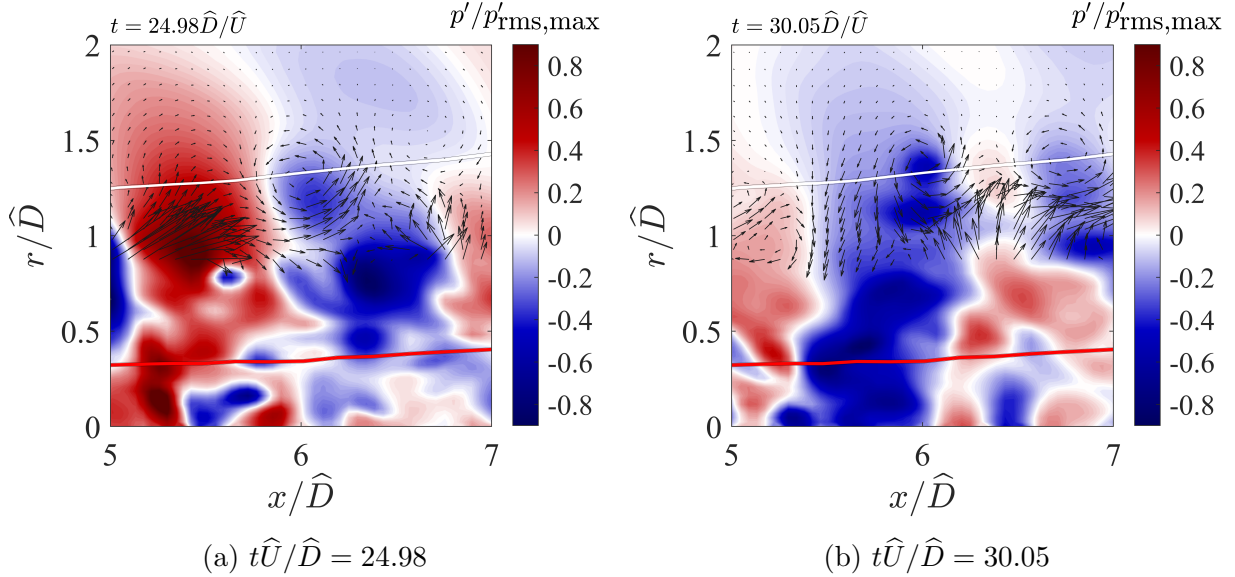


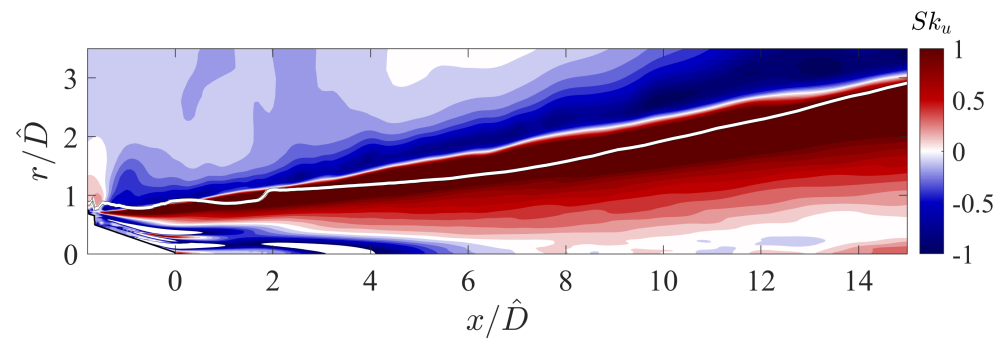
Figure 4.26: Contour of the instantaneous pressure fluctuation in jet AXI04U at  $\phi = 0^\circ$ . Arrows: projection of velocity fluctuation vectors on  $x-y$  plane; white line: radiator surface; red line: OSPS surface.

## Skewness of Axial Velocity Fluctuation

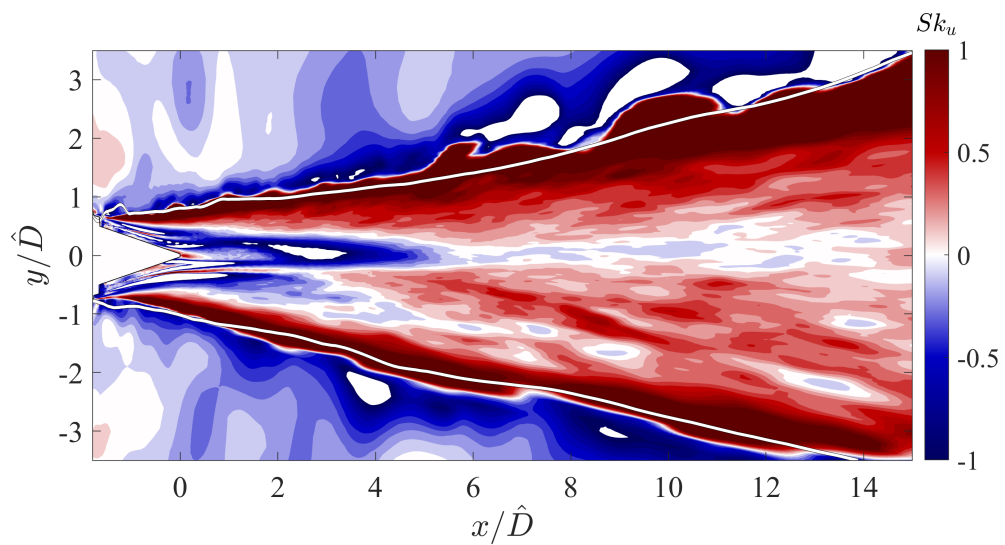
Analysis of the instantaneous pressure and velocity fields revealed that sparse vortices peeling off from the main flow cause a negative layer of skewness near the edge of the jet. Given the influence of those vortices on the skewness of the pressure fluctuation, it is interesting to study the analogous skewness of the axial velocity fluctuation,  $Sk_u$ , which is plotted in Fig. 4.27. The results for jet AXI04U, shown in Fig. 4.27a, have been averaged in the azimuthal direction, and the results for jet ECC09U in Fig. 4.27b are of its symmetry plane. In both cases, there are clear double layers of positive and negative skewness near the edge of the jets. The shape of the double layers, with the positive part underneath the negative one, are consistent with the footprint of rotational events in the same direction of those shown in Fig. 4.26. In the right-handed cylindrical coordinate system  $(x, r, \phi)$ , that rotation is towards positive  $\phi$ .

## Connection Between Pressure and Vorticity Fields

The connection between the sparse vortical events and the pressure drops that cause negative skewness of pressure can be quantified by the correlation between azimuthal vorticity fluctuation  $\omega'_\phi$  and pressure fluctuation  $p'$ , expressed as  $R_{\omega_\phi p}$  by Eq. 4.2 for zero time displacement  $\tau$ . There are evident layers of negative correlations near the edge of the jet, of values between -0.25 and -0.5. Apart from a difference in contour levels, the distributions of  $R_{\omega_\phi p}$  in Fig. 4.28 are remarkably similar to those of  $Sk_p$  in Fig. 4.24. These results confirm that the pressure drops are consistently caused by vortices peeling off from the main flow and traveling near the radiator surface. Additionally, the negative sign of  $R_{\omega_\phi p}$  indicates that negative pressure events are linked to events of positive  $\omega_\phi$ , just as it is shown in Figs. 4.26 and 4.27. The analysis of the events near the edge of the jet is presented here for the



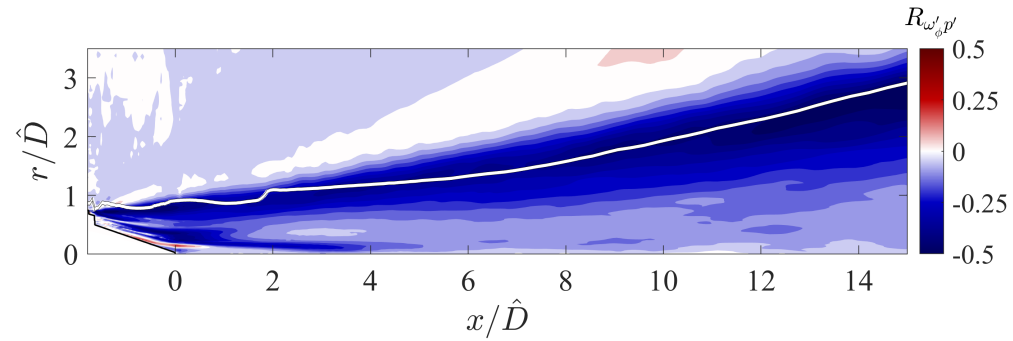
(a) Jet AXI04U



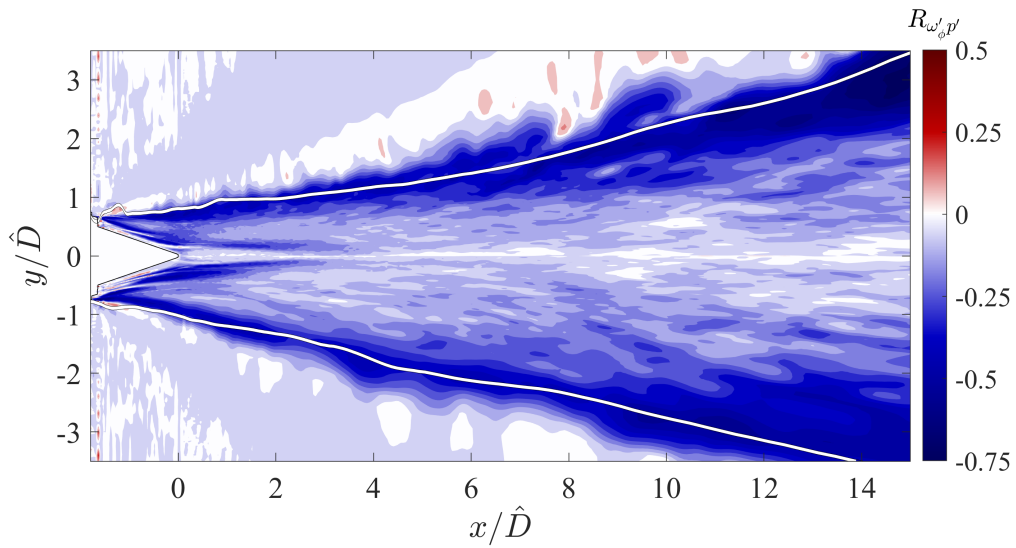
(b) Jet ECC09U (symmetry plane)

Figure 4.27: Distribution of the normalized skewness of the LES axial velocity field. White lines: radiator surface.

three-stream jets. It can be easily reproduced for the single-stream jet, as shown in Annex B, with consistent results.



(a) Jet AXI04U



(b) Jet ECC09U (symmetry plane)

Figure 4.28: Distribution of normalized correlation between  $\omega'_\phi$  and  $p'$ ,  $R_{\omega_\phi p}$ . White lines: radiator surface.

## 4.5 Longitudinal Correlations

### 4.5.1 2D Space-Time Correlations

The connection between the inner vortical field and the edge of the jet is further investigated using two-dimensional space-time correlations of the LES data. The focus is on the interaction between turbulent eddies near the inner (high-speed) shear layer and the rest of the domain, with emphasis on events near the radiator surface. For the reasons given in Section 4.4, we consider the correlation  $R_{up}$  between  $u'$  in the high-speed turbulent region and  $p'$  elsewhere. The formulation of Eq. 4.2 is used with reference point  $\mathbf{x}_0 = (x_0, r_0, 0)$  and displaced point  $\mathbf{x} = (x, r, 0)$ .

On the meridional plane  $\phi = 0^\circ$ , the reference point is placed at  $(x_0, r_0) = (2.0, 0.3)\hat{D}$ . This point is on the OSPS of jet AXI04U and near the middle of the high-speed shear layer of jet ECC09U. The resulting space-time correlation  $\hat{R}_{up}$  is plotted in Fig. 4.29 for jets AXI04U and ECC09U at three time separations. The evolution of  $\hat{R}_{up}$  for AXI04U shows two main lobes of opposite signs traveling downstream at a speed slightly faster than  $0.6\hat{U}$ . At zero time separation ( $\tau=0$ ), the lobes show a strong correlation pattern radiating from the vortical region to the radiator surface and then on to the near acoustic field. For non-zero time separations ( $\tau = \pm 1.92\hat{D}/\hat{U}$ ), the correlations remain strong in the near acoustic field but weaken inside the vortical region. The correlation peaks near the radiator surface represent the footprint of large turbulent structures that pass through the reference point and dominate the surrounding linear field [32]. However, inside the vortical field those large eddies coexist with smaller scales that become uncorrelated quickly and thus decrease the values of two-point correlations for  $\tau \neq 0$ . The fact that the peaks of correlation linked to the linear field follow well the location of the radiator surface is further confirmation of its appropriate placement in Section 4.4.

In comparison with jet AXI04U, jet ECC09U shows much lower values of correlations at all time separations. At zero time separation, the peak correlation of ECC09U in the near acoustic field is  $R_{up} = -0.13$  versus  $R_{up} = -0.21$  for AXI04U. At non-zero time separation, the correlations for ECC09U become even weaker. The thickened low-speed flow of jet ECC09U not only suppresses the turbulence level of the inner shear layer, as evidenced in Fig. 4.7, but also weakens the correlation between the inner shear layer and the emitted acoustic field. The reduced correlation can be attributed to the lower radiation efficiency of the eddies in the inner shear layer.

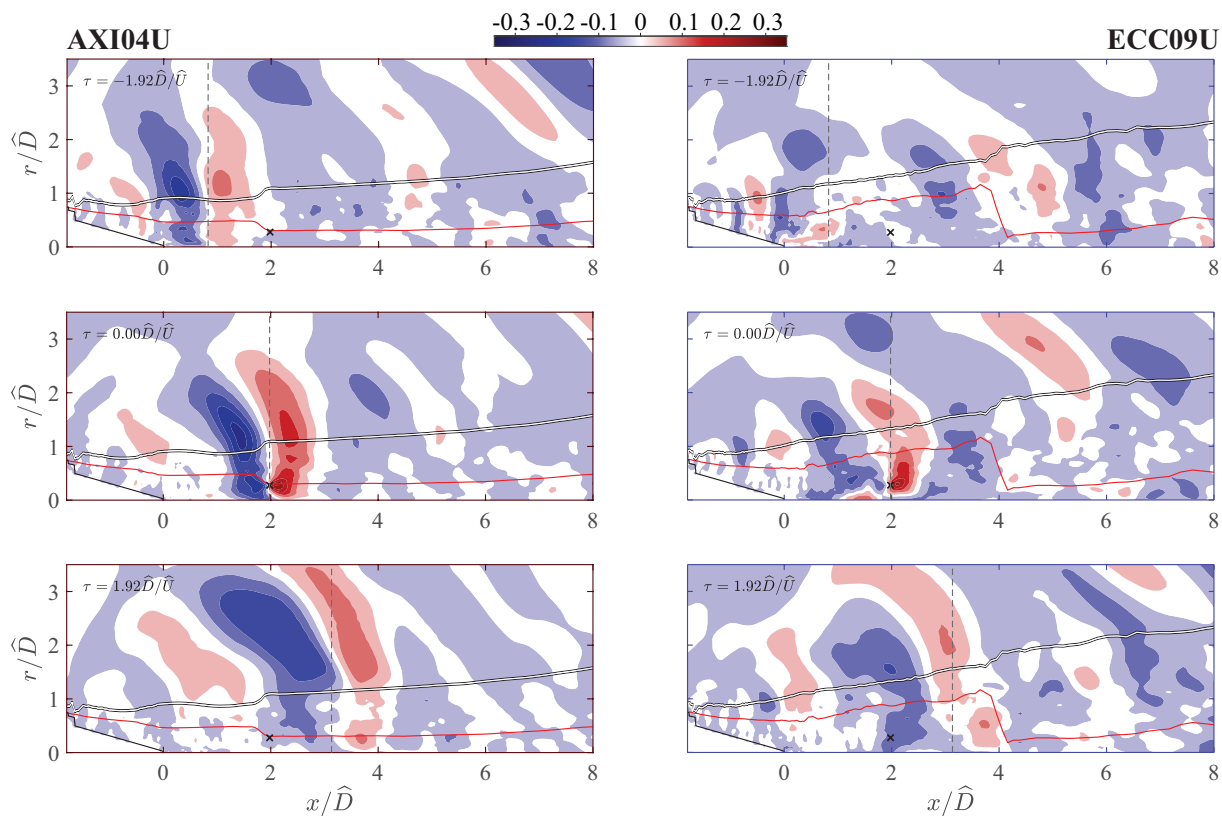


Figure 4.29: Contours of  $R_{up}$  with reference point  $(x_0, r_0) = (2, 0.3)\hat{D}$  for jets AXI04U (left column) and ECC09U (right column) at azimuthal angle  $\phi = 0^\circ$ . Time separations:  $\tau = -1.92\hat{D}/\hat{U}$  (top row),  $\tau = 0$  (middle row), and  $\tau = 1.92\hat{D}/\hat{U}$  (bottom row). Red line: SPS. White line: radiator surface. Black dashed vertical line: positions for a downstream convection at velocity  $0.6\hat{U}$ .

## 4.5.2 Longitudinal Length Scales

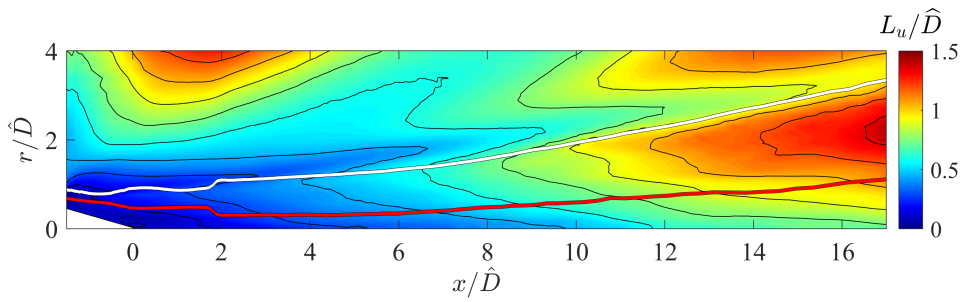
The definition of fixed- and moving-frame length scales defined in section 3.2 for the single-stream jet can be directly applied for the three-stream jets. This section presents the distributions of length scales based on axial velocity fluctuation and pressure fluctuation of jets AXI04U and ECC09U. For brevity, the results for jet ECC09U are only shown at  $\phi = 0^\circ$ . In order to improve the convergence and visualization of results, the results of jet AXI04U have been averaged in the azimuthal direction, and those of jet ECC09U have been averaged on a  $20^\circ$  span centered on  $\phi = 0^\circ$ . It should be noted that the initial flow region near the jet exit, which presents multiple shear layers at short distances from each other, is too intricate for this study and has been left out of the commentary. If such analysis were to be carried out, the researches should place careful consideration to the distance of the displacements  $\xi$  of the space-time correlations, and set them in a correct angle that follows the flow direction.

### Fixed-Frame Length Scales

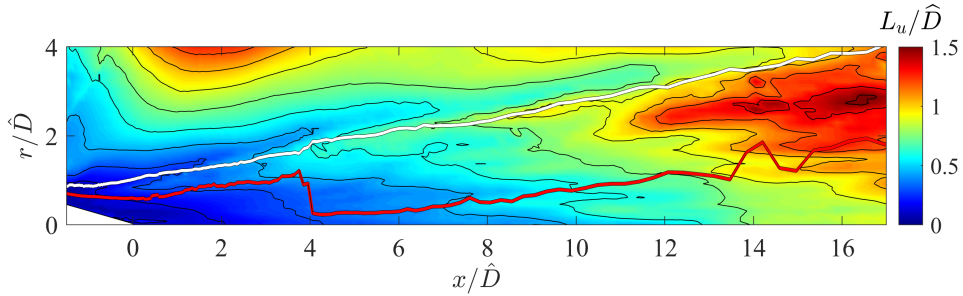
Figure 4.30 presents isocontours of normalized fixed-frame length scales based on axial velocity fluctuation,  $L_u/\widehat{D}$ , on jets AXI04U and ECC09U. There are evident similarities of these distributions to the single-stream results of Section 3.4.2, which suggest that there are similar physical mechanisms at play. Starting from the jet exit, the scales  $L_u$  grow axially following the growth of the jet itself. Regarding their radial variation, going radially outwards from the jet centerline, the scales  $L_u$  form a local maximum, then decrease to a local minimum near the edge of the jet, and then rise to higher values.

The main qualitative difference of the distributions of  $L_u$  of the three-stream jets in Fig. 4.30 with respect to the single-stream jet in Fig. 3.16 is the location of the radiator surface. In the single-stream jet, the radiator surface closely follows the radial minima near the edge of the jet, which is associated with a loss of coherence of velocity-based events. In

the three-stream jets, the radiator surface is located between the radial maxima and this “valley” of low correlation. For jet ECC09U in Fig. 4.30b, the radiator surface is very close to the radial maxima until  $x/\hat{D} = 11$ . The reason for this discrepancy is not well understood at this time, but it may be due to the fact that the space-time correlations for the three-stream jets use horizontal stencils for the whole flow field, and this method may introduce inaccuracies at the jet boundary. Nevertheless, the radiator surface is close to the layer of low correlation, and the observations made in Section 3.4.2 are still applicable for these jets.



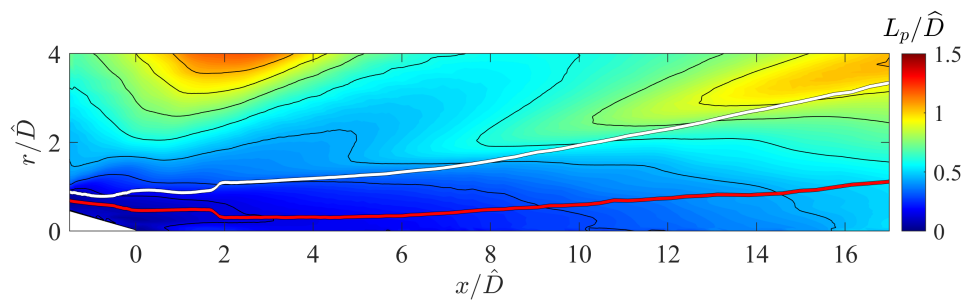
(a) Jet AXI04U



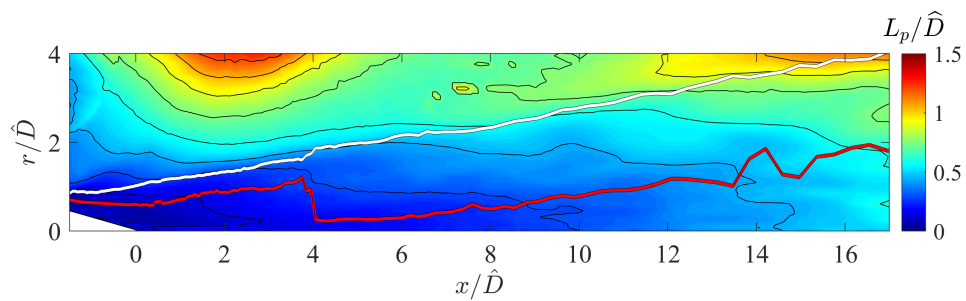
(b) Jet ECC09U,  $\phi = 0^\circ$

Figure 4.30: Isocontours of normalized fixed-frame length scales based on axial velocity fluctuation,  $L_u/\hat{D}$ . Red line: OSPS. White line: radiator surface.

The distribution of normalized fixed-frame length scaled based on pressure fluctuation,  $L_p/\hat{D}$ , for jets AXI04U and ECC09U are presented in Fig. 4.31. As with the velocity-based scales, we can note a reasonable similarity of these distributions to the single-stream results for  $L_p$  presented in Section 3.4.2. Inside the vortical regions of the three-stream jets,  $L_p$  increases radially and reaches high levels outside the radiator surface.



(a) Jet AXI04U



(b) Jet ECC09U,  $\phi = 0^\circ$

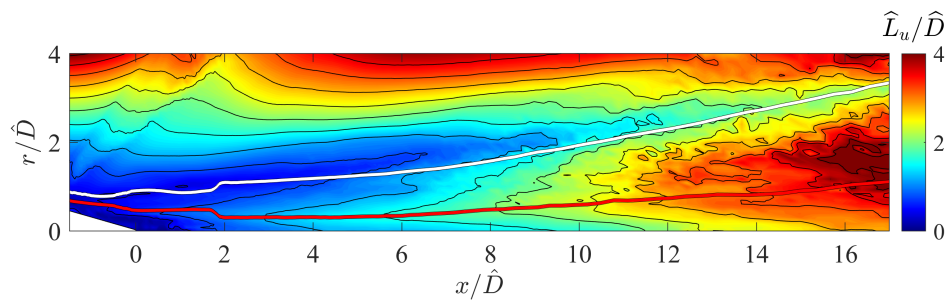
Figure 4.31: Isocontours of normalized fixed-frame length scales based on pressure fluctuation,  $L_p/\hat{D}$ . Red line: OSPS. White line: radiator surface.

It is interesting to note the similarity of the trends obtained from jets AXI04U and ECC09U for both types of scales  $L_u$  and  $L_p$ . The asymmetry of ECC09U, with a thicker tertiary stream at  $\phi = 0^\circ$ , causes a wider spreading of the flow at this angle compared to jet AXI04U. That difference is seen in the location of the radiator surface and the quantitative values of length scales, but the trends remain consistent. This fact is encouraging for the low-cost modeling of noise generation of multi-stream jets, as it suggests that the variation of turbulence scales of a given asymmetric jet can be inferred from the study of a similar, reference jet.

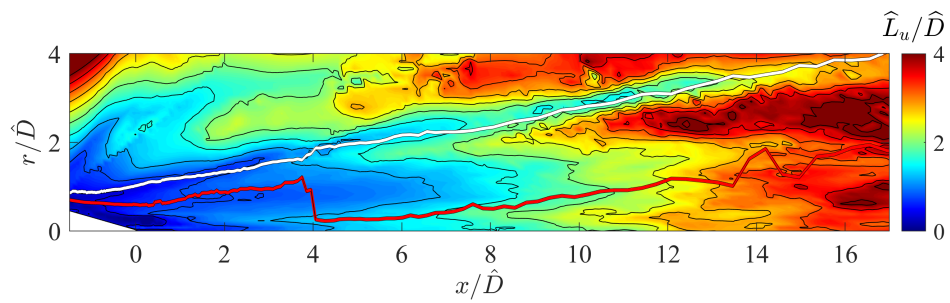
### Moving-Frame Length Scales

The distributions of normalized moving-frame length scales based on axial velocity fluctuation,  $\widehat{L}_u/\widehat{D}$  are presented in Fig. 4.32. The analogous scales based on pressure fluctuation  $\widehat{L}_p/\widehat{D}$  are presented in Fig. 4.33.

The distributions of  $\widehat{L}_u$  and  $\widehat{L}_p$ , shown in Figs. 4.32a and 4.33a respectively, show remarkable resemblance to the single-stream  $\widehat{L}$  distributions in Fig. 3.20 of Section 3.4.3. As with the fixed-frame length scales, it is reasonable to assume that jet AXI04U contains similar physical phenomena as the single-stream jet, and the same physical explanations of Section 3.20 are applicable here. Jet ECC09U has somewhat similar trends to jet AXI04U, with the exception of a layer of radial maxima just below the radiator surface in both of the contours of  $\widehat{L}_u$  and  $\widehat{L}_p$ . A possible explanation for this region of high scales is that as jet ECC09U introduces a tertiary shear layer that diverges and does not mix with the other two shear layers (see Fig. 4.7), it creates a region of turbulence eddies that are somewhat disconnected from the main turbulent region, as shown in Fig. 4.29. These turbulence structures are not necessarily large, as they do not induce large values in fixed-frame scales  $L$ . Instead, their disconnection from the main turbulent region causes a slower breakdown process, an increase in their time scales, and consequently large values of  $\widehat{L}$ .

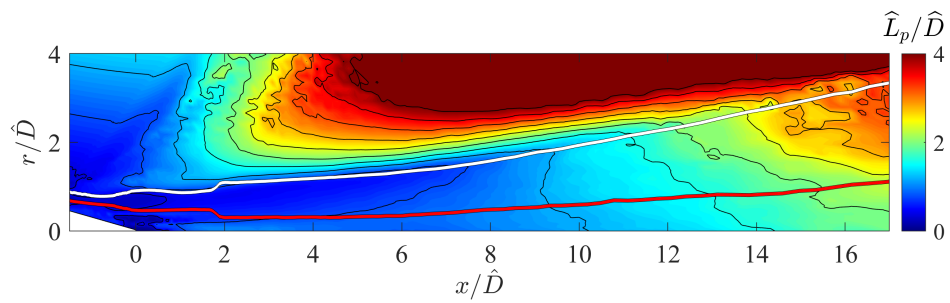


(a) Jet AXI04U

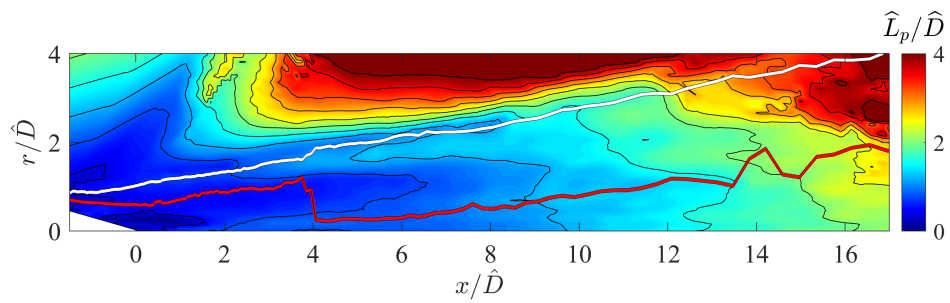


(b) Jet ECC09U,  $\phi = 0^\circ$

Figure 4.32: Isocontours of normalized moving-frame length scales based on axial velocity fluctuation,  $\hat{L}_u/\hat{D}$ . Red line: OSPS. White line: radiator surface.



(a) Jet AXI04U



(b) Jet ECC09U,  $\phi = 0^\circ$

Figure 4.33: Isocontours of normalized moving-frame length scales based on pressure fluctuation,  $\hat{L}_p/\hat{D}$ . Red line: OSPS. White line: radiator surface.

## Modeling Based on RANS Flow Field

Efforts on the single-stream jet presented earlier on Chapter 3 suggested that the scales at the jet vary following somewhat consistent trends, so the scales at the edge of the jet can be inferred from the inner vortical field. In addition, the modeling study in Section 3.6 indicated that time-averaged flows give good trends to model the scales at the radiator surface after being adjusted by a proportionality constant. Here we study the extension of those conclusions to the three-stream jets of this work. Again, we ask two questions for each variable and jet: A) Are the scales in the vortical flow field, studied on the OSPS, easily connected to those on the radiator surface?, and B) If so, can the scales on the OSPS be modeled from RANS flow fields?

Figure 4.34 plots the distributions of  $L_p$  on the radiator surface,  $L_u$  on the OSPS, and RANS-based length scales for jets AXI04U and ECC09U. The distribution of  $L_u$  has been adjusted by a proportionality factor  $C$  to match the  $L_p$  variation. The RANS-based scales are calculated through Eq. 3.10, repeated here for clarity,

$$L = C_L \frac{k^{3/2}}{\epsilon} \quad (3.10 \text{ revisited})$$

where  $C_L$  has also been adjusted to match the variation of  $L_p$  on the radiator surface.

The trends of  $L_p$  and  $L_u$  display fairly linear growth for jet AXI04U, presented in Fig. 4.34a. The distribution of RANS-based scales starts a trend of linear growth, but it is notably affected by the collapse of the OSPS from the outer to the inner shear layers (see Fig. 4.11) and experiences a sudden drop. After that, the trend increases fairly linearly but at a faster rate than the other two curves.

The variation of  $L_p$  on jet ECC09U plotted in Fig. 4.34b is fairly linear, but the scales distributions on the OSPS are affected by its strong collapse (see Fig. 4.12). The curve

of  $L_u$  on the OSPS experiences a drop at  $x/\widehat{D} = 4$  from 0.5 to 0.3, while the curve for RANS-based scales shows a bigger drop at  $x\widehat{D} = 5$ . The general trends of  $L_p$  at the radiator and  $L_u$  on the OSPS are similar after the latter being adjusted by the proportionality factor  $C$ . However, the RANS-based scales show, as is the case with jet AXI04U, different trends before and after the collapse of the OSPS which would suggest the need for two different proportionality adjustments.

One interesting aspect of the comparisons of Figs. 4.34 is the consistency of the proportionality factors between jets AXI04U and ECC09U. The factor  $C$  to fit  $L_u$  on the OSPS to  $L_p$  on the radiator surface is 0.94 and 1.03 respectively, and the RANS-based scales are fitted through  $C_L = 0.62$  and 0.70. These results suggest that modifications on the jets and their turbulence fields have a consistent effect on their time-averaged flow field, and are encouraging for their RANS-based modeling.

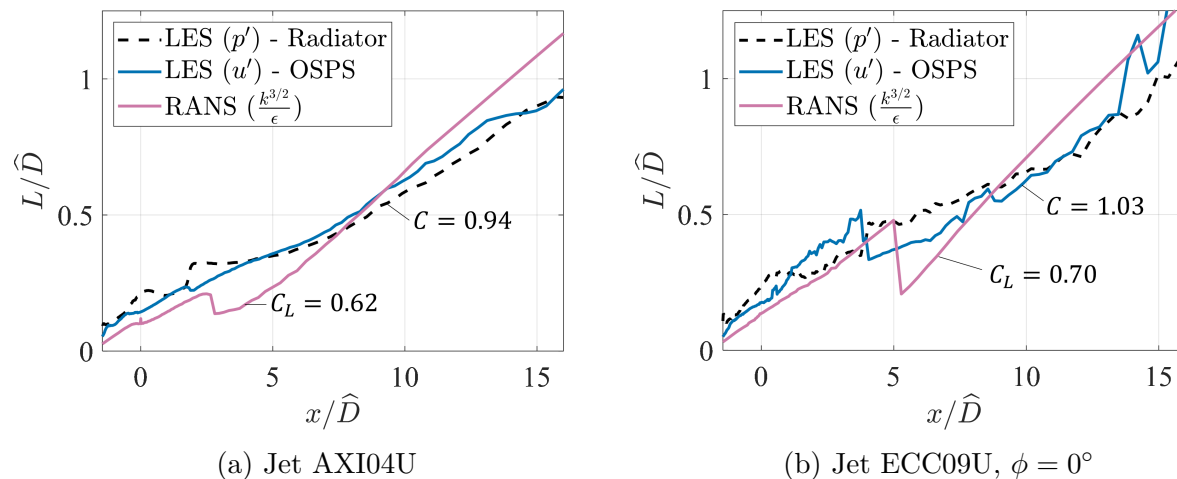


Figure 4.34: Fitting of  $L_u$  on the OSPS and RANS-based length scales to the  $L_p$  distribution on the radiator surface.

The analogous plots of the moving-frame length scales  $\widehat{L}$  are plotted in Fig. 4.35, with a modification on the calculation of RANS-based scales. These RANS-based scales, as calculated from Eq. 3.10, have already been shown in Fig. 4.34 and seem to be affected by the OSPS geometry more than the LES-based moving-frame scales. We take the opportunity to

test another way of modeling the moving-frame length scales as a product of a time scale and a velocity scale. The time scale is taken from RANS dimensional analysis as  $k/\epsilon$  and the velocity scale is simply the mean axial velocity on the OSPS, so the modeled  $\widehat{L}$  is

$$\widehat{L} = C_{\widehat{L}} \frac{k}{\epsilon} \bar{u}(r = r_{OSPS}) \quad (4.6)$$

The trend of  $\widehat{L}_p$  on the radiator surface of jets AXI04U in Fig. 4.35a is more complex than that of fixed-frame length scales, as was the case with the single-stream jet in Section 3.4.3. These scales experience an initial rapid growth, followed by a plateau, and then they grow again. The initial shape of  $\widehat{L}_p$  is jumpy up to  $x/\widehat{D} = 2$  due to the geometry of the radiator surface, which is affected by the initial changes in convective velocity at the OSPS. In contrast, the other two distributions of  $\widehat{L}_u$  on the LES-based OSPS and the RANS-based  $\widehat{L}$  exhibit fairly linear trends and match well one another.

Figure 4.35b plots the corresponding distributions of  $\widehat{L}$  for jet ECC09U. There, the distribution of  $\widehat{L}_p$  on the radiator surface is approximately linear until  $x/\widehat{D} = 8$ , where it increases its growth rate. The other two curves,  $\widehat{L}_p$  and RANS-based  $\widehat{L}$ , are fairly linear and show a good match among themselves. It appears that the approach of Eq. 4.6 of modeling  $\widehat{L}$  from RANS minimizes the influence of the drop of the OSPS thanks to the higher mean axial velocity of the inner flow regions. Overall, the three curves show a reasonable agreement through a simple proportionality constant.

The constants  $C_{\widehat{L}}$  used for Fig. 4.35 are very similar among the two jets, with values  $C_{\widehat{L}} = 0.46$  and  $0.53$ . Unfortunately, the proportionality factors to match the OSPS and radiator distributions are not so consistent, with  $C = 0.65$  for jet AXI04U and  $C = 0.91$  for jet ECC09U.

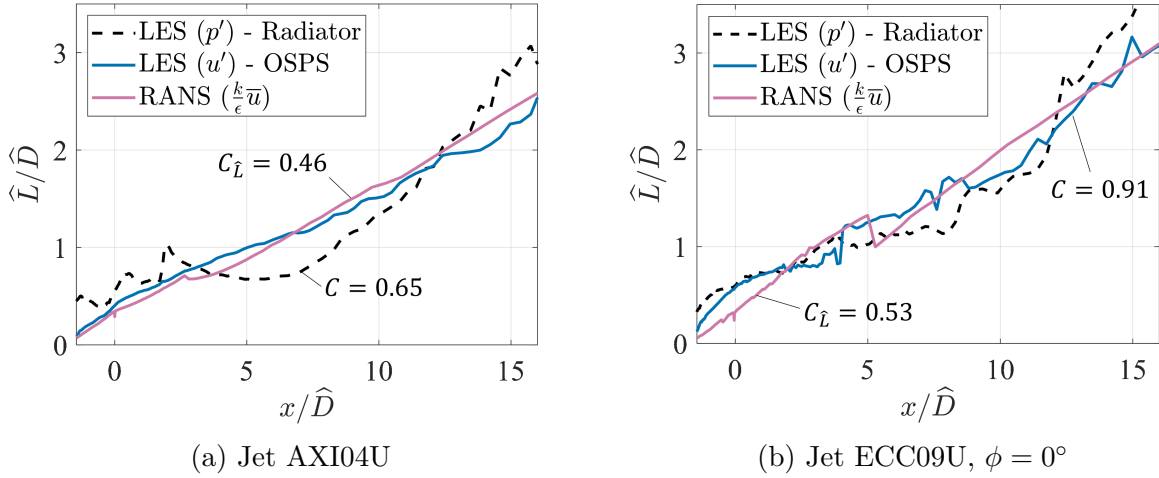


Figure 4.35: Fitting of  $\widehat{L}_u$  on the OSPS and RANS-based length scales to the  $\widehat{L}_p$  distribution on the radiator surface.

## 4.6 Azimuthal Correlations

### 4.6.1 Azimuthal Scales

In this section, we present the analysis of the azimuthal scales of the three-stream jets of this work. The definition of azimuthal scale of turbulence based on two-point space correlations of Eq. 3.4 can be extended to non-axisymmetric jets as

$$R_{ff}(x, r, \alpha) = \frac{\overline{f(x, r, \phi, t) f(x, r, \phi + \alpha, t)}}{\left(\overline{f^2(x, r, \phi, t)} \overline{f^2(x, r, \phi + \alpha, t)}\right)^{1/2}} \quad (4.7)$$

Similarly to Eq. 3.5, the azimuthal scales  $\Phi_u$  and  $\Phi_p$  are the azimuthal angle  $\alpha$  for which the correlations  $R_{uu}$  and  $R_{pp}$ , respectively, decay to  $1/e$ . The distributions of azimuthal scales  $\Phi$  of jets AXI04U and ECC09U are presented below. As with the longitudinal scales in Subsection 4.5.2, the results for jet AXI04U are averaged in the full azimuthal direction, and those for jet ECC09U are averaged on a  $20^\circ$  angle centered on  $\phi = 0$ .

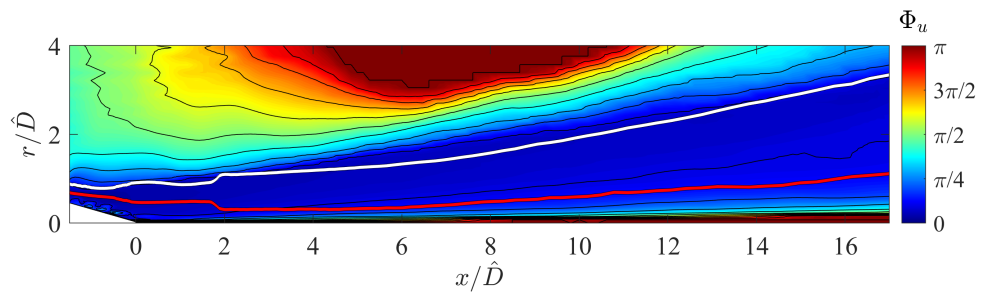
The distributions of azimuthal scales based on axial velocity fluctuation,  $\Phi_u$ , are presented in Fig. 4.36. The analogous scales based on pressure fluctuation,  $\Phi_p$ , are plotted in Fig. 4.37. There are obvious similarities of these distributions with the azimuthal scales of the single-stream jet presented in Section 3.5. By definition, the flow has full azimuthal coherence near the centerline as  $r \rightarrow 0$ . Going radially outwards from the centerline, the scales decrease, reach a plateau of low coherence, and then increase near the edge of the jet. The radial location and scale level of that plateau increases with axial location. For example, it is near  $\Phi_u = 0.05\pi = 9.2^\circ$  at  $(x, r) = (1.0, 0.5)\hat{D}$  for jet AXI04U, but it increases slightly to  $\Phi_u = 0.07\pi = 12.6^\circ$  at  $(x, r) = (7.0, 1.15)\hat{D}$  for the same jet.

Comparing the two types of azimuthal scales, it is evident that the pressure-based scales are higher than the velocity-based scales at a given point. This difference is in line with the results from Chapter 3 and the intuitive concept that pressure fluctuations capture bigger turbulence scales. In addition, the pressure-based scales  $\Phi_p$  exhibit a faster increase at the edge of the jet, which coincide with the radiator surface. As observed with the single-stream jet, this large coherence is consistent with the radiation pattern of turbulent jets, where the low azimuthal modes dominate at shallow angles and are responsible for the jet noise directivity [30].

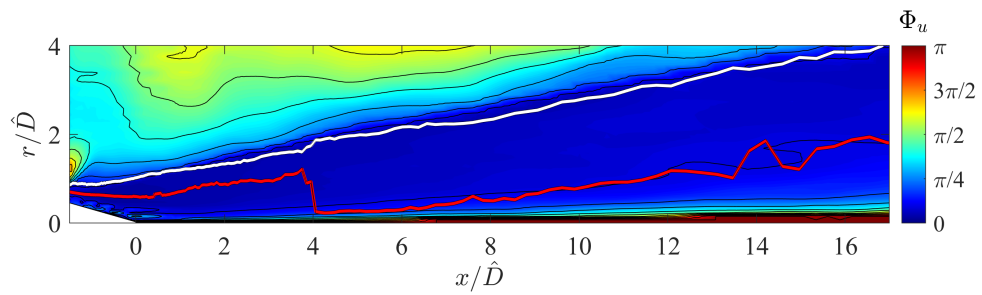
## 4.6.2 Modeling Based on RANS Flow Field

Here we attempt to fit the distribution of LES-based  $\Phi_u$  on the OSPS and the RANS-based azimuthal scales to the LES-based  $\Phi_p$  on the radiator surface through simple proportional relations, as done with the longitudinal scales above. The azimuthal scales are modeled from the RANS flow field in the same from Eq. 3.11, repeated here for clarity,

$$\Phi = C_\Phi \frac{k^{3/2}}{\epsilon r} \tag{3.11 revisited}$$

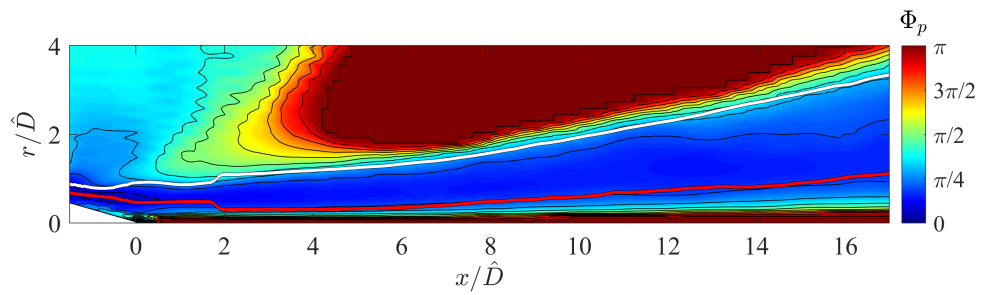


(a) Jet AXI04U

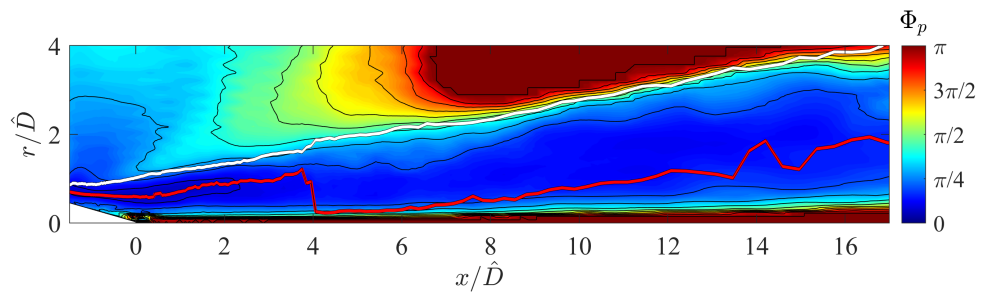


(b) Jet ECC09U,  $\phi = 0^\circ$

Figure 4.36: Isocontours of azimuthal scales based on axial velocity fluctuation,  $\Phi_u$ . Red line: OSPS. White line: radiator surface.



(a) Jet AXI04U



(b) Jet ECC09U,  $\phi = 0^\circ$

Figure 4.37: Isocontours of azimuthal scales based on pressure fluctuation,  $\Phi_p$ . Red line: OSPS. White line: radiator surface.

The values from  $k$  and  $\epsilon$  are taken from the RANS solution at the OSPS, and  $r$  is the radius of the radiator surface.

The results for jets AXI04U and ECC09U are shown in Figs. 4.38(a) and 4.38(b), respectively. It is apparent that no good, consistent match can be achieved with the current methodology. In jet AXI04U, the curves of  $\Phi_u$  and  $\Phi_p$  exhibit somewhat similar trends of initial growth and later saturation, but the initial growth of  $\Phi_p$  is faster. They are fitted through a proportionality factor of  $C = 2.21$  multiplying the  $\Phi_u$  on the OSPS, through an attempt to match the saturated portion only. The RANS-based scales do not share the same trend and instead they grow consistently throughout the jet flow, with the exception of a sudden drop where the RANS-based OSPS shifts from outer to inner shear layers.

The trends of the azimuthal scales on jet ECC09U, shown in Fig. 4.38(b) also show little agreement among themselves and with jet AXI04U. The curve of  $\Phi_p$  on the radiator surface exhibits an initial growth up to  $x/\hat{D} \approx 7.5$ , but does not saturate. The other two curves are strongly affected by the uneven geometry of the relevant surfaces. The variation of  $\Phi_u$  on the OSPS has an initial slow growth, followed by a strong jump due to the collapse of the LES-based OSPS, after which its value decays until stabilizing near  $x/\hat{D} = 10$  at  $\Phi_u = 3\pi/8$ . The curve of RANS-based  $\Phi$  matches well the  $\Phi_p$  distribution until  $x/\hat{D} \approx 2.5$ , after which it increases suddenly due to the undulation of the RANS-based radiator (see Fig. 4.20) and drops due to the collapse of the OSPS.

There seems to be little agreement among the azimuthal scales extracted from LES and those modeled from RANS through the current approach, which involves using simple proportionality constants. The origin of such differences reside in the fact that the azimuthal scales are too sensitive to the geometry of the relevant surfaces. For example, even though jets AXI04U and ECC09U exhibit similar  $x - r$  distributions of azimuthal scales in Figs. 4.36 and 4.37, the position of the radiator on jet ECC09U is slightly further into the high coherence region of the linear field. That reflects into higher values and a different variation

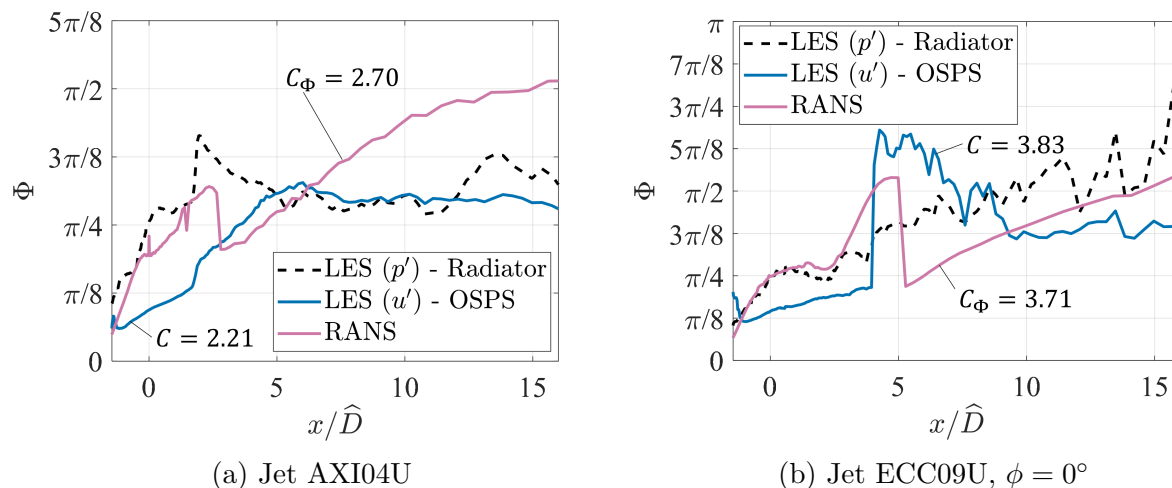


Figure 4.38: Fitting of  $\Phi_u$  on the OSPS and RANS-based azimuthal scales to the  $\Phi_p$  distribution on the radiator surface.

of  $\Phi_p$  along that surface, which causes higher values of coefficients  $C$  and  $C_\Phi$ . The other clear example is the strong influence of the collapse of the OSPS surfaces in  $\Phi_u$  and RANS-based  $\Phi$ . It can be seen how those curves would resemble more each other and that of  $\Phi_p$  if they did not showed such jumps. Further studies should investigate how these issues can be mitigated.

## 4.7 Summary

This chapter explores the connections between the vortical and near-acoustic fields of two three-stream jets. The purpose is to understand the flow dynamics to aid in the development of the linear, surface-based model outlined in Section 2.4.3. One jet is coaxial and the other is has an eccentric tertiary flow that yields noise suppression in preferred directions. They are named AXI04U and ECC09U respectively. They operate at identical conditions, which simulate the takeoff set point of a supersonic turbofan engine.

The two jets are simulated through LES and RANS. The two techniques yield similar time-averaged flow fields, with the RANS simulations predicting moderately slower flow mixing and consequently longer potential cores.

LES-based correlations are used to assess a key assumption in the RANS-based model, the modeling of the convective velocity  $U_c$  of the turbulence eddies as the mean axial velocity on the OSPS. The comparisons of LES and RANS results show a good agreement, which suggests the validity of this assumption.

The radiator surface, already defined in Section 3, is also located for these three-stream jets using the distributions of convective velocities. Again, the location near the edge of the jet where the convective velocity equals that of the OSPS yields a surface located at the boundary between the rotational and irrotational fields, and can be approximated well using a criterion based on the mean vorticity.

The LES flow field is used to investigate the region near the edge of the jet to understand the connection to the inner vortical field. Computation of the skewness of pressure and velocity fluctuations, visualization of the instantaneous flow field, and analysis of the correlation of pressure and vorticity reveals that the edge of the jet is affected by sparse, slow-moving vortices that peel off from the main flow and travel along the vicinity of the radiator surface. They constitute the last remnants of the vortical field. This finding also helps confirm the correct location of the radiator surface as the boundary between rotational and irrotational fields.

We use two-dimensional space-time correlations to investigate the connection between the inner, vortical field and the very near pressure field. The correlations are centered on the inner shear layer and computed along the symmetry plane and  $\phi = 0$ . They help visualize how the asymmetry of the tertiary stream and the resulting thicker low-speed flow weaken the radiation efficiency of the high-speed eddies.

Axial and azimuthal turbulence scales are calculated, and the potential of RANS to emulate those scales is evaluated. The focus is on  $p'$ -based scales on the radiator surface, and  $u'$ -based scales on the OSPS. The RANS-based length scales, computed by  $k^{3/2}/\epsilon$  and adjusted by a proportionality factor, show a reasonably similar trend but not a close agreement to the LES-based fixed-frame length scales. An alternative approach to modeling the length scales, using the mean axial velocity as  $k\bar{u}/\epsilon$ , is used to match the curves of moving-frame length scales  $\hat{L}$ . With that approach, the RANS length scales are in good agreement with the  $u'$  scales on the OSPS, but the  $p'$  scales on the radiator surface show a different trend altogether. Finally, the trends of the azimuthal scales do not closely match and seem to be too sensitive to the uneven geometries of the OSPS and the radiator surface.

# Chapter 5

## Elements of a Linear Surface-Based Model

This chapter presents a simplified model for the jet turbulent mixing noise at angles close to the direction of peak emission. This model aims to predict the change in noise level when altering a jet baseline design. An example of alteration is the change in geometry from jet AXI04U, used here as the baseline jet, to the asymmetric geometry of jet ECC09U.

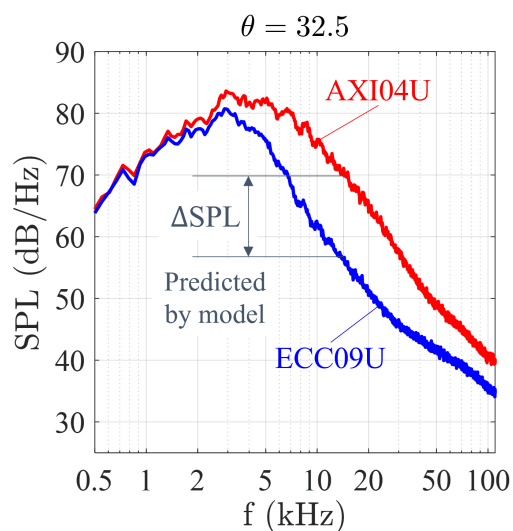


Figure 5.1: Far field SPL spectrum of jets AXI04U and ECC09U.

This simplified model studies the far-field sound at the direction of peak emission. Figure 5.2 illustrates this idea. First, we will build a set of wavepackets that are informed from the RANS flow field of jet AXI04U and depend on a set of empirical parameters  $\mathbf{C}$ . Those parameters are then calculated by fitting the far-field emission of the wavepacket set to the AXI04U spectra at the polar angle  $\theta = 32.5^\circ$ . As will be shown later in Section 5.3, this process presented inaccuracies that indicate problems with the present wavepacket model. Ultimately, the wavepacket model would be informed by the RANS flow field of the modified jet, ECC09U in this work, and its far-field spectra would be extrapolated using the set of empirical constants  $\mathbf{C}$  obtained using the reference jet.

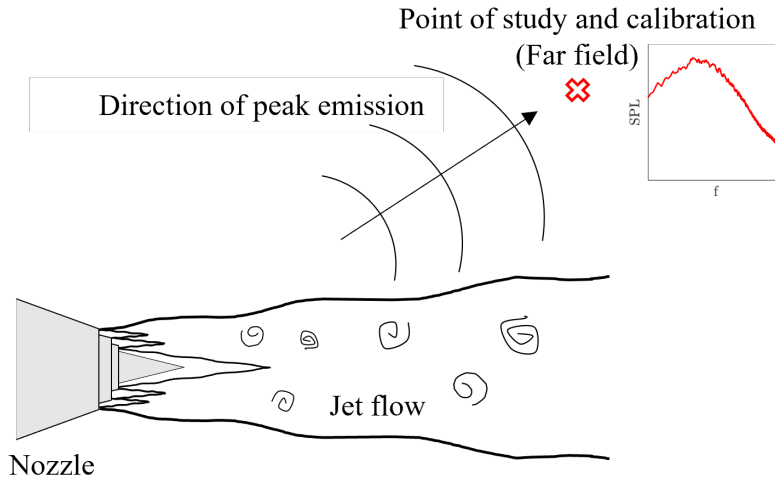


Figure 5.2: Sketch of noise radiation and point of study of the wavepacket model.

Aiming at modeling the directional emission of the jets allows for simplifications in the model, e.g. the use of axisymmetric wavepackets. Nevertheless, the amount of information available in the noise spectra of a single point is limited, so the present model uses a simplified approach to reduce the number of empirical constants to calibrate.

## 5.1 Theoretical Framework

We start with a generalized form of a wavepacket of a given frequency, prescribed on the radiator surface

$$p_{wp}(x, r = r_{rad}, \phi, t) = p_0(x, \omega, \phi) e^{-i\omega t} \quad (5.1)$$

where  $p_0$  is the wavepacket shape, which is broken down into three terms

$$p_0(x, \omega, \phi) = \mathcal{A}(\omega) q(x, x_0) g_\phi(\phi, \phi_0) \quad (5.2)$$

where  $\mathcal{A}$  is the amplitude;  $x_0$  and  $\phi_0$  are the axial and azimuthal origins of the event; and  $q$  and  $g$  are functions that govern the axial and azimuthal evolution respectively. In this model, the parameters of Eq. 5.2 are all deterministic and function of  $\omega$ . A stochastic model should consider the stochastic nature of  $\mathcal{A}$ ,  $x_0$ , and  $\phi_0$  and their relation with frequency. In fact, previous works by Papamoschou [75] suggest that the characteristic decline in coherence with increasing polar angle are caused by the randomness of the axial origin of the event,  $x_0$ .

The azimuthal evolution can be expanded into

$$g_\phi(\phi) = G(\phi, \phi_0) e^{i\beta(\phi - \phi_0)} \quad (5.3)$$

where  $G$  defines the azimuthal envelope and  $\beta$  is the helicity. For this model, the azimuthal dependence is ignored so that noise sources are axisymmetric, therefore  $g_\phi(\phi, \phi_0) = 1$ . This step greatly simplifies the treatment of the helicity, which has been shown to have a dependence with frequency as  $\beta(\omega)$  [75], but it is unclear how that relation can be obtained by RANS. We can justify this simplification with the fact that this model aims to calculate the noise generation near the direction of peak noise, which it has been shown to be dominated

by the axisymmetric component [30]. For noise predictions at higher polar angles from the jet downstream direction ( $\theta \gtrsim 40^\circ$ ), higher modes would be required [30, 75, 76].

The pressure perturbation at the radiator surface is a superposition of wavepackets at a range of frequencies

$$p_{rad}(x, r = r_{rad}, t) = \int_{-\infty}^{\infty} \mathcal{A}(\omega) q(x, x_0(\omega)) e^{-i\omega t} d\omega \quad (5.4)$$

The pressure outwards from the jet could be computed analytically if the radiator surface were a cylinder, as it is explained in the appendix section A.2. This model determines the radiator surface from the vorticity field of a RANS simulation, and it tends to resemble more to the shape of a cone. The radiator surface may also be irregular, as it is affected by the complex flow-field of multi-stream jets. For that reason, calculation of the pressure propagation outwards from the jet must be done computationally. This model uses boundary element method (BEM), explained in the appendix section A.1, for that purpose.

### 5.1.1 Axial shape

The axial evolution  $q$  of Eq. 5.2 is expanded as

$$q(x, x_0) = W(x, x_0) \exp\{i\kappa_{wp} (x - x_0)\} \quad (5.5)$$

where  $W$  is a function defining the axial envelope shape and  $\kappa_{wp}$  is the axial wavenumber. The axial wavenumber of the wavepacket is related to the convective velocity and frequency through

$$k_{wp}(\omega, x_0) = \frac{\omega}{U_c(x_0)} \quad (5.6)$$

where it is assumed that the velocity of wavepackets originating at a given  $x_0$  does not depend on their frequency [4].

The axial envelope  $W$  is assigned to be a Gaussian function

$$W\left(\frac{x-x_0}{L_{wp}(x_0)}\right) = \exp\left\{-\left(\frac{x-x_0}{L_{wp}(x_0)}\right)^2\right\} \quad (5.7)$$

where  $L_{wp}$  is the wavepacket length scale, which is informed by the RANS flow field. This simple shape is chosen in order to minimize the amount of parameters to calibrate with the reference jet. The Gaussian envelope is centered at  $x_0$  and its width is adjusted by  $L_{wp}$ . The envelope  $W$  only depends on frequency through the relation between central location and frequency,  $x_0(\omega)$ .

### 5.1.2 Modeling from RANS

The model is informed by the RANS results through the vorticity, axial velocity, turbulence kinetic energy and dissipation. The vorticity is used to calculate the location of the radiator surface through the criterion derived in Section 4.4.2. The other values ( $u$ ,  $k$ , and  $\epsilon$ ) are taken at the OSPS location to provide the distribution of length scales and the relation between the event's axial origin  $x_0$  and the wavepacket frequency  $\omega$ .

The wavepacket length scales are based on the RANS-based length scales at the OSPS at the same axial location  $x$ , through an expression equivalent to Eq. 3.10,

$$L_{wp}(x) = C_L L_{RANS}(x) = C_L \frac{k(x, r_{OSPS})^{\frac{3}{2}}}{\epsilon(x, r_{OSPS})} \quad (5.8)$$

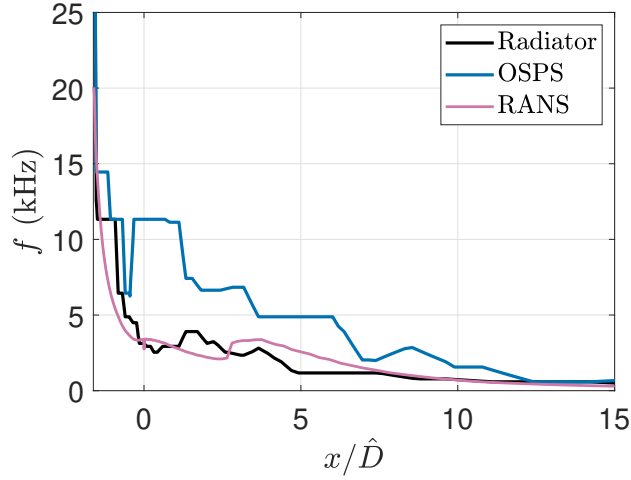


Figure 5.3: Peak frequencies of the pressure autospectra on the OSPS and radiator surface of jet AXI04U. RANS-based frequencies are adjusted by  $C_f = 0.3$ .

The connection between frequency and the event’s origin is provided by the RANS-based characteristic frequency adjusted by the proportionality factor  $C_f$ ,

$$\omega(x) = 2\pi C_f \frac{\epsilon(x, r_{OSPS})}{k(x, r_{OSPS})} \quad (5.9)$$

The factor  $2\pi$  is added so that the proportionality factor reflects a more direct connection between the ratio  $\epsilon/k$  and the wavepacket frequency in Hertz. This modeling approach is based on Ref. [83] and shown in Fig. 5.3. It is surmised that the origin of an event of given frequency is related to the location where that frequency dominates. Figure 5.3 plots the peak frequencies of the pressure autospectra along the OSPS and radiator. The curve of characteristic frequency, as calculated by Eq. 5.9, matches well those two distributions with adequate proportionality factors. Those factors are  $C_f = 0.3$  for the curve on the radiator surface, and  $C_f = 0.8$  for the curve on the OSPS.

The wavepacket amplitude  $\mathcal{A}$  is a difficult parameter to infer from the RANS flow field. Earlier works have left the function  $\mathcal{A}(\omega)$  as an entirely free parameter to be adjusted with the reference jet. However, this model will be calibrated with just one observer position, so leaving amplitude as an unbounded function of frequency would render the model with more

unknowns than equations. Given that the shape of isotropic turbulence spectra commonly resembles a log-normal distribution [31], it is reasonable to parametrize  $\mathcal{A}$  as

$$\mathcal{A}(\omega) = \exp \left\{ - \left( \frac{\log(\omega) - C_1}{C_2} \right)^2 \right\} \quad (5.10)$$

It should be noted that the first challenge of the model is to match the *shape* of the power spectrum of the jet AXI04U, not its actual values. For this reason, Eq. 5.10 does not contain a parameter outside the exponential that governs the levels of  $\mathcal{A}(\omega)$ .

## 5.2 Methodology

### 5.2.1 BEM input

The boundary element method explained in section A.1 allows for the computation of the pressure field generated by a wavepacket of a given frequency which is prescribed on the radiator surface. Calculating the acoustic transfer matrix facilitates the solution of the pressure field from a wavepacket of a different shape, but it is still restricted to the same frequency. In order to simplify the meshing process and the BEM solution of each frequency, only 12 frequency points are used to model the AXI04U spectrum of Fig. 5.1 between 1kHz and 25 kHz.

To save computational cost, the radiator surface is only extended along reasonable locations where a wavepacket of a given frequency might be located through Eq. 5.9. Therefore, each modeled frequency is associated with an expected origin location  $x_0$  and a cutoff location  $x_{\max}$ , after which the radiator surface is closed with a polynomial to render a closed body for BEM. The expected origin is based on the peak frequency distribution of Fig. 5.3, taken from the pressure fluctuation at the OSPS of jet AXI04U from the LES results. The

cutoff locations are determined to be, for each frequency  $f$ , the approximate location of its half frequency  $f/2$ . The modeled frequencies, expected locations  $x_0$ , and cutoff coordinates  $x_{\max}$  for jet AXI04U are shown in Table 5.1.

The grid elements in the discretization of the radiator surface must be fine enough to resolve well A) the acoustic wavelength  $\lambda_\infty = a_\infty/f$ , which is a common BEM requirement, and B) the wavepacket shape, including the axial fluctuation governed by the term  $e^{i\omega/U_c(x-x_0)}$  of Eq. 5.5. We can define the wavepacket wavelength, also named the hydrodynamic wavelength, as  $\lambda_{wp} = U_c/f$ . As a rule of thumb, the grid elements should be small enough to contain at least six elements per wavelength. Here, the convective velocity  $U_c$  for each frequency is estimated based on its expected location  $x_0$ , and meshed to have at least six elements per the smallest wavelength, acoustic or hydrodynamic. In order to be conservative with the degree of uncertainty presented by the convective velocity, for which we initially have only an estimate, the grids are finer than the minimum requirement. Low frequencies have 12 or more elements per wavelength, and higher frequencies ( $f \geq 10$  kHz) have as many elements as permitted by 32 GB RAM of the PC used. The estimated convective velocities, wavelengths, and final element sizes are shown in Table 5.1. The meshing process was done using triangular elements in Ansys<sup>®</sup> Academic Research Mechanical, Release 2021 R1. The BEM software used was FastBEM Acoustics<sup>®</sup> Release 6, and it is validated against an analytical result in the appendix section A.2.

### 5.2.2 Model calibration

For a known wavepacket shape  $p_0$ , we can write it as  $p_0(x, \omega, \mathbf{C})$ , where  $\mathbf{C} = C_1, C_2, C_f, C_L$  is the array of calibration parameters explained in section 5.1.2. The idea is then to select the set of parameters  $\mathbf{C}$  that minimizes the difference between the modeled sound intensity  $S_{\text{mod}}(\omega, \mathbf{C})$ , calculated with BEM for a point at a distance of  $100\hat{D}$  and  $\theta = 32.5^\circ$ , with the

f (kHz)	$St$	Estimated $x_0/\hat{D}$	$x_{\max}/\hat{D}$	$U_c(x_0)/\hat{U}$	$\lambda_\infty/\hat{D}$	$\lambda_{wp}/\hat{D}$	Element length
1	0.0	12.48	14.55	0.32	13.79	5.59	27.84 $\lambda_{wp}$
2	0.11	10.98	14.55	0.37	6.89	3.23	16.10 $\lambda_{wp}$
3	0.17	8.23	12.67	0.57	4.60	3.32	16.53 $\lambda_{wp}$
4	0.23	5.79	9.60	0.81	3.45	3.54	17.18 $\lambda_\infty$
5	0.29	4.38	9.52	0.91	2.76	3.18	13.75 $\lambda_\infty$
6	0.34	3.25	7.52	0.85	2.30	2.48	11.93 $\lambda_\infty$
7	0.40	2.07	7.05	0.52	1.97	1.30	11.97 $\lambda_{wp}$
8	0.46	1.55	5.81	0.49	1.72	1.07	11.58 $\lambda_{wp}$
10	0.57	0.16	4.39	0.40	1.38	0.70	9.16 $\lambda_{wp}$
15	0.86	-1.06	3.35	0.36	0.92	0.42	8.70 $\lambda_{wp}$
20	1.15	-1.43	1.72	0.36	0.69	0.31	9.03 $\lambda_{wp}$
25	1.43	-1.53	1.72	0.36	0.55	0.25	7.70 $\lambda_{wp}$

Table 5.1: Parameters for BEM modeling of jet AXI04U.

experimental intensity distribution  $S_{\text{exp}}(\omega)$  shown in Fig. 5.1. Given that the main focus is on matching the shape of spectrum and not its absolute value, we normalize the modeled and experimental distributions by their peak values. Expressing  $S_{\text{mod}}$  and  $S_{\text{exp}}$  in decibels,

$$\begin{aligned}\hat{S}_{\text{mod}}(\omega, \mathbf{C}) &= S_{\text{mod}}(\omega, \mathbf{C}) - S_{\text{mod}, \max}(\mathbf{C}) \\ \hat{S}_{\text{exp}}(\omega) &= S_{\text{exp}}(\omega) - S_{\text{mod}, \max}\end{aligned}\tag{5.11}$$

where  $\max$  denotes the peak value of the spectral distribution.

The calibration is carried out by minimizing the cost function  $F(\mathbf{C})$  with the normalized modeled and experimental autospectra known at the discrete frequencies  $\omega_j, j = 1, \dots, J$ , specified in Table 5.1.  $F(\mathbf{C})$  is defined as

$$F(\mathbf{C}) = \sqrt{\frac{1}{J} \sum_{j=1}^J \left[ \hat{S}_{\text{exp}}(\omega_j) - \hat{S}_{\text{mod}}(\omega_j, \mathbf{C}) \right]^2}\tag{5.12}$$

The value of  $\mathbf{C}$  that minimizes  $F(\mathbf{C})$  is calculated with the function *fmincon* in MATLAB<sup>®</sup> Release 2020b [63], which prioritizes the ‘‘Interior-Point’’ algorithm. After the shape differ-

ence is minimized, the absolute level of the modeled distribution can be easily matched to that of the experimental distribution. Removing the coefficient to match the absolute levels in the first step of the calibration simplifies the minimization process for  $\mathbf{C}$ .

## 5.3 Model Results

The wavepacket model explained in Section 5.1 is calibrated for the experimental far-field autospectra of jet AXI04U at  $\theta = 32.5^\circ$  using the wavepacket propagation and noise level minimization for the parameter array  $\mathbf{C} = (C_1, C_2, C_f, C_L)$  outlined in Section 5.2. The calibrated parameter array is  $C_1 = 7.3 \times 10^3$ ,  $C_2 = 0.58$ ,  $C_f = 0.88$ , and  $C_L = 0.5$ , which results in the far-field pressure spectrum and wavepackets shown in Fig. 5.4.

The scaled SPL levels of Fig. 5.4a are in reasonable agreement with the experimental results, but the wavepacket shapes of each frequency, shown in 5.4b located at their corresponding event location  $x_0(\omega)$ , are less encouraging. It is evident that their length scales are too short to represent a traveling wave, and instead appear as compact sources of noise. These wavepacket shapes are not in agreement with the expected axial fluctuation of previous works by many authors [29, 61, 76, 86].

### 5.3.1 Effects of Length Scales

To investigate the effect of the length scales on the noise generation, we plot the SPL distribution along the vertical plane for various values of  $C_L$  in Fig. 5.5. The wavepackets used have a frequency of  $f = 4$  kHz located at  $x_0 = 6.8\hat{D}$  with a convective velocity of  $U_c = 0.63\hat{U} = 0.8a_\infty$ . These parameters correspond to a frequency coefficient of  $C_f = 0.65$  approximately. The amplitude is set to 40 Pa. The radiator surface is visible at the top left of each contour.

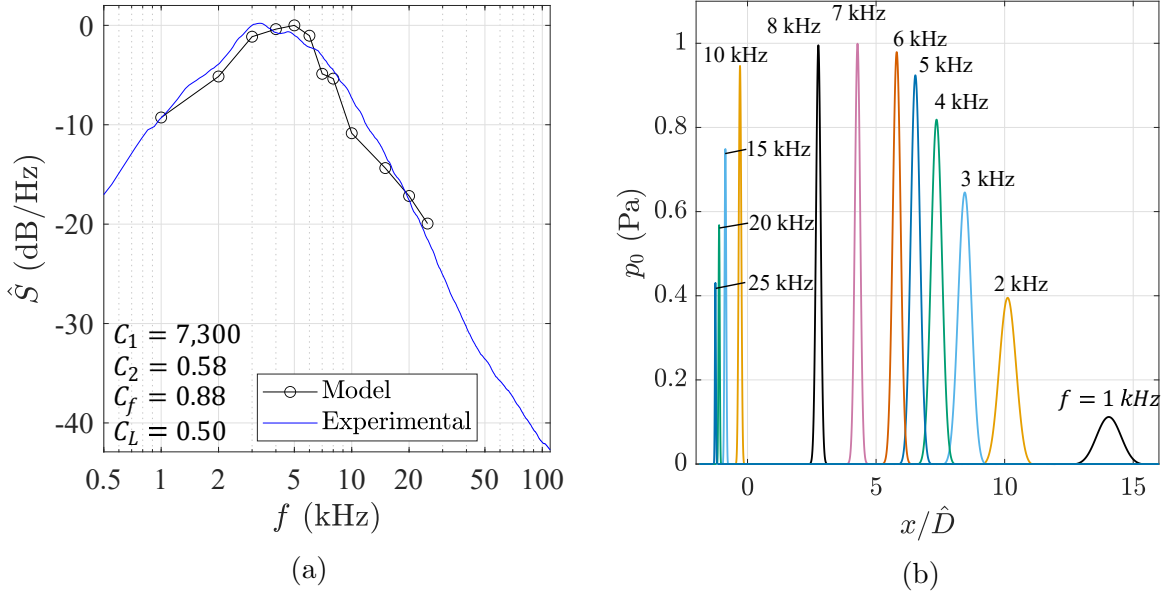


Figure 5.4: Results of model calibration to experimental far-field autospectra of jet AXI04U at  $\theta = 32.5^\circ$ . (a) Comparison of scaled experimental and modeled autospectra, and (b) real part of the axial distribution  $p_0(x)$ .

From Fig. 5.5, it is evident that very short length scales affect the noise directivity of the wavepackets to a more isotropic radiation. The values obtained by the minimization, near  $C_L = 0.5$ , resemble the radiation showed by Fig. 5.5a. This is not the characteristic radiation pattern of a wavepacket. Results by other authors [30], as well as from this work, suggest that the expected radiation pattern resembles the one shown by  $C_L = 4.0$  in Fig. 5.5d. It is then sensible to force the model to use larger length scales, which are more physically consistent with the wavepacket physics, and study the influence of the parameters  $C_L$  and  $C_f$  on the resulting spectrum.

Forcing the model to use larger values of  $C_L$  narrows the modeled spectrum and makes the minimization process difficult. In fact, the subroutine *fmincon* used cannot find a better parameter combination when supplied the optimal parameters of Fig. 5.4 but with  $C_L$  changed to  $C_L = 4.0$ . The resulting spectrum of this new parameter combination, shown in Fig. 5.6, does not adequately resemble the experimental pressure spectrum.

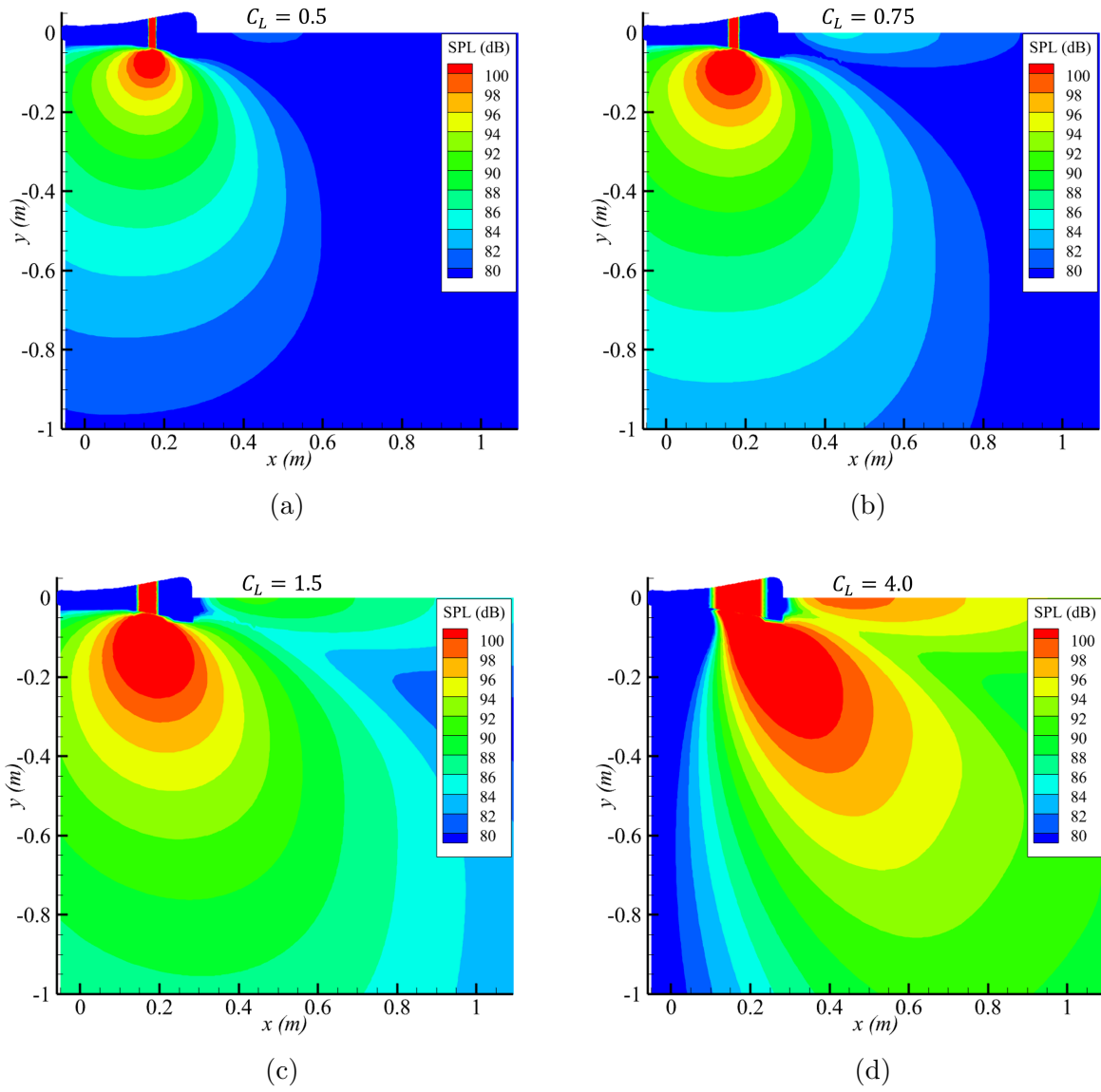


Figure 5.5: Sound pressure levels generated by wavepackets of different length scales, all other parameters equal.

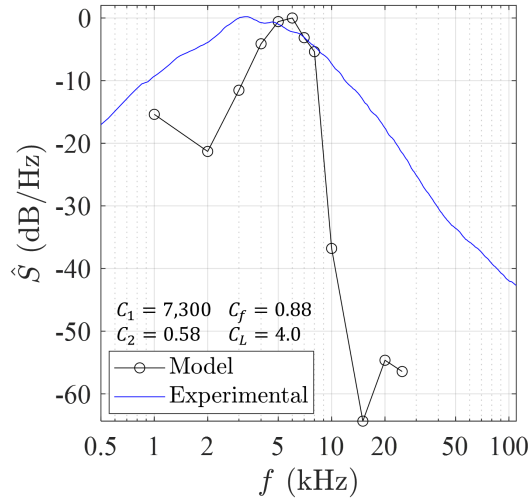


Figure 5.6: Comparison of scaled experimental and modeled autospectra using a length scale coefficient of  $C_L = 4.0$ .

### 5.3.2 Effects of Frequency and Length Coefficients

Next, we study the effects of changing the values of  $C_f$  and  $C_L$  independently to understand the behavior of the model and the narrowing of the modeled spectrum shown in Fig. 5.6. The coefficients are changed around the “physically realistic” values of  $C_L = 4.0$  and  $C_f = 0.6$ . In order to minimize the effects of the arbitrary amplitude function used (Eqn. 5.10) and its coefficients  $C_1$  and  $C_2$ , we set a constant amplitude across all frequencies  $\mathcal{A} = 1$ . The results are plotted in Fig. 5.7.

Figure 5.7 shows that increasing  $C_f$  and  $C_L$  separately cause their far-field pressure autospectrum to turn concave. In order to understand the effects of changing  $C_f$ , we also plot the axial distribution of convective velocity  $U_c(x_0)$  in Fig. 5.8. The values of  $U_c$  assigned to the modeled wavepackets for  $C_f = 0.6$  are shown as blue circles. Decreasing the value of  $C_f$  moves the event origins of each wavepacket upstream, so the blue circles would shift to the left following the distribution of  $U_c(x_0)$ . For the very low value of  $C_f = 0.1$  shown in Fig. 5.7(a), all frequencies have similar low values of convective velocity and their radiation levels are also comparable. Increasing  $C_f$ , seen along Figs. 5.7(a-e) introduces a wider range of

convective velocities across all frequencies. The autospectra then acquire a concave shape, and the frequencies of high convective velocities dominate the noise radiation. It should be noted that the sudden increase in noise levels of the low frequencies seen in Figs. 5.7(c-e) are numerical artifacts, a result of the wavepackets extending beyond the axial extent of the radiator surface  $x_{\max}$ . A proper computation of their radiation should consider increasing the levels of  $x_{\max}$  used in Table 5.1.

Let us now analyze the effects of changing  $C_L$ , shown across Figs. 5.7(f-i). Again, we see the numerical artifact of high noise levels at low frequencies, which should be ignored. Increasing  $L$  from the very low value of  $C_L = 0.5$  of Fig. 5.7(f) has the effect seen in Fig. 5.5, for which the wavepacket noise generation goes turns more directive. Therefore, the increase in  $C_L$  is associated with narrowing the spectra into a convex shape. The frequencies associated with higher convective velocities, near  $f = 5$  kHz, show higher radiating power towards the low angle modeled,  $\theta = 32.5^\circ$ .

Regardless of which coefficient is changed in Fig. 5.7, there is no clear direction which brings the modeled autospectra to resemble the experimental results. We can conclude that, under the current assumptions, there is no combination of parameters that yields a good approximation of the far-field radiation of jet AXI04U. By inspection of Fig. 5.7, it can be seen that the modeled spectra tend to be too narrow to match the experimental spectrum. For example, for Fig. 5.7(c), the model matches the peak shape but the higher frequencies are too quiet.

We postulate that the problem lies in the association of each frequency to a single location through Eq. 5.9 and the fact that that location may not be the dominant noise source. In fact, the essential idea of Eq. 5.9 is that one frequency is related to the location where it is dominant. However, for the same frequency, there may be other locations where it is more acoustically efficient due to different turbulence scales, even if it is not the dominant frequency on that location. This may be the case for the high frequencies of Fig. 5.7(c), which

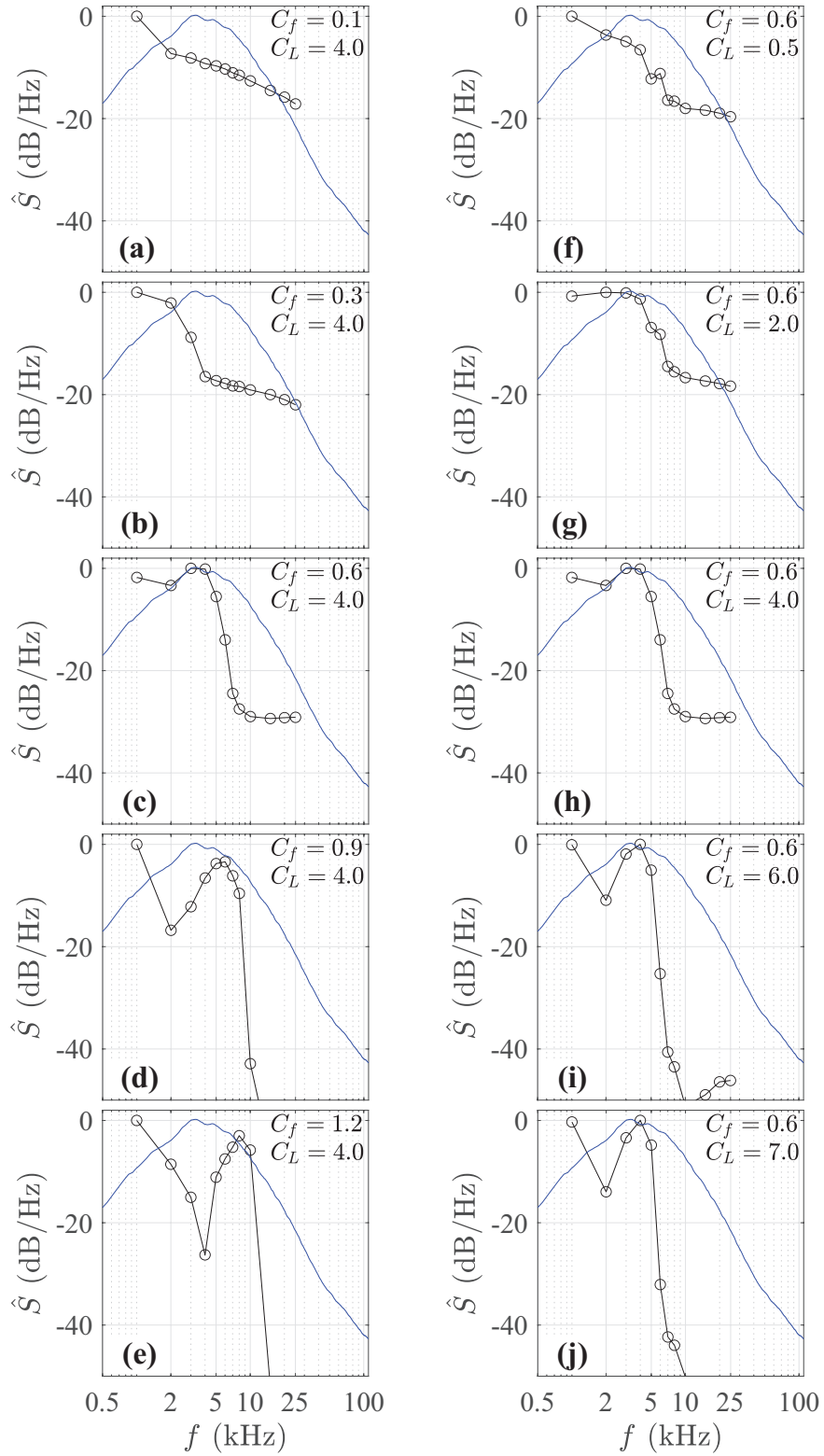


Figure 5.7: Changes in modeled autospectrum generated by changing  $C_f$  (left column) or  $C_L$  (right column) around point  $C_f = 0.6$  and  $C_L = 4.0$ . Wavepacket amplitude is  $\mathcal{A} = 1$  for all cases.

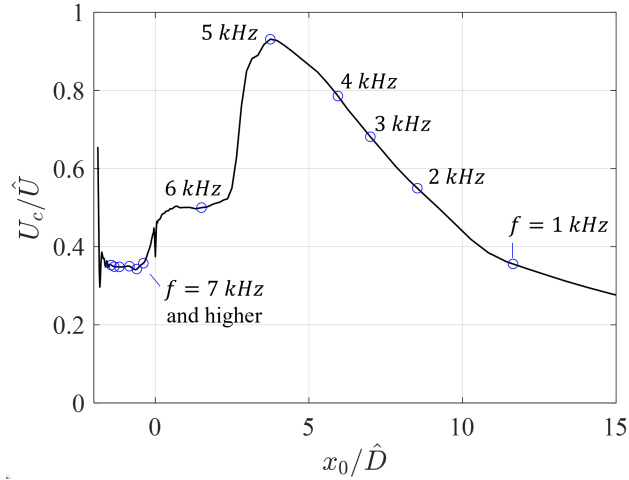


Figure 5.8: Convective velocity distribution  $U_c$  (solid line) and values assigned to the modeled wavepackets (circles) for  $C_f = 0.6$ .

are assigned to early axial locations with low convective velocity and length scales. To visualize this idea, we plot the pressure spectra along the radiator surface in Fig. 5.9. The black line denotes the maximum frequency at each axial location, which is the relation between frequency and location modeled by Eq. 5.9. It is evident from the contour that the region of  $0 \leq x/\hat{D} \leq 10$  contains strong frequency components that are not well approximated by the black line, and that would be difficult to be assimilated into a one-dimensional array altogether. Future modeling efforts should consider alternative forms of relating frequency and event origin, including taking into account the stochastic behavior of the event origin  $x_0$ .

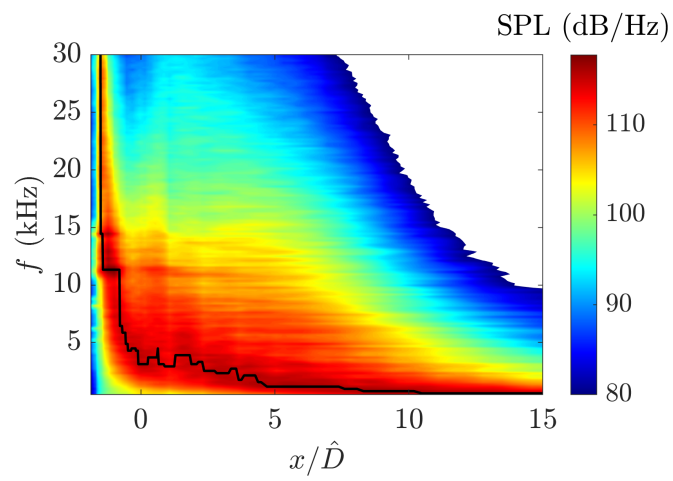


Figure 5.9: Pressure spectra along the radiator surface. The black line denotes the maximum frequency at each axial location.

# Chapter 6

## Conclusions

### 6.1 Summary of Work Completed

This computational study explores connections between the vortical and near-acoustic fields of single- and multi-stream jets whose understanding will aid in the noise source modeling of these flows. The ultimate goal is development of linear, surface-based models that would be informed by low-cost RANS solutions. The study used one single-stream jet and two triple-stream jets.

The model envisioned in this work is a linear, surface-based model for the jet noise source. It is greatly influenced by the approach by Papamoschou [74–76] and the analogy of turbulent noise sources to wavepackets [52]. The model prescribes a set of partial fields on a surface enclosing the vortical region of the jet, named the “radiator surface”, which is located at the boundary between the non-linear and linear fields. The partial fields replicate the noise-generating effects of turbulence structures within the flow, and are informed from low-cost RANS simulations.

The single-stream jet is studied through a highly-resolved large eddy simulation (LES). It is round, isothermal, and its initial turbulence levels are set to match experimental conditions. This jet is used to investigate the connection between the statistics of the vortical field and its pressure signature on the edge of the jet. The representative locations for those regions are the surface of peak Reynolds stress (SPS) and the “radiator surface”, respectively. The radiator surface is defined as the location where the convective velocity equals that on the SPS, and it is where the jet noise source model would be prescribed for computation of its noise propagation. Two-point, space-time correlations are used to compute the convective velocity and turbulence scales in the axial and azimuthal directions across the vortical and very near fields of the jet. The correlations are based on the axial velocity fluctuation  $u'$  and pressure fluctuation  $p'$ . In the two cases, two definitions of axial scales are considered, the fixed-frame scale  $L$  and the moving-frame scale  $\hat{L}$ .

The two-dimensional space-time correlations evaluated along a longitudinal and a cross-sectional plane, for reference points on the SPS, help us to understand the phenomena at play and key differences between velocity and pressure fluctuations. On the radial-axial plane, pressure-based correlations exhibit a wavepacket-like pattern that is coherent radially and travels fairly uniformly with the convective velocity  $U_c$  on the SPS. On the contrary, the velocity-based correlation lacks strong radial coherence and its convection is non-uniform, strongly influenced by the local mean-flow velocity. These results suggest that velocity-based correlations capture localized turbulent events, while the pressure-based correlations are dominated by the interaction of large eddies with the surrounding potential flow. Consequently, the axial and radial distributions of the corresponding length scales follow different trends. The pressure-based correlation scales on the radiator surface are larger than the velocity- or pressure-based scales on the SPS, indicating that fine-scale vortical motions do not significantly imprint the pressure field on the radiator surface. These observations are also applicable to correlations on a cross-sectional plane. There, the velocity-based correla-

tion show events at the SPS have a limited range of effect, while pressure-based correlations have a wide azimuthal range of influence, which grows notably outside the radiator surface.

The radial variations of fixed-frame length scales collapse well on a single curve when the radial coordinate is offset by the radial location of the inner edge of the shear layer and normalized by the momentum thickness. This works particularly well for axial locations of  $x \geq 3D_j$ . The same scaling is carried out with moving-frame length scales and azimuthal scales, with equally good results with the exception of moving-frame length scales based on pressure whose growth does not follow that of the momentum thickness. A particularly interesting finding is that the radiator surface passes through a “valley” (local minimum) of velocity-based length scale (fixed or moving-frame), indicating that the velocity fluctuations there are mostly decorrelated from events in the core vortical region.

The potential of extracting relevant velocity and length scales from the time averaged flow field is evaluated on the single-stream jet. LES results are used to emulate a Reynolds-Averaged Navier-Stokes solution (eRANS). The focus is on  $p'$ -based scales on the radiator surface, which can be located by eRANS using the mean vorticity. eRANS can predict satisfactorily the convective velocity on the radiator surface without any fitting parameters. The distributions of azimuthal scale and fixed-frame axial length scale are matched approximately by fitting constants to the eRANS-derived scales. The distribution of moving-frame axial length scale is complex and requires a higher level of empiricism.

Of the triple-stream jets, one is coaxial and the other has an eccentric tertiary flow that yields noise suppression in preferred directions. These jets exhaust at conditions simulating the takeoff set point of a supersonic turbofan engine. They are studied through LES and RANS to assess key modeling assumptions and the ability of RANS to predict the flow field accurately.

An essential requirement for the model is the accurate representation of the convective velocity  $U_c$  of the noise-generating turbulent eddies. Direct evaluation of the Reynolds stress and convective velocity  $U_c$  from the LES show reasonable agreement with the RANS-based modeled values. Nozzle asymmetry causes changes in the geometry of the OSPS and convective velocity that are captured by RANS with a reasonable degree of accuracy. This suggests the validity of modeling the convective velocity of the noise-generating turbulent as the mean axial velocity on the outer surface of peak stress (OSPS).

Despite the irregular shape of the OSPS, the radiator surface is relatively smooth and its geometry can be approximated using a mean-vorticity criterion, therefore it can also be based on the RANS solution. A criterion based on the mean vorticity is formulated that accurately approximates the shape of this surface. We conclude that RANS shows promise in predicting two of the most important elements in the proposed modeling – the geometry of the radiator surface and the convective velocity distribution on it.

Particular emphasis is placed on studying the flow features near the edge of the three-stream jets, where the radiator surface is located. This surface overlaps with a band of negative skewness of the pressure and a double band of opposite values of the skewness of axial velocity. Examination of the instantaneous vorticity field, as well as correlations of vorticity and pressure, show vortices peeling off from the main flow and migrating towards the radiator surface outside of which their strength vanishes. The vortical events near the radiator surface help explain the negative pressure skewness, and reinforce the idea that the radiator surface is located at the boundary between non-linear and linear fields.

The connection between the inner vortical field and the edge of the jet is also investigated through two-dimensional space-time correlations of the velocity and pressure fields. The correlations shed light on the noise generation from the high-speed region of the jet and show how the asymmetry of the tertiary stream, and the resulting thicker low-speed flow, weakens the radiation efficiency of the high-speed eddies.

The distribution of axial and azimuthal turbulence scales on the three-stream jets resemble the trends seen on the single-stream jet. However, their radial trends cannot be collapsed into similarity form due to the complexity of their flow field. Attempts at modeling the scale variations from the RANS flow field yield reasonable results for the fixed frame length scales. The modeled moving-frame length scales match within reasonable accuracy the distribution of  $u'$ -based scales along the OSPS, but the  $p'$ -based scales at the radiator surface exhibit a more complex variation. Overall, the success at modeling the turbulence length scales at the two surfaces is limited, and it appears that the scale values are too sensitive to the uneven geometry of the surfaces.

Finally, we present a simplified version of a deterministic wavepacket model that attempts to replicate the far-field noise spectra of jet AXI04U at the direction of peak noise spectra. The model is informed by the RANS flow field and computes the noise propagation using the boundary element method. This early attempt recreates the main features of the spectra, but the high frequencies are too quiet. It is observed that the method for determining the axial location of a given frequency, based on the ratio  $\epsilon/k$  of the RANS flow field, places the high frequencies too upstream in the jet flow and consequently are acoustically inefficient. However, that modeling approach captured well the peak frequency along the OSPS. Therefore, it can be concluded that the source of a given frequency may not be the same location where that frequency dominates the spectra.

## 6.2 Recommendations for Future Work

This work presents important findings to aid in the development of linear, surface-based models of the noise sources of simple and complex nozzles. Additionally, it also highlights areas that should be the focus of future efforts.

First, the moving-frame length scales based on pressure fluctuation studied on the single-stream jet (Section 3.4.3) are difficult to model due to their accelerated growth during the first few diameters of the jet, which reflect a non-similar behavior for the extent of the potential core. It is suggested that this might be related to a different mechanism of turbulence generation, but it is very interesting to explore the origin of this difference, and why it is not reflected on velocity-based moving-frame length scales or in fixed-frame length scales.

Next, a very important assumption of this work is that the noise sources, which are frequency-dependent, can be studied and modeled using two-point correlations of the LES flow field and the time-averaged RANS solution, both of which are not frequency-resolved. While this is a reasonable first approach, future works should verify the validity of this study and establish connections between the noise-generating frequencies and the integral, frequency-averaged results that are two-point correlations.

An interesting idea for the location of the radiator surface was proposed by a faculty member of the Department of Mechanical and Aerospace Engineering, by which the surface could be located using RANS based on the dissipation field instead of the vorticity field. Evidently, the two variables are related physically, but two-equation models for RANS may be able to capture better the outer edge of turbulence in terms of dissipation rather than direct vorticity.

Finally, the implementation of the knowledge gained during this work into a more complete wavepacket model is still left to do. The basic elements are laid out in Section 5, but it is a simple, deterministic approach that considers only the axisymmetric mode. The stochastic nature of turbulence and higher modal components must be considered to model the jet noise generation at higher angles than the direction of peak noise radiation [76]. Further, this work emphasizes the need for a new method of determining the central location of the wavepackets, after the dimensional construct  $\epsilon/k$  on the OSPS was deemed inaccurate.

# Bibliography

- [1] A. Adam, D. Papamoschou, and C. Bogey. The imprint of vortical structures on the pressure field at the edge of a turbulent high-speed jet. *AIAA Scitech 2021 Forum*, 2021. doi:10.2514/6.2021-1184.
- [2] A. Adam, D. Papamoschou, J. Xiong, and F. Liu. The very near pressure field of three-stream jets. *AIAA Aerospace Sciences Meeting, 2018*, 2018. doi:10.2514/6.2018-1739.
- [3] A. Adam, D. Papamoschou, J. Xiong, and F. Liu. Vorticity dynamics and flow statistics near the edge of high-speed multi-stream jets. *AIAA Scitech 2019 Forum*, 2019. doi:10.2514/6.2019-1303.
- [4] R. E. Arndt, D. F. Long, and M. N. Glauser. The proper orthogonal decomposition of pressure fluctuations surrounding a turbulent jet. *Journal of Fluid Mechanics*, 340:1–33, 6 1997. doi:10.1017/S0022112097005089.
- [5] P. K. Banerjee. *The Boundary Element Methods in Engineering*. McGraw-Hill, 1994.
- [6] M. Basner, C. Clark, A. Hansell, J. Hileman, S. Janssen, K. Shepherd, and V. Sparrow. Aviation Noise Impacts: State of the Science. *Noise & Health*, 19(87):41, 3 2017. doi:10.4103/NAH.NAH.104.16.
- [7] G. K. Batchelor. *An Introduction to Fluid Dynamics*. Cambridge University Press, 2 2000. doi:10.1017/CBO9780511800955.
- [8] C. Bogey. Grid Sensitivity of Flow Field and Noise of High-Reynolds-number Jets Computed by Large-Eddy Simulation. *International Journal of Aeroacoustics*, 17(4-5):399–424, 2018. doi:10.1177/1475472X18778287.
- [9] C. Bogey. On noise generation in low Reynolds number temporal round jets at a Mach number of 0.9. *Journal of Fluid Mechanics*, 859:1022–1056, 1 2019. doi:10.1017/JFM.2018.864.
- [10] C. Bogey. Two-dimensional features of correlations in the flow and near pressure fields of mach number 0.9 jets. *AIAA Scitech 2019 Forum*, 2019. doi:10.2514/6.2019-0806.
- [11] C. Bogey. Acoustic tones in the near-nozzle region of jets: characteristics and variations between Mach numbers 0.5 and 2. *Journal of Fluid Mechanics*, 921:A3, 2021. doi:10.1017/jfm.2021.426.

- [12] C. Bogey. Generation of Excess Noise by Jets with Highly Disturbed Laminar Boundary-Layer Profiles. *AIAA Journal*, 59(2):569–579, 2021. doi:10.2514/1.J059610.
- [13] C. Bogey and C. Bailly. A Family of Low Dispersive and Low Dissipative Explicit Schemes for Flow and Noise Computations. *Journal of Computational Physics*, 194(1):194 – 214, 2004. doi:10.1016/j.jcp.2003.09.003.
- [14] C. Bogey and C. Bailly. Large Eddy Simulations of Transitional Round Jets: Influence of the Reynolds Number on Flow Development and Energy Dissipation. *Physics of Fluids*, 18(6):65101, 2006. doi:10.1063/1.2204060.
- [15] C. Bogey and C. Bailly. Turbulence and Energy Budget in a Self-Preserving Round Jet: Direct Evaluation Using Large Eddy Simulation. *Journal of Fluid Mechanics*, 627:129–160, 2009. doi:10.1017/S0022112009005801.
- [16] C. Bogey, C. Bailly, and D. Juvé. Noise Investigation of a High Subsonic, Moderate Reynolds Number Jet Using a Compressible Large Eddy Simulation. *Theoretical and Computational Fluid Dynamics 2002 16:4*, 16(4):273–297, 3 2003. doi:10.1007/S00162-002-0079-4.
- [17] C. Bogey, N. de Cacqueray, and C. Bailly. A Shock-Capturing Methodology Based on Adaptive Spatial Filtering for High-Order Non-Linear Computations. *Journal of Computational Physics*, 228(5):1447 – 1465, 2009. doi:10.1016/j.jcp.2008.10.042.
- [18] C. Bogey, N. de Cacqueray, and C. Bailly. Finite Differences for Coarse Azimuthal Discretization and for Reduction of Effective Resolution Near Origin of Cylindrical Flow Equations. *Journal of Computational Physics*, 230(4):1134 – 1146, 2011. doi:10.1016/j.jcp.2010.10.031.
- [19] C. Bogey and O. Marsden. Identification of the Effects of the Nozzle-Exit Boundary-Layer Thickness and Its Corresponding Reynolds Number in Initially Highly Disturbed Subsonic Jets. *Physics of Fluids*, 25(5):55106, 2013. doi:10.1063/1.4807071.
- [20] C. Bogey, O. Marsden, and C. Bailly. Large-eddy simulation of the flow and acoustic fields of a Reynolds number 105 subsonic jet with tripped exit boundary layers. *Physics of Fluids*, 23(3):035104, 3 2011. doi:10.1063/1.3555634.
- [21] C. Bogey, O. Marsden, and C. Bailly. Effects of Moderate Reynolds Numbers on Subsonic Round Jets With Highly Disturbed Nozzle-Exit Boundary Layers. *Physics of Fluids*, 24(10):105107, 2012. doi:10.1063/1.4757667.
- [22] C. Bogey, O. Marsden, and C. Bailly. Influence of Initial Turbulence Level on the Flow and Sound Fields of a Subsonic Jet at a Diameter-Based Reynolds Number of  $10^5$ . *Journal of Fluid Mechanics*, 701:352–385, 2012. doi:10.1017/jfm.2012.162.
- [23] C. Bogey and R. Sabatini. Effects of Nozzle-Exit Boundary-Layer Profile on the Initial Shear-Layer Instability, Flow Field and Noise of Subsonic Jets. *Journal of Fluid Mechanics*, 876:288–325, 2019. doi:10.1017/jfm.2019.546.

- [24] J. Bridges. Rapid prediction of installed jet noise from RANS. *25th AIAA/CEAS Aeroacoustics Conference, 2019*, 2019. doi:10.2514/6.2019-2732.
- [25] J. E. Bridges and M. P. Wernet. Measurements of Turbulent Convection Speeds in Multistream Jets Using Time-Resolved PIV. *AIAA Paper 2017-4041*, 6 2017. doi:10.2514/6.2017-4041.
- [26] C. Brown, J. Bridges, and B. Henderson. Offset stream technology test - Summary of results. *13th AIAA/CEAS Aeroacoustics Conference (28th AIAA Aeroacoustics Conference)*, 2007. doi:10.2514/6.2007-3664.
- [27] G. L. Brown and A. Roshko. On density effects and large structure in turbulent mixing layers. *Journal of Fluid Mechanics*, 64(4):775–816, 1974. doi:10.1017/S002211207400190X.
- [28] R. Camussi and C. Bogey. Intermittent Statistics of the 0-Mode Pressure Fluctuations in the Near Field of Mach 0.9 Circular Jets at Low and High Reynolds Numbers. *Theoretical and Computational Fluid Dynamics*, 35(2):229–247, 4 2021. doi:10.1007/s00162-020-00553-9.
- [29] A. V. Cavalieri, P. Jordan, and L. Lesshafft. Wave-packet models for jet dynamics and sound radiation. *Applied Mechanics Reviews*, 71(2), 3 2019. doi:10.1115/1.4042736/726704.
- [30] A. V. G. Cavalieri, P. Jordan, T. Colonius, and Y. Gervais. Axisymmetric Superdirectivity in Subsonic jets. *Journal of Fluid Mechanics*, 704:388–420, 2012. doi:10.1017/jfm.2012.247.
- [31] F. H. Champagne. The fine-scale structure of the turbulent velocity field. *J. Fluid Mech*, 86(1):67–108, 2022. doi:10.1017/S0022112078001019.
- [32] F. Coiffet, P. Jordan, J. Delville, Y. Gervais, and F. Ricaud. Coherent Structures in Subsonic Jets: A Quasi-Irrotational Source Mechanism? *International Journal of Aeroacoustics*, 5(1):67–89, 2006. doi:10.1260/147547206775220407.
- [33] D. Crighton and P. Huerre. Shear-layer pressure fluctuations and superdirective acoustic sources. *Journal of Fluid Mechanics*, 220:355–368, 1990. doi:10.1017/S0022112090003299.
- [34] S. C. Crow and F. H. Champagne. Orderly structure in jet turbulence. *Journal of Fluid Mechanics*, 48(3):547–591, 8 1971. doi:10.1017/S0022112071001745.
- [35] M. D. Dahl. Turbulent statistics from time-resolved piv measurements of a jet using empirical mode decomposition. *18th AIAA/CEAS Aeroacoustics Conference (33rd AIAA Aeroacoustics Conference)*, 2012. doi:10.2514/6.2012-2297.
- [36] K. A. Daniel, D. E. Mayo, K. Todd Lowe, and W. F. Ng. Use of thermal nonuniformity to reduce supersonic jet noise. *AIAA Journal*, 57(10):4467–4475, 9 2019. doi:10.2514/1.J058531/ASSET/IMAGES/LARGE/FIGURE5.JPEG.

- [37] A. Darisse, J. Lemay, and A. Benaïssa. Budgets of Turbulent Kinetic Energy, Reynolds Stresses, Variance of Temperature Fluctuations and Turbulent Heat Fluxes in a Round Jet. *Journal of Fluid Mechanics*, 774:95–142, 2015. doi:10.1017/jfm.2015.245.
- [38] D. Fauconnier, C. Bogey, and E. Dick. On the Performance of Relaxation Filtering for Large-Eddy Simulation. *Journal of Turbulence*, 14(1):22–49, 2013. doi:10.1080/14685248.2012.740567.
- [39] M. J. Fisher, G. A. Preston, and W. D. Bryce. A Modelling of the Noise from Simple Coaxial Jets, Part I: With Unheated Primary Flow. *Journal of Sound and Vibration*, 209(3):385–403, 1998. doi:10.1006/jsvi.1997.1218.
- [40] V. Fleury, C. Bailly, E. Jondeau, M. Michard, and D. Juvé. Space-Time Correlations in Two Subsonic Jets Using Dual Particle Image Velocimetry Measurements. *AIAA Journal*, 46(10):2498–2509, 2008. doi:10.2514/1.35561.
- [41] J. E. F. Fowcs and W. Illiams. The noise from turbulence convected at high speed. *Philosophical Transactions of the Royal Society of London. Series A, Mathematical and Physical Sciences*, 255(1061):469–503, 4 1963. doi:10.1098/RSTA.1963.0010.
- [42] K. L. Gee, T. B. Neilsen, and A. A. Atchley. Skewness and shock formation in laboratory-scale supersonic jet data. *Journal of the Acoustical Society of America*, 133(6):EL491–EL497, 6 2013. doi:10.1121/1.4807307.
- [43] N. J. Georgiadis and J. R. DeBonis. Navier-Stokes Analysis Methods for Turbulent Jet Flows with Application to Aircraft Exhaust Nozzles. *Progress in Aerospace Sciences*, 42:378–418, 2006. doi:10.1016/j.paerosci.2006.12.001.
- [44] M. Harper-Bourne. Jet noise turbulence measurements. *9th AIAA/CEAS Aeroacoustics Conference and Exhibit*, 2003. doi:10.2514/6.2003-3214.
- [45] Q. He, C. Wollersheim, M. Locke, and I. Waitz. Estimation of the global impacts of aviation-related noise using an income-based approach. *Transport Policy*, 34:85–101, 7 2014. doi:10.1016/J.TRANPOL.2014.02.020.
- [46] B. Henderson. Aeroacoustics of three-stream jets. *18th AIAA/CEAS Aeroacoustics Conference (33rd AIAA Aeroacoustics Conference)*, 2012. doi:10.2514/6.2012-2159.
- [47] B. Henderson and D. Huff. The aeroacoustics of offset three-stream jets for future commercial supersonic aircraft. *22nd AIAA/CEAS Aeroacoustics Conference, 2016*, 2016. doi:10.2514/6.2016-2992.
- [48] B. Henderson, S. J. Leib, and M. Wernet. Measurements and predictions of the noise from three-stream jets. *21st AIAA/CEAS Aeroacoustics Conference*, 2015. doi:10.2514/6.2015-3120.
- [49] D. L. Huff, B. S. Henderson, J. J. Berton, and J. A. Seidel. Perceived noise analysis for offset jets applied to commercial supersonic aircraft. *54th AIAA Aerospace Sciences Meeting*, 2016. doi:10.2514/6.2016-1635.

- [50] ICAO Secretariat. Environmental Report. Technical report, International Civil Aviation Organization, 2019.
- [51] A. Jameson, W. Schmidt, and E. Turkel. Numerical solution of the Euler equations by finite volume methods using Runge Kutta time stepping schemes. *14th Fluid and Plasma Dynamics Conference*, 6 1981. doi:10.2514/6.1981-1259.
- [52] P. Jordan and T. Colonius. Wave Packets and Turbulent Jet Noise. *Annual Review of Fluid Mechanics*, 45:173–195, 9 2013. doi:10.1146/annurev-fluid-011212-140756.
- [53] M. Kaltenbach, C. Maschke, and R. Klinke. Health Consequences of Aircraft Noise. *Deutsches Ärzteblatt International*, 105(31-32):548, 8 2008. doi:10.3238/ARZTEBL.2008.0548.
- [54] F. Kerhervé, J. Fitzpatrick, and P. Jordan. The frequency dependence of jet turbulence for noise source modelling. *Journal of Sound and Vibration*, 296(1):209 – 225, 2006. doi:10.1016/j.jsv.2006.02.012.
- [55] F. Kremer and C. Bogey. Large-Eddy Simulation of Turbulent Channel Flow Using Relaxation Filtering: Resolution Requirement and Reynolds Number Effects. *Computers & Fluids*, 116:17 – 28, 2015. doi:10.1016/j.compfluid.2015.03.026.
- [56] J. C. Lau, P. J. Morris, and M. J. Fisher. Measurements in subsonic and supersonic free jets using a laser velocimeter. *Journal of Fluid Mechanics*, 93(1):1–27, 1979. doi:10.1017/S0022112079001750.
- [57] S. J. Leib. Modeling Sound Propagation Through Non-Axisymmetric Jets. *NASA/CR-2014-218107*, 3 2014.
- [58] M. J. Lighthill. On sound generated aerodynamically I. General theory. *Proceedings of the Royal Society of London. Series A. Mathematical and Physical Sciences*, 211(1107):564–587, 3 1952. doi:10.1098/RSPA.1952.0060.
- [59] G. Lilley. On the noise from air jets. *Noise Mechanisms, AGARD CP*, 131:1–13, 1974.
- [60] Y. Liu. Fast Multipole Boundary Element Method: Theory and Applications in Engineering. *Fast Multipole Boundary Element Method: Theory and Applications in Engineering*, 9780521116596:1–235, 1 2009. doi:10.1017/CBO9780511605345.
- [61] I. A. Maia, P. Jordan, A. V. Cavalieri, and V. Jaunet. Two-point wavepacket modelling of jet noise. *Proceedings of the Royal Society A*, 475(2227), 7 2019. doi:10.1098/RSPA.2019.0199.
- [62] J. Mathieu and J. Scott. *An Introduction to Turbulent Flow*. Cambridge University Press, 6 2000. doi:10.1017/CBO9781316529850.
- [63] MATLAB. *9.9.0.1467703 (R2020b)*. The MathWorks Inc., Natick, Massachusetts, 2020.

- [64] D. K. McLaughlin, G. L. Morrison, and T. R. Troutt. Experiments on the instability waves in a supersonic jet and their acoustic radiation. *Journal of Fluid Mechanics*, 69(1):73–95, 1975. doi:10.1017/S0022112075001322.
- [65] S. Mendez, M. Shoeybi, S. Lele, and P. Moin. On the Use of the Ffowcs Williams-Hawkins Equation to Predict Far-Field Jet Noise from Large-Eddy Simulations. *International Journal of Aeroacoustics*, 12(1-2):1–20, 6 2013. doi:10.1260/1475-472X.12.1-2.1.
- [66] F. R. Menter. Two-Equation Eddy-Viscosity Turbulence Models for Engineering Applications. *AIAA Journal*, 32(8):1598–1605, 1994. doi:10.2514/3.12149.
- [67] D. C. Mincu, E. Manoha, C. Parzani, J. Chappuis, S. Redonnet, R. Davy, and M. Escoufflaire. Numerical and experimental characterization of aft - Fan noise for isolated and installed configurations. *16th AIAA/CEAS Aeroacoustics Conference (31st AIAA Aeroacoustics Conference)*, 2010. doi:10.2514/6.2010-3918.
- [68] K. Mohseni and T. Colonius. Numerical Treatment of Polar Coordinate Singularities. *Journal of Computational Physics*, 157(2):787 – 795, 2000. doi:10.1006/jcph.1999.6382.
- [69] B. R. Molesworth and M. Burgess. Improving intelligibility at a safety critical point: In flight cabin safety. *Safety Science*, 51(1):11–16, 1 2013. doi:10.1016/J.SSCI.2012.06.006.
- [70] P. J. Morris. A Note on Noise Generation by Large Scale Turbulent Structures in Subsonic and Supersonic Jets. *International Journal of Aeroacoustics*, 8(4):301–316, 2009. doi:10.1260/147547209787548921.
- [71] P. J. Morris and K. Zaman. Velocity Measurements in Jets with Application to Jet Noise. *Journal of Sound and Vibration*, 329:394–414, 2010. doi:10.1016/j.jsv.2009.09.024.
- [72] D. Papamoschou. New Method for Jet Noise Reduction in Turbofan Engines. *AIAA Journal*, 42(11):2245–2253, 5 2004. doi:10.2514/1.4788.
- [73] D. Papamoschou. Prediction of jet noise shielding. *48th AIAA Aerospace Sciences Meeting Including the New Horizons Forum and Aerospace Exposition*, 2010. doi:10.2514/6.2010-653.
- [74] D. Papamoschou. Modelling of Noise Reduction in Complex Multistream Jets. *Journal of Fluid Mechanics*, 834:555–599, 1 2018. doi:10.1017/jfm.2017.730.
- [75] D. Papamoschou. On the Connection Between Near and Far Pressure Fields of a Turbulent Jet. *AIAA Paper 2018-1251*, 1 2018. doi:10.2514/6.2018-1251.
- [76] D. Papamoschou. Wavepacket Modeling of the Jet Noise Source. *International Journal of Aeroacoustics*, 17(1-2):52–69, 2 2018. doi:10.1177/1475472X17743653.

- [77] D. Papamoschou and M. Debiasi. Directional Suppression of Noise from a High-Speed Jet. *AIAA Journal*, 39(3):380–387, 2001. doi:10.2514/2.1345.
- [78] D. Papamoschou and S. Mayoral. Modeling of jet noise sources and their diffraction with uniform flow. *51st AIAA Aerospace Sciences Meeting including the New Horizons Forum and Aerospace Exposition 2013*, 2013. doi:10.2514/6.2013-326.
- [79] D. Papamoschou and V. Phong. The Very Near Pressure Field of Single- and Multi-Stream Jets. *AIAA Paper 2017-0230*, 1 2017. doi:10.2514/6.2017-0230.
- [80] D. Papamoschou and V. Phong. Perceived Noise Assessment of Offset Three-Stream Nozzles for Low Noise Supersonic Aircraft. *AIAA Paper 2018-1740*, 1 2018. doi:10.2514/6.2018-1740.
- [81] D. Papamoschou, V. Phong, J. Xiong, and F. Liu. Quiet nozzle concepts for three-stream jets. *54th AIAA Aerospace Sciences Meeting*, 2016. doi:10.2514/6.2016-0523.
- [82] D. Papamoschou and S. Rostamimonjezi. Effect of Velocity Ratio on Noise Source Distribution of Coaxial Jets. *AIAA Journal*, 48(7):1504–1512, 2010. doi:10.2514/1.J050140.
- [83] D. Papamoschou, J. Xiong, and F. Liu. Towards a low-cost wavepacket model of the jet noise source. *53rd AIAA Aerospace Sciences Meeting*, 2015. doi:10.2514/6.2015-1006.
- [84] V. Phong and D. Papamoschou. Investigation of isolated and installed three-stream jets from offset nozzles. In *AIAA SciTech Forum - 55th AIAA Aerospace Sciences Meeting*. American Institute of Aeronautics and Astronautics Inc., 2017. doi:10.2514/6.2017-0005.
- [85] S. Piantanida, V. Jaunet, J. Huber, W. R. Wolf, P. Jordan, and A. V. G. Cavalieri. Scattering of Turbulent-Jet Wavepackets by a Swept Trailing Edge. *Journal of the Acoustical Society of America*, 140(6):4350–4359, 2016. doi:10.1121/1.4971425.
- [86] C. Picard and J. Delville. Pressure Velocity Coupling in a Subsonic Round Jet. *International Journal of Heat and Fluid Flow*, 21(3):359 – 364, 2000. doi:10.1016/S0142-727X(00)00021-7.
- [87] E. Pickering, G. Rigas, P. A. Nogueira, A. V. Cavalieri, O. T. Schmidt, and T. Colonius. Lift-up, Kelvin–Helmholtz and Orr mechanisms in turbulent jets. *Journal of Fluid Mechanics*, 896, 2020. doi:10.1017/JFM.2020.301.
- [88] P. Pineau and C. Bogey. Study of the generation of shocks by high-speed jets using conditional averaging. *2018 AIAA/CEAS Aeroacoustics Conference*, 2018. doi:10.2514/6.2018-3305.
- [89] C. D. Pokora and J. J. McGuirk. Stereo-PIV Measurements of Spatio-Temporal Turbulence Correlations in an Axisymmetric Jet. *Journal of Fluid Mechanics*, 778:216–252, 2015. doi:10.1017/jfm.2015.362.

- [90] S. B. Pope. *Turbulent Flows*. Cambridge University Press, 8 2000. doi:10.1017/CBO9780511840531.
- [91] R. W. Powers, D. K. McLaughlin, and P. J. Morris. Noise reduction with fluidic inserts in supersonic jets exhausting over a simulated aircraft carrier deck. *21st AIAA/CEAS Aeroacoustics Conference*, 2016. doi:10.2514/6.2015-2374.
- [92] A. Proença, J. Lawrence, and R. Self. Measurements of the Single-Point and Joint Turbulence Statistics of High Subsonic Jets Using Hot-Wire Anemometry. *Experiments in Fluids*, 60(63), 3 2019. doi:10.1007/s00348-019-2716-3.
- [93] R. Reba, S. Narayanan, and T. Colonius. Wave-Packet Models for Large-Scale Mixing Noise. *International Journal of Aeroacoustics*, 9:533–558, 2010. doi:10.1260/1475-472X.9.4-5.533.
- [94] P. L. Roe. Approximate Riemann Solvers, Parameter Vectors and Difference Schemes. *Journal of Computational Physics*, 46(2):357–378, 1980. doi:10.1016/0021-9991(81)90128-5.
- [95] M. Samimy, J. H. Kim, J. Kastner, I. Adamovich, and Y. Utkin. Active Control of a Mach 0.9 Jet for Noise Mitigation Using Plasma Actuators. *AIAA Journal*, 45(4):890–901, 5 2007. doi:10.2514/1.27499.
- [96] O. T. Schmidt, A. Towne, G. Rigas, T. Colonius, and G. A. Brès. Spectral analysis of jet turbulence. *Journal of Fluid Mechanics*, 855:953–982, 11 2018. doi:10.1017/JFM.2018.675.
- [97] J. M. Seiner. Advances in High Speed Jet Aeroacoustics. *AIAA Paper*, 1984. doi:10.2514/6.1984-2275.
- [98] M. L. Shur, P. R. Spalart, and M. K. Strelets. Noise Prediction for Increasingly Complex Jets. Part I: Methods and Tests. *International Journal of Aeroacoustics*, 4(3):213–246, 2005. doi:10.1260/1475472054771376.
- [99] R. J. Simmons. *Design and Control of a Variable Geometry Turbofan with an Independently Modulated Third Stream*. PhD thesis, Ohio State University, Columbus, OH, 2009.
- [100] P. R. Spalart and S. R. Allmaras. A One-Equation Turbulence Model for Aerodynamic Flows. *AIAA Paper 1992-0439*, 1 1992. doi:10.2514/6.1992-439.
- [101] P. R. Spalart, W. H. Jou, M. Strelets, and S. R. Allmaras. Comments on the Feasibility of LES for Wings, and on a Hybrid RANS/LES Approach. In *AFOSR international conference on DNS/LES*, 1st AFOSR Int. Conf. on DNS/LES, Ruston, LA, 8 1997.
- [102] M. Stuber, K. T. Lowe, and F. N. Wing. Synthesis of Convection Velocity and Turbulence Measurements in Three-Stream Jets. *Experiments in Fluids*, 60(83):998–1001, 2019. doi:10.1007/s00348-019-2730-5.

- [103] C. K. Tam. Supersonic Jet Noise. *Annual Review of Fluid Mechanics*, 27(1):17–43, 11 1995. doi:10.1146/ANNUREV.FL.27.010195.000313.
- [104] C. K. Tam. Influence of Nozzle Geometry on the Noise of High-Speed Jets. *AIAA Journal*, 36(8):1396–1400, 5 1998. doi:10.2514/2.560.
- [105] C. K. Tam. Mach Wave Radiation from High-Speed Jets. *AIAA Journal*, 47(10):2440–2448, 5 2009. doi:10.2514/1.42644.
- [106] C. K. Tam, K. Viswanathan, K. K. Ahuja, and J. Panda. The sources of jet noise: experimental evidence. *Journal of Fluid Mechanics*, 615:253–292, 2008. doi:10.1017/S0022112008003704.
- [107] C. K. W. Tam and Z. Dong. Radiation and Outflow Boundary Conditions for Direct Computation of Acoustic and Flow Disturbances in a Nonuniform Mean Flow. *Journal of Computational Acoustics*, 04(02):175–201, 1996. doi:10.1142/S0218396X96000040.
- [108] C. K. W. Tam, N. N. Pastouchenko, and K. Viswanathan. Extension of the Near Acoustic Field of a Jet to the Far Field. *Procedia Engineering*, 6:9–18, 10 2010. doi:10.1016/j.proeng.2010.09.002.
- [109] J. K. Tanna and P. J. Morris. The Noise from Normal-Velocity-Profile Coannular Jets. *Journal of Sound and Vibration*, 98(2):213–234, 1985. doi:10.1016/0022-460X(85)90386-4.
- [110] C. E. Tinney and P. Jordan. The Near Pressure Field of Co-axial Subsonic Jets. *Journal of Fluid Mechanics*, 611:175–204, 9 2008. doi:10.1017/S0022112008001833.
- [111] D. Violato and F. Scarano. Three-Dimensional Vortex Analysis and Aeroacoustic Source Characterization of Jet Core Breakdown. *Physics of Fluids*, 25(1):15112, 2013. doi:10.1063/1.4773444.
- [112] K. Viswanathan. Aeroacoustics of hot jets. *Journal of Fluid Mechanics*, 516:39–82, 10 2004. doi:10.1017/S0022112004000151.
- [113] K. Viswanathan. Mechanisms of Jet Noise Generation: Classical Theories and Recent Developments. *International Journal of Aeroacoustics*, 8(4):355–407, 6 2009. doi:10.1260/147547209787548949.
- [114] J. Xiong, F. Liu, and D. Papamoschou. Large eddy simulation of three-stream jets. *AIAA Aerospace Sciences Meeting, 2018*, 2018. doi:10.2514/6.2018-1737.
- [115] J. Xiong, P. Nielsen, F. Liu, and D. Papamoschou. Computation of High-Speed Coaxial Jets with Fan Flow Deflection. *AIAA Journal*, 48(10):2249–2262, 2010. doi:10.2514/1.J050331.
- [116] K. B. M. Q. Zaman. Effect of Initial Condition on Subsonic Jet Noise. *AIAA Journal*, 23(9):1370–1373, 1985. doi:10.2514/3.9094.

- [117] J. Zhou, R. J. Adrian, S. Balachandar, and T. M. Kendall. Mechanisms for generating coherent packets of hairpin vortices in channel flow. *Journal of Fluid Mechanics*, 387:353–396, 5 1999. doi:10.1017/S002211209900467X.

# Appendix A

## Noise Propagation through the Boundary Element Method

### A.1 Fundamentals of the Boundary Element Method

The boundary element method (BEM) is a computational method for solving linear partial differential equations which can be written into integral equations [5]. In this work, BEM is used to solve the inhomogeneous wave equation for pressure  $p'$

$$\frac{1}{a_\infty^2} \frac{\partial^2 p'}{\partial t^2} - \nabla^2 p' = S(\mathbf{y}, \tau) \quad (\text{A.1})$$

where  $S$  is a noise source located at coordinates  $\mathbf{y}$  emitting at time  $\tau$ . For harmonic problems, with  $e^{-i\omega t}$  convention, the pressure fluctuation will have the form  $p'(\mathbf{x}, t) = \mathcal{P}(\mathbf{x}, \omega)e^{-i\omega t}$ , where  $\mathcal{P}$  is a complex sound pressure function in the frequency domain. With this harmonic assumption, Eq. A.1 becomes the Helmholtz equation

$$\nabla^2 \mathcal{P} + \kappa_\infty^2 \mathcal{P} = S(\mathbf{y}, \omega) \quad (\text{A.2})$$

where  $\kappa_\infty = \omega/a_\infty$  is the acoustic wavenumber.

The BEM allows solving for  $\mathcal{P}$  for scattering and radiating problems by considering a body of surface  $S$ , as shown in Fig. A.1. The body's surface  $S$  is a closed surface. Outside the body, there may be an incident known pressure field  $\mathcal{P}_i(\mathbf{x})$ . The Helmholtz equation can be transformed to a surface integral equation [60] named the Kirchhoff-Helmholtz integral

$$c(\mathbf{x})\mathcal{P}(\mathbf{x}) = \int_S \left[ \frac{\partial \mathcal{P}(\mathbf{y})}{\partial n} G(\mathbf{x}, \mathbf{y}) - \mathcal{P}(\mathbf{y}) \frac{\partial G(\mathbf{x}, \mathbf{y})}{\partial n} \right] d^2\mathbf{y} + \mathcal{P}_i(\mathbf{x}) \quad (\text{A.3})$$

where  $G(\mathbf{x}, \mathbf{y})$  is the free-space Green's function

$$G(\mathbf{x}, \mathbf{y}) = \frac{1}{4\pi r_d}, \quad r_d = |\mathbf{x} - \mathbf{y}| \quad (\text{A.4})$$

The constant  $c(\mathbf{x})$  is  $c(\mathbf{x}) = 1/2$  on a smooth surface  $S$ , and  $c(\mathbf{x}) = 1$  on the exterior of the surface. The term  $\frac{\partial \mathcal{P}}{\partial n}$  is the normal derivative of  $\mathcal{P}$ , which is related to the normal velocity  $v_n$  of the flow field

$$v_n = \frac{1}{i\omega\rho} \frac{\partial \mathcal{P}}{\partial n} \quad (\text{A.5})$$

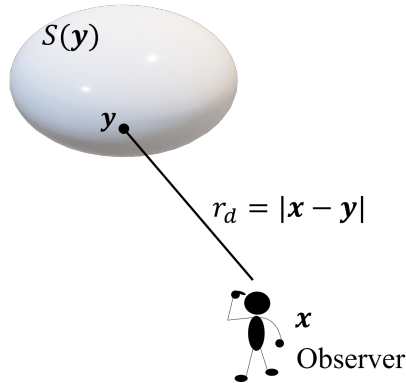


Figure A.1: Sketch of BEM surface and observer references.

Equation A.3 is solved by BEM as follows. For radiation problems, the normal derivative  $\frac{\partial \mathcal{P}}{\partial n}$  is unknown at the surface, but  $\mathcal{P}$  is known there. The surface  $S$  is discretized into  $N$  elements and  $\mathbf{x}$  is taken at the surface, each element  $j$  contains the equation

$$\frac{1}{2}\mathcal{P}_j = \sum_{k=1}^N \left[ i\omega\rho v_{n_k} G(\mathbf{x}_j, \mathbf{x}_k) - \mathcal{P}_k \frac{\partial G(\mathbf{x}_j, \mathbf{x}_k)}{\partial n} \right] + \mathcal{P}_{i_j} \quad (\text{A.6})$$

in which the normal velocity  $v_{n_k}$  is the only unknown. It is then simple to group the  $N$  equations at the surface and solve for  $v_n$  with a linear system of equations. This is the type of problems we will be solving with BEM, where the radiator surface acts as a radiating body containing the wavepacket, and there are no other incident fields  $\mathcal{P}_i = 0$ .

The convenience of BEM is that, for an acoustic wave problem where the geometry of the radiating body is fixed, we can compute an acoustic transfer matrix (ATM) to quickly recalculate the sound field for different  $\mathcal{P}$  distributions at the surface, i.e. the ATM must be calculated only once for a given wavepacket shape and frequency, and it is valid for all wavepacket shapes. The formulation of the ATM relies on the fact that the relation between normal velocity and pressure of Eqn. A.6 is linear. Express the set of discretized flow field variables  $v_n$  and  $\mathcal{P}$  at the surface  $S$  as  $\mathbf{v}_{n_S}$  and  $\mathcal{P}_S$  respectively. These sets are related through two coefficient matrices  $\mathbf{F}_S$  and  $\mathbf{G}_S$  as

$$\mathbf{F}_S \mathcal{P}_S = \mathbf{G}_S \mathbf{v}_{n_S} \quad (\text{A.7})$$

Similarly, the discretized form of Eqn. A.3 for a point on the field,  $f$ , can be expressed with coefficient matrices  $\mathbf{F}_f$  and  $\mathbf{G}_f$  and no incident field as

$$\mathcal{P}_f = \mathbf{G}_f \mathbf{v}_{n_S} + \mathbf{F}_f \mathcal{P}_S \quad (\text{A.8})$$

Equations A.7 and A.8 are then combined to define the acoustic matrix  $T$

$$\mathcal{P}_f = [\mathbf{G}_f \mathbf{G}_S^{-1} \mathbf{F}_S - \mathbf{F}_f] \mathcal{P}_S \equiv \mathbf{T} \mathcal{P}_S \quad (\text{A.9})$$

The coefficient matrices remain constant as long as the radiating surface, field points, and frequency remain constant. Therefore, the acoustic transfer matrix  $\mathbf{T}$ , even though it is computationally expensive, serves to quickly calculate the pressure field for any wavepacket shape, which is very convenient for the calibration of the model parameters of the reference jet explained in section 5.2.

## A.2 Software Validation

If the radiator surface were a cylinder of radius  $r_0$  and has a wavepacket prescribed as Eq. 5.2, the pressure field for a radius  $r \geq r_0$  can be computed analytically. This solution is used here to verify the BEM software and methodology.

### A.2.1 Propagation from a radiating cylinder

Denote the spatial Fourier transform of the wavepacket shape  $p_0(x, \omega)$  as  $\hat{p}_0(x, \kappa)$ . The field pressure induced by an axisymmetric wavepacket of given  $\omega$  is [70]

$$p_{wp}(x, r, t) = \frac{1}{2\pi} e^{-i\omega t} \int_{-\infty}^{\infty} \hat{p}_0(\kappa) \frac{H_0^{(1)}(\lambda r)}{H_0^{(1)}(\lambda r_0)} e^{i\kappa x} d\kappa \quad (\text{A.10})$$

$$\lambda = \left[ \left( \frac{\omega^2}{a_\infty^2} - \kappa^2 \right) \right]^{1/2}, \quad -\frac{\pi}{2} < \arg(\lambda) < \frac{\pi}{2}$$

where  $H_0^{(1)}$  is the Hankel function of the first kind of order 0. Equation A.10 is the exact solution to the linear propagation of pressure outside the cylindrical radiator surface,

and contains radiating and non-radiating components. In the far field, only the radiating components remain. The far-field approximation of Eq. A.10 is[70]

$$p_{wp, far}(R, \theta, t) = -\frac{i}{\pi R} \frac{\hat{p}_0\left(\frac{\omega}{a_\infty} \cos \theta\right)}{H_0^{(1)}\left(\frac{\omega}{a_\infty} r_0 \sin \theta\right)} e^{i\omega R/a_\infty} e^{-i\omega t} \quad (\text{A.11})$$

where  $R$  is the distance of the observer from the origin and  $\theta$  is the polar angle. The modulus square of pressure is the variance of the far-field pressure, or spectrum

$$S_{wp, far}(R, \theta, \omega) = \frac{1}{(\pi R)^2} \left| \frac{\hat{p}_0\left(\frac{\omega}{a_\infty} \cos \theta\right)}{H_0^{(1)}\left(\frac{\omega}{a_\infty} r_0 \sin \theta\right)} \right|^2 \quad (\text{A.12})$$

It should be noted that the exact location of the wavepacket,  $x_0$ , can be neglected when considering far-field propagation. The location of the wavepacket is still relevant when determining the axial shape of the wavepacket, which includes convective velocity and wavepacket length scales.

In this model, the wavepacket shape  $\hat{p}_0$  consists of the Gaussian envelope of Eq. 5.7 and the axial fluctuation dominated by frequency and convective velocity of Eqns. 5.5 and 5.6. Its spatial Fourier transform is

$$\hat{p}_0(\kappa) = \mathcal{A} |L| \sqrt{\pi} \exp\left\{-\frac{L^2}{4} \left(\kappa - \frac{\omega}{U_c}\right)^2\right\} \quad (\text{A.13})$$

Examination of Eqn. A.12 reveals that the far field will only be affected by the wavepacket wavenumbers below  $\kappa \leq \omega/a_\infty$ , i.e., the supersonic components of the wavepacket shape. That, in combination with Eqn. A.13, indicates that the numerator of Eqn. A.12 will only present a local maximum along  $\omega$  or  $\theta$  if the wavepacket is travelling at supersonic speeds relative to the ambient medium,  $U_c > a_\infty$ .

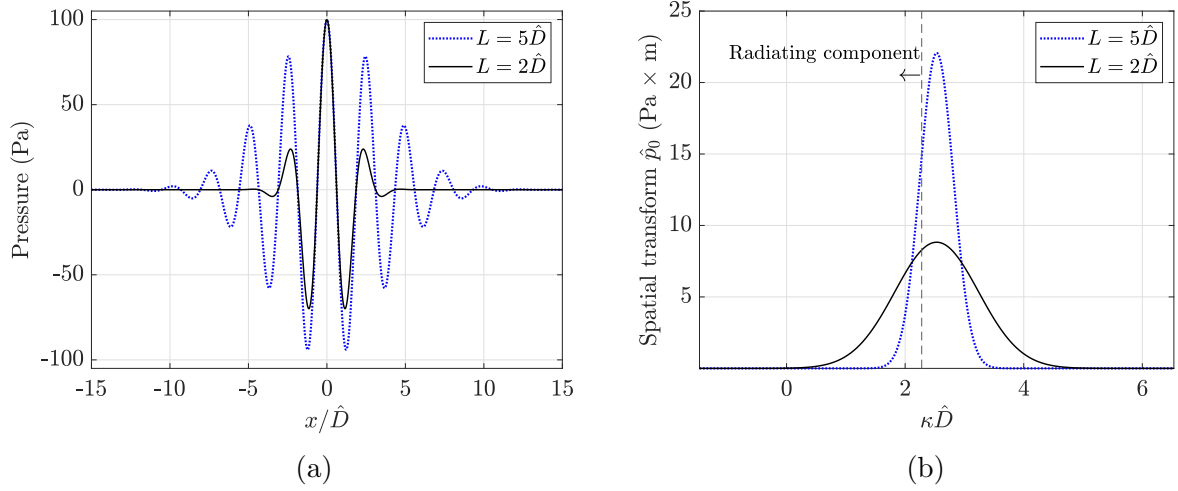


Figure A.2: Examples of wavepacket ansatzes for  $U_c = 0.9a_\infty$  and length scales of 2 and 5  $\hat{D}$ . (a) Real part of the axial distribution  $p_0(x)$ , and (b) Spatial Fourier transform  $\hat{p}_0(\kappa)$

## A.2.2 Validation results

The BEM validation is carried out with a cylinder of radius  $r_0 = \hat{D}/2$  and at a frequency of  $f = 5kHz$ . The BEM element size is  $13.75\lambda_\infty$ , consistent with Table 5.1 and very small. An axisymmetric wavepacket was prescribed following the development of Section 5.1 centered at  $x = 0$ , with an amplitude  $\mathcal{A} = 100$  Pa. In order to capture the general subsonic behavior of the jets of this work but still radiate noise, the convective velocity was set to  $U_c = 0.9a_\infty$ . Several wavepacket length scales, ranging  $0.5 \leq L/\hat{D} \leq 5$ , were applied to test the different radiation patterns generated by the wavepacket envelope of Eqn. A.13. Figure A.2 shows an example of how two wavepacket shapes, of equal parameters except for their length scales, translate into their spatial Fourier transforms. It is evident how shortening the wavepacket length scale “flattens” its spatial Fourier transform and changes the radiating composition, located at  $\kappa \leq \omega/a_\infty$ .

One additional concern is the difference in boundary conditions at  $r = r_0$  of the analytical and BEM solutions. The analytical approach has a set pressure along all of the  $x$ -axis, while the BEM approach only sets the pressure on the surface of the body. The dimensions of

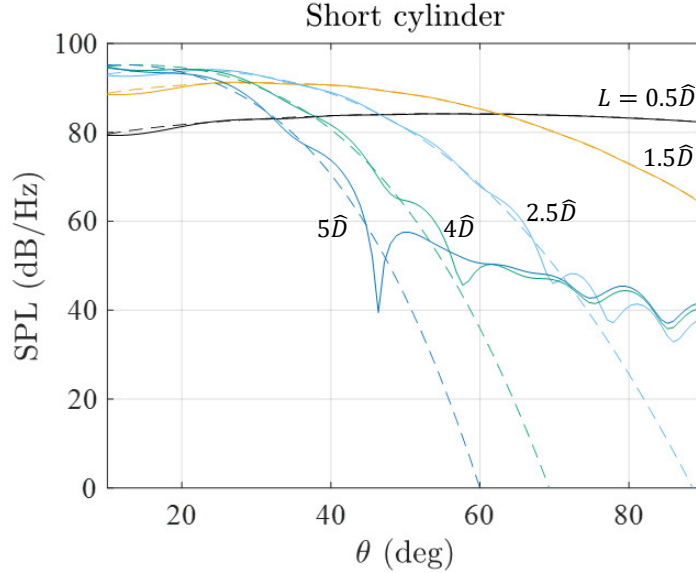


Figure A.3: Sound pressure levels from the standard cylinder BEM computation (solid lines) and the analytic formula (dashed lines) for polar angles  $\theta$  and wavepacket length scales  $L$ . Points are located at  $100\hat{D}$  from the origin.

the radiating surface of the BEM, for the case of a cylinder, have the only condition of properly containing the wavepacket. Given that the radiating surface needs to be meshed, very large surfaces add computational cost and result impractical. For these reasons, the exact dimensions of the radiator surface are arbitrary. We want to test the influence of the size of the radiator surface and the impact of the difference in boundary conditions by testing two different cylinder lengths: short and long. The two cylinders have a radius of  $r_0 = \hat{D}/2$  and are closed by hemispheres.

### Short cylinder

The “short” cylinder has a length spanning  $30\hat{D}$  and is centered at the origin. Figure A.3 compares the noise levels using this cylinder as the radiator surface of the BEM with the theoretical result of Eqn. A.12. The noise levels are taken at a distance of  $100\hat{D}$  from the origin, which is common among all tested cylinders in this work.

It can be observed in Fig. A.3 that low length scales cause more isotropic far-field noise. The length scales of  $0.5\hat{D}$  and  $1.5\hat{D}$  exhibit a very good match between the BEM and the analytical results across all polar angles. With increasing length scales, the SPL curves turn more directional and peak at smaller polar angles. For these directional distributions, the BEM results are accurate for low polar angles and start diverging from the analytical result at  $\theta > 40^\circ$ . For a given length scale, this divergence happens at values more than 20dB below the peak level, so it can be said that the BEM is predicting well the main directions and levels of emissions.

It is clear that the BEM results are physically unrealistic after their divergence from the analytical curves in Fig. A.3. This behavior cannot be due to the short cylinder not containing well the wavepacket shape. The short cylinder presents a length of constant radius of  $15\hat{D}$  on each side of the  $x$ -axis, which is enough to contain a wavepacket of Gaussian envelope and length scale of  $5\hat{D}$  up to levels below 0.1% of its peak value. On the contrary, this behavior is likely to be due to inaccuracies on the BEM calculation or on the boundary conditions defined. We investigate further the noise radiation from the short cylinder by plotting the two-dimensional SPL distribution generated by the wavepacket of  $L = 5\hat{D}$  on a vertical slice, shown in Fig. A.4.

Figure A.4 shows two regions of unusual SPL distribution. The most apparent is that of  $\theta > 45^\circ$ , where the overall SPL levels decrease, and lobes appear. That is the non-physical behavior observed at moderate angles on Fig. A.3. The second region is for very long polar angles,  $\theta \rightarrow 0$ , the emission does not follow the characteristic lobed distribution typical of jet noise, which peaks near  $\theta = 30^\circ$ . Instead, the SPL levels increase when approaching the jet centerline. The influence of the boundary conditions on these two regions is investigated by comparing these results to the case of the long cylinder.

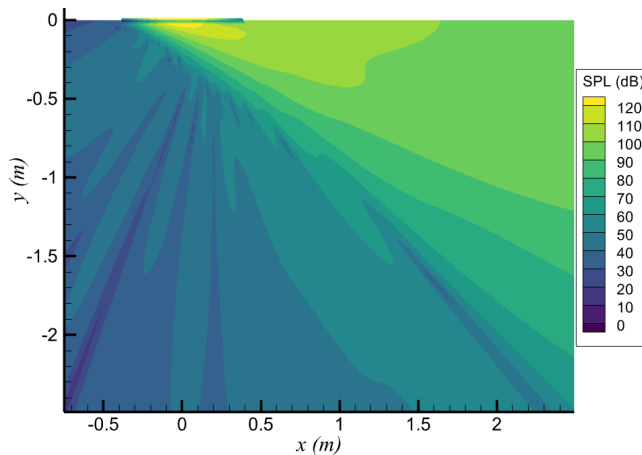


Figure A.4: Sound pressure levels generated from the short cylinder using a wavepacket of length scale  $L = 5\hat{D}$  along the vertical half-plane. The cylinder is visible near  $y = 0$ , spanning from  $x = -0.4$  m to  $x = 0.4$  m.

### Long cylinder

The “short” cylinder has a length spanning from  $x = -15\hat{D}$  to  $x = 100\hat{D}$ . The corresponding sound pressure levels, and their comparison to the analytic results, are shown in Fig. A.6. The field points are taken at  $100\hat{D}$ . Therefore, the pressure boundary condition on the BEM cylinder extends beyond the axial location of those points. It is evident that the BEM results are in very good agreement with the theoretical results and accurately predict the relevant emission levels and directivity of the wavepackets tested. The length scales of  $0.5\hat{D}$  and  $1.5\hat{D}$  show excellent agreement across all of the polar range. The larger length scales show some disagreements at levels near 60 dB below their peak values, and therefore can be considered very minor inaccuracies.

For completeness, we can investigate the origin of the discrepancies between the BEM and theoretical results by plotting the two-dimensional SPL levels along a vertical azimuthal slice generated by a wavepacket of length scale  $L = 5\hat{D}$ , shown on Fig. A.6. The improvement at low polar angles is evident when compared to Fig. A.4, which can be attributed to the more consistent pressure boundary condition.

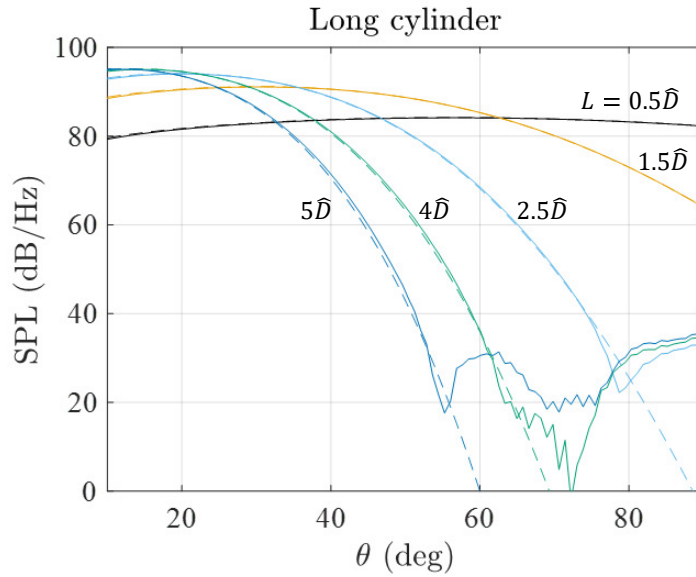


Figure A.5: Sound pressure levels from the long cylinder BEM computation (solid lines) and the analytic formula (dashed lines) for polar angles  $\theta$  and wavepacket length scales  $L$ . Field points are located at  $100\hat{D}$  from the origin.

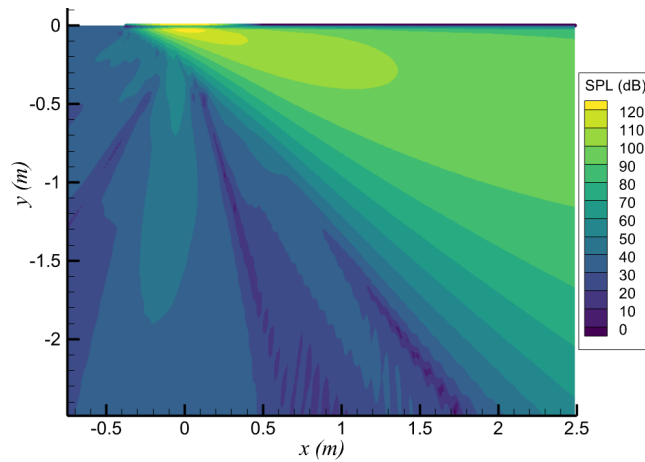


Figure A.6: Sound pressure levels generated from the long cylinder using a wavepacket of length scale  $L = 5\hat{D}$  along the vertical half-plane. The cylinder is visible near  $y = 0$ , spanning from  $x = -0.4$  m to  $x = 2.5$  m.

# Appendix B

## Flow Features Near the Edge of the Single-Stream Jet

The results presented in Section 4.4.3 discuss flow features near the edge of the three-stream jets, which included the study of vortical events peeling from the main flow and causing locally intense pressure drops. Nothing in that study suggested that the features presented were exclusive to multi-stream, or heated, jets. In fact, we can repeat the analysis with the single-stream jet and find good consistency in the results. This appendix presents the main figures of Section 4.4.3 applied to the single-stream jet of Section 3.

Figures B.1 and B.2 show contour plots of the skewness of the pressure and axial velocity fluctuations, respectively. The surface of peak Reynolds stress (SPS, red line) and radiator surface (white line) are included for completeness. The figures are very similar to those of the three-stream jets in Secs. 4.4.3, and therefore are applicable of the same commentary. There is a very notable layer of negative  $Sk_p$  near the edge of the jet, which is also very close to the center of a double layer of negative and positive  $Sk_u$ .

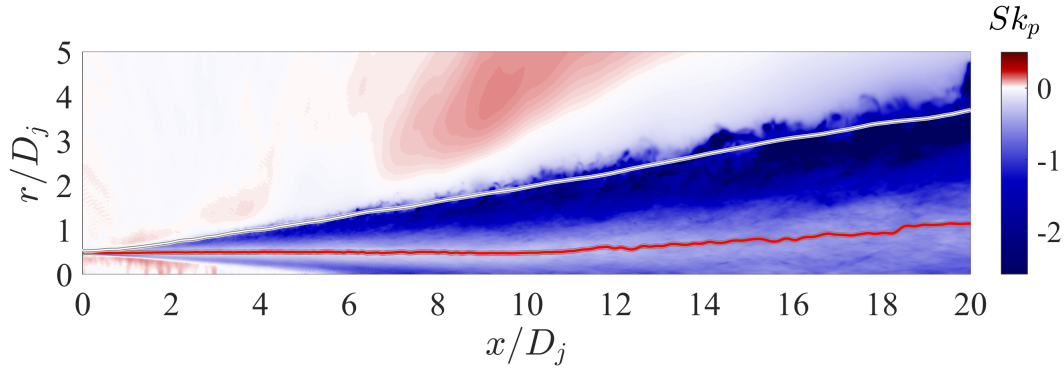


Figure B.1: Distribution of the skewness of the pressure fluctuation,  $Sk_p$ , of the single-stream jet. Red line: SPS. White line: radiator surface.

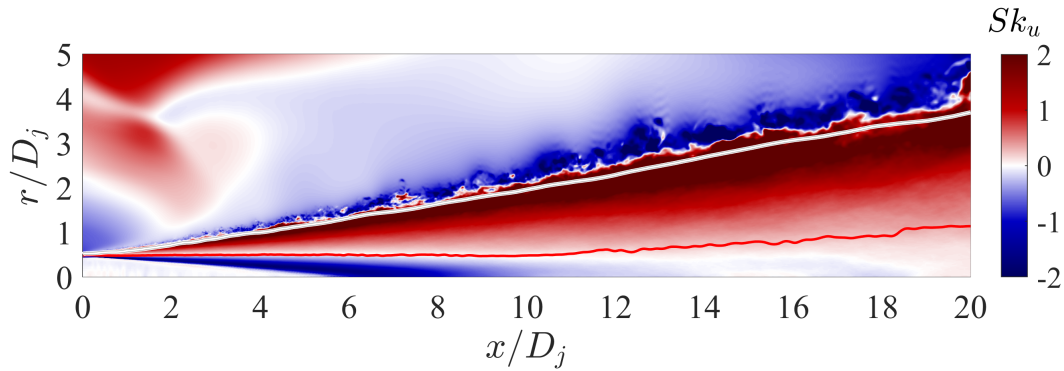


Figure B.2: Distribution of the skewness of the fluctuation of axial velocity,  $Sk_u$ , of the single-stream jet. Red line: SPS. Black double line: radiator surface.

For this jet, there is another layer of negative  $Sk_p$  between the shear layer and the potential core, which is visible in Fig. B.1 inwards of the SPS and for  $x/D_j \leq 8$ . This inner layer might be related to intermittent events when shear-layer vortical structures intrude into the of the potential core, as noted by Bogey *et al.* [16]. This phenomenon was, in fact, pointed in that work as a possible source for turbulent noise generation. The idea of shear layer turbulence intruding into the high-speed region of the potential core is also consistent with the negative values of  $Sk_u$  in that same area.

In Section 4.4.3 it is shown that the layers of pressure and velocity skewness near the jet edge are due to vortical events peeling off from the main flow and causing pressure drops. Correlations between vorticity and pressure reinforce that idea. Repeating that analysis to

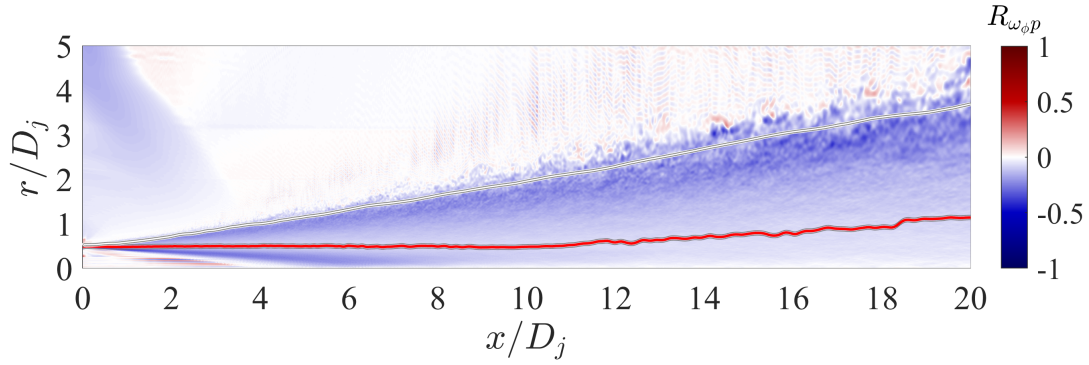


Figure B.3: Distribution of the normalized correlation between  $\omega'_\phi$  and  $p'$ ,  $R_{\omega_\phi p}$ . Red line: SPS. White line: radiator surface.

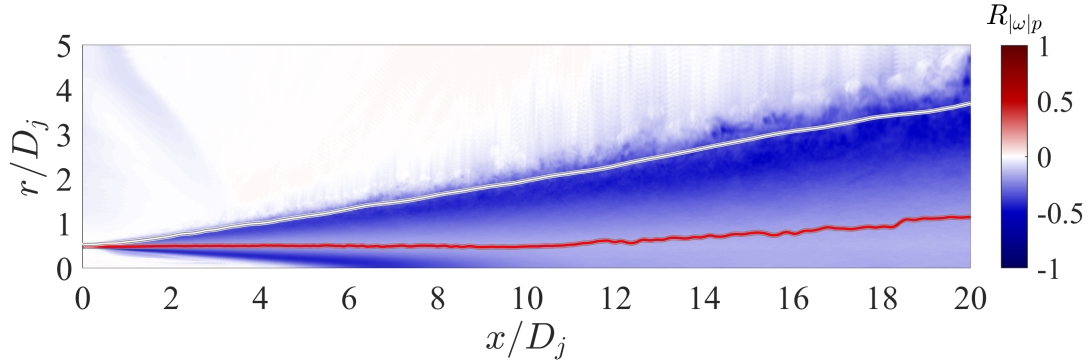


Figure B.4: Distribution of the normalized correlation between  $|\pm \omega|'$  and  $p'$ ,  $R_{|\pm \omega|p}$ . Red line: SPS. White line: radiator surface.

the three-stream jet yields consistent results, shown in Fig. B.3 and B.4. Figure B.3 shows a clear connection between azimuthal vorticity fluctuation ( $\omega'_\phi$ ) and pressure fluctuation ( $p'$ ) near the edge of the jet in the form of a negative correlation, which indicates that events of positive  $\omega'_\phi$  are linked to negative  $p'$  and vice versa. For completeness, Fig. B.4 plots the correlation of the module of vorticity ( $|\omega|$ ) and  $p'$ . This figure shows that unsigned vortical events are linked to pressure drops. Figs. B.3 and B.4 combined prove that the predominant connection between vorticity and pressure at the edge of the jet is through counter-clockwise vortical events and negative pressure fluctuations.